Université du Québec
Institut National de la Recherche Scientifique
Énergie Matériaux Télécommunications

ULTRAFAST REAL-TIME PHOTONIC SPECTROGRAMS

Par

Connor Mckenzie Layton Rowe

Mémoire présenté pour l'obtention du grade de
Maître ès Sciences, M.Sc.
en sciences de l'énergie et des matériaux

Jury d'évaluation

Examinateur externe	Joshua Schwartz Engineering Science Trinity University
Examinateur interne	Tarek Djerafi Institut National de la Recherche Scientifique (INRS-EMT)
Directeur de recherche	José Azaña Institut National de la Recherche Scientifique (INRS-EMT)

AVANT-PROPOS

Structure

A useful word for the reader on the language structure of this thesis. The abstract is given in both French and English on page ix and vii, respectively. A French summary of the entire thesis begins on page xix, while the English thesis 1 begins on page 1. Before the beginning of the English introduction, all titles are in French, with the exception of the main thesis title. A table of contents is included on page xii, followed by a list of figures, list of tables, and list of acronyms. The author has attempted to use the passive voice as much as possible throughout the text, except for certain cases where I find the active voice appropriate.

Un mot utile pour le lecteur sur la structure du langage de cette thèse. Le résumé est donné en français et en anglais à la page ix et vii. Un sommaire en français de l'ensemble de la thèse se trouve à la page xix, et la partie en anglais commence à la page 1. Avant le début de l'introduction en anglais, tous les titres sont en français, à l'exception du titre principal de la thèse. Une table des matières est inclue à la page xii, suivie d'une liste des figures, une liste des tables et une liste des acronyms.

Contributions

The project in its entirety was a collaborative effort Benjamin Crockett, José Azaña, and myself. José Azaña was the one to conceptualize the possibility of this project and introduce me to the time lens. José also gave insightful direction and supervision throughout the entirety of the development, and was closely involved in each stage of the project. I derived the early theoretical proof of the TLS, and began simulations with the guidance of Benjamin and José. Benjamin trained and mentored me in the laboratory, and supervised the first experimental demonstration for the TLS. Benjamin led the development of the TAIS using the TAI phase pattern, and together we experimentally verified the theoretical predictions. Benjamin also led the initial testing of the TLS for complex signals. Together we developed more tests for high bandwidth settings, wrapped spectrograms, coherent communications signals, and frequency hopping signals. Specifically for the results presented in the thesis, I have led the theoretical, simulation, and experimental results.

Histoire

In this section, I want to present a brief history of what I consider to be the "small" events that lined up in my life to lead me to where I am today, because I think it is a fun story. I do wonder if my career path could have turned out any differently had I slept in one day, or chosen a different cereal, or if all roads lead to this same outcome. I am not going to answer this question, but keep it in mind in the following paragraphs.

There was not an exact moment when I decided to go into the field of photonics. It was over the course of many years that I took small unconscious steps in this direction. I can reasonably attribute my early interest in science to the books I was gifted by my immediate and extended family for Christmases and birthdays (I preemptively say thank you for that). Among the lessons I learned from these early readings was to enjoy, and not be intimidated by, things I didn't understand (and still don't).

In high school, the seemingly innocent question "how does an electron move from place to place" probably cemented my interest in physics among the sciences, and also introduced me to the world of university libraries. The depth of knowledge of a university library seems practically infinite to a high school student, and I eventually found myself asking professors for help navigating the piles of books. This is how I met Patrick Irwin, the former University of Calgary physics lab supervisor. He invited me to join the demonstrations for undergraduate students, and even took the time to set up his favourite experiments for me. He also tried to teach me about the Fourier transform and windowing functions. Some of the highlights among the demonstrations were levitating superconductors, "rattlebacks" which are simple objects that only spin in one direction, and my personal favourite, a transmission hologram. By shining light on a small flat piece of transparent film, a three dimensional image formed on the other side of a chess board with all its pieces. This was not a clever trick, such as showing two slightly different images to each eye like in movie theaters. This flat film actually had all the information of a three dimensional object inscribed upon it. I could look around pieces to see what was behind, with incredible detail. The most shocking thing however, was when I looked through a small corner of the film which was broken off from the main part. I saw the exact same, full three dimensional chess board. Not only was the three dimensional information put onto the two dimensional surface of the film, but it was evenly distributed around the film so that it could be recreated using any small section (at the expense of spatial resolution). Although I didn't decide then and there to go into optics, it definitely made a lasting impact.

At the University of Waterloo, I met Heather Anderson through working for the Waterloo Physics Club. Heather is the lab supervisor for the Waterloo Physics department, and also has a fun collection of demonstrations, such as a Möbius strip superconducting track which unfortunately I never saw completely finished. Heather mentioned to me, on the down-low, that there was a seminar happening for one of my professors who had just won the Nobel prize in physics. She happened to know the time and room number where the presentation would be, although, technically it was supposed to be for graduate students and faculty. I decided to show up, and to my embarrassment, I was one of the first ones in the lecture hall. Grabbing a seat at the back, I tried to look as inconspicuous as possible. Donna Strickland, who was my professor for Electricity and Magnetism 2, was preparing her talk, and asked the few early members of the audience if she could get a couple of volunteers for a live demonstration of chirped pulses. As no one was volunteering, I decided to raise my hand. After the event, I received an email from Donna thanking me for raising my hand when no one else would, and saying she recognized me from class. As I was in the process of looking for a summer internship, I decided to read up on her papers and ask for a lab tour, prepared with the least dumb questions I could manage. After the second visit, I asked if I could do a research internship, which she accepted. It's possible that Heather Anderson is indirectly responsible for this thesis, or it's possible that I would've asked Donna for an internship even if I hadn't been at her talk. I'm not sure which is true but I am certainly glad for all the people like her who have helped me over the years.

The final set of circumstances which led to my joining the Ultrafast Optical Processing group with José Azaña, was during the Canadian Undergraduate Physics Conference in Montreal during the last year of my undergraduate studies. I was presenting on the work I was doing with Donna, and one of the attendees, Benjamin MacLellan, was my former residence Don during my first year of university. Ben recommended I visit the INRS booth at the conference, to learn about the possibilities for graduate studies. At the booth presenting about their work on invisibility in optical fibers, was Benjamin Crockett. Meeting Ben and José made up my mind as to where I wanted to be for my graduate studies. They were most enthusiastic scientists I had ever met, and great to get along with. They also produced impactful and interesting science and published at an incredible pace. I have been here ever since, under the direction of Ben and José, and will happily be for the next few years of my PhD.

Throughout my journey to photonics, I have definitely learned to keep an open mind for the opportunities that arise. I enjoy that so many seemingly small decisions made in such an impact in hindsight on what is my career so far. There are many people who I think about who have made their impacts on my life, and I would like to thank them in this next section.

Remerciements

I would first like to state a general thank-you to everyone on this list, and also to all the people who are not mentioned below.

I would like to thank my family for the support and encouragement. Thank you to my parents: Dad, Mom, Del, and Beatriz, for raising me, making me the person I am today, and never saying my goals are too far fetched. Thank you to my siblings: Kaleb, Halle, Shallon, and Gabriel, for inspiring me, making me laugh, and being great siblings. Thank you to my grandparents for the love and prayers: Grandma, Papa, Nanny, and Poppy Jeff. Thank you to David, Lesley, Tanko, and Max for welcoming me into their home and family. Thank you too all my aunts and uncles, especially to Uncle Don and Aunt Trudy who let me freeload for a summer. Thank you to my cousins, and extended cousins for all the parts you've played in my life.

I would like to sincerely thank all my friends who have caused me to spend the better half of my life with a smile on my face. I have learned more from friends than I ever have or will from books. Including my friends from hockey: Ziggy, Fig, Colin, Stephens, Cooper, Chase, I could go on.... From school: Zach, Aron, and Kaiden. And from university: Jade, Sarah, Maddie, and Tanko (again). As well as Basel, Celine, and Mujtaba, who made mathematics one of my life's passions. Thank you to my teachers in grade school who made mathematics and science so much fun: Sr. Plata, Sr. Lopez, Mr. Wiegele (I have not discovered a new particle to name a Wiegelion yet), Dr. Pike, and others. Thank you to all my coaches and mentors who taught me the importance of hard work and resilience: Randy, Bob, John, Bruce, Mr. Gill, Mr. Mo, and more.... Thank you to Lee Villeneuve and my friends at LVBJJ. Thank you to the Expos hockey franchise for the 10:30pm Monday night hockey games. I reiterate my thanks to Patrick Irwin, and Heather Anderson, who kept their doors open to students with a curious mind. Thank you to Ruxandra Moraru, Francis Poulin, David Mackinnon, and my other professors for their amazing teaching ability, approachability, and care for their students. I would like to give a special thank you to Donna Strickland, for allowing me to run amok in her lab, for giving me my first foundation in lasers and optics, and for writing me reference letters on what sometimes seems like a bimonthly basis.

Specifically relating to my research and this thesis, I would like to thank all the people who took the time to give me feedback on my thesis, including Uncle Don, Aunt Trudy, and Dr. Caroline Barnes. Thank you to Saket Kaushal for insightful discussions on coherent communications, to Manuel Fernández, to Rob Helstein, and to all my other colleagues at the INRS EMT. Thank you

to the committee members Joshua Schwartz and Tarek Djerafi for taking the time to review this thesis and offering many insightful comments.

Last but certainly not least, I would like to thank the two people who made this thesis possible, José Azaña and Benjamin Crockett. You two have been my mentors throughout my degree, and your constant teaching, support, and involvement make this work enjoyable and worth while. These past three years have been some of the best of my life, and there is nowhere in the world I would rather spend my graduate studies. Your research is world class, and you two are perfect examples of innovative, creative, enthusiastic, and intelligent scientists. I hope to publish many more papers and attend many more conferences with you during my PhD.

ABSTRACT

Microwave signals are a fundamental pillar of modern wireless communications, sensing and ranging, and imaging. Analysing these signals in time and frequency simultaneously, produces one of the most intuitive descriptions available in signal processing. Joint time-frequency representations, such as the spectrogram, have been widely used from sound and speech processing techniques, to enabling the full characterization of the fastest electromagnetic waves produced by man or nature. For many applications this type of analysis must be done in real-time, but without gaps in acquisition.

Digital signal processing is too slow to provide real-time and gapless analysis of microwave signals with more than a few GHz bandwidths and variations below the scale of hundreds of nanoseconds. Earlier photonic spectrogram processing techniques have provided either the necessary speed (temporal resolution) or bandwidth, but not both. In this thesis, two new photonics spectrograms are presented which were developed in the Ultrafast Optical Processing group at the INRS, which achieve unprecedented performance in speed and bandwidth. The first, the Time Lens Spectrogram, can achieve both high bandwidth into the hundreds of GHz range as well as high temporal resolution down to tens of picoseconds. The second, the Talbot Array Illuminator Spectrogram, provides high frequency resolutions in the MHz range and hundreds of analysis points along the frequency axis. These two spectrograms create a single complementary system which is versatile and reconfigurable to address a wider range of applications.

Presented here are results for these two spectrograms applied to microwave signals, achieving the real-time and gapless analysis of tens of GHz bandwidth signals with sub-nanosecond time resolutions or sub-GHz frequency resolutions, as desired. A theoretical connection is made between the two spectrograms, facilitating an in-depth analysis of their trade-offs and comparisons. The capability of these photonics spectrograms to analyse signals with significantly higher bandwidth than the detection or digitization devices employed is demonstrated, for what will be called super-bandwidth analysis. The application-oriented example of frequency hopping signals is utilized to emphasize that signals easily within the bounds of the proposed spectrograms are completely inaccessible to the state-of-the-art. Finally, this thesis demonstrates the Time Lens Spectrogram applied to a signal with phase information, to acknowledge the wide range of demonstrated and future work on optical signals.

Keywords Spectrogram, Time-Frequency Analysis, Microwave Photonics, Time Lens, Talbot Array Illuminator, Cognitive Communications

RÉSUMÉ

Les signaux micro-ondes sont un pilier fondamental des communications sans fil modernes, de la détection et de la télémétrie, et de l'imagerie. L'analyse de ces signaux en temps et en fréquence simultanément produit l'une des descriptions les plus intuitives disponibles pour le traitement des signaux. Les représentations conjointes temps-fréquence, telles que le spectrogramme, ont été largement utilisées dans les techniques de traitement du son et de la parole, jusqu'à permettre la caractérisation complète des ondes électromagnétiques les plus rapides produites par l'homme ou la nature. Pour de nombreuses applications, ce type d'analyse doit être effectué en temps réel, mais sans interruption de l'acquisition.

Le traitement électronique des signaux est trop lent pour permettre une analyse en temps réel et sans interruption des signaux micro-ondes avec des largeurs de bande de plus de quelques GHz et des variations inférieures à l'échelle de quelques nanosecondes. Les techniques antérieures de traitement des spectrogrammes photoniques ont fourni soit la vitesse nécessaire (résolution temporelle), soit la largeur de bande, mais pas les deux à la fois. Cette thèse présente deux nouveaux spectrogrammes photoniques développés par le groupe Ultrafast Optical Processing de l'INRS, qui atteignent des performances sans précédent en termes de vitesse et de largeur de bande. Le premier, le Time Lens Spectrogram, peut atteindre une bande passante élevée dans la gamme des centaines de GHz, ainsi qu'une haute résolution temporelle jusqu'à des dizaines de picosecondes. Le second, le Talbot Array Illuminator Spectrogram, offre des résolutions de haute fréquence dans la gamme des MHz et des centaines de points d'analyse sur l'axe des fréquences. Ces deux spectrogrammes créent un système complémentaire unique qui est versatile et reconfigurable pour répondre à une plus large gamme d'applications.

Les résultats de ces deux spectrogrammes appliqués à des signaux micro-ondes sont présentés ici. Ils permettent l'analyse en temps réel et sans lacune de signaux d'une largeur de bande de dizaines de GHz avec des résolutions temporelles inférieures à la nanoseconde ou des résolutions de fréquence inférieures au GHz, selon le souhait de l'utilisateur. Une connexion théorique est établie entre les deux spectrogrammes, facilitant une analyse détaillée de leurs compromis et de leurs comparaisons. La capacité de ces spectrogrammes photoniques à analyser des signaux ayant une largeur de bande considérablement plus élevée que les appareils de détection ou de digitalisation utilisés est démontrée, pour ce que l'on appellera l'analyse de la super largeur de bande. L'exemple orienté vers l'application des signaux de saut de fréquence est utilisé pour souligner que les signaux qui se situent facilement dans les limites des spectrogrammes proposés sont complètement inaccessibles à la technologie de pointe. Enfin, cette thèse démontre l'application du Time Lens Spectrogram à un signal avec information de phase, afin de reconnaître le large éventail de travaux démontrés et futurs sur les signaux optiques.

Mots-clés Spectrogramme, analyse temps-fréquence, photonique des micro-ondes, lentille temporelle, illuminateur de réseau Talbot, communications cognitives

TABLE DES MATIÈRES

LISTE DES FIGURES

LISTE DES TABLEAUX

LISTE DES ABRÉVIATIONS

Common Acronyms

arb.	Arbitrary Units
AWG	Arbitrary Waveform Generator
BER	Bit Error Ratio
CW	Continuous Wave
DSP	Digital Signal Processing
ECC	Error Correcting Code
FEC	Forward Error Correction
FWHM	Full Width at Half Maximum
FWM	Four-Wave Mixing
GVD	Group Velocity Dispersion
IM	Intensity Modulator
LCFBG	Linear-Chirped Fiber Bragg Grating
LiDAR	Light Detection And Ranging
norm.	Normalized Unit
OSA	Optical Spectrum Analyzer
PD	Photodetector
PM	Phase Modulator
QAM	Quadrature Amplitude Modulation
RF	Radio Frequency
RTO	Real-Time Oscilloscope
SMF	Single Mode Fiber
SNR	Signal to Noise Ratio
std. noise	Standard Deviation of Noise
SUT	Signal Under Test
TAI	Talbot Array Illuminator
TAIS	Talbot Array Illuminator Spectrogram
TL	Time Lens
TLS	Time Lens Spectrogram
XPM	Cross-Phase Modulation

Mathematical Parameters

β	Dispersive Propagation constant
β_2	Second-order dispersion coefficient (units ps^2/km)
$\ddot{\phi}$	Total dispersion (units ps^2)
Δt	Multilevel phase pattern step width
λ	Wavelength
$\mathcal{F}\{\cdot\}$	Fourier transform
$\mathcal{F}^{-1}\{\cdot\}$	Inverse Fourier transform
ω	Angular frequency (radians per second)
φ	Temporal phase
B_w	Bandwidth
f	Frequency (cycles per second)
I	Intensity
p	Primary phase factor
q	Amplification factor
T	Temporal period of lens function, lens aperture
t	time
V	Voltage

SOMMAIRE

Ce sommaire de la thèse comprend l'introduction, la méthodologie de l'expérience et certains des résultats.

0.1 Introduction

Sur les nombreuses façons dont l'information peut être encodée dans un signal, la plus familière est sans doute celle des changements de fréquence à travers le temps. La capacité de l'oreille humaine à distinguer l'intensité et la synchronisation des fréquences dans une onde acoustique est ce qui nous permet de traiter et de comprendre la conversation et la musique. Sans cette capacité à distinguer les fréquences, nous communiquerions probablement tous en code morse (bien que même le code morse contienne des informations sur les fréquences), et la musique serait sans doute moins intéressante. Réfléchir en termes de changements dans le domaine temporel est tellement intégré dans notre compréhension du monde qu'il est encore plus difficile d'imaginer que nous ne disposions pas d'informations temporelles sur les sons que nous entendons. Par conséquent, presque tout le monde a une expérience directe de la nécessité de résoudre un signal en temps et en fréquences à la fois. Cette intuition amène naturellement au concept de représentations conjointes temps-fréquence (JTFR), où le contenu en temps et en fréquence d'un signal est présenté dans une image à deux dimensions. Cependant, il est bien connu que les informations simultanées temps-fréquence des JTFR sont intrinsèquement ambiguës. En fonction de la durée de la portion de signal considérée, seules certaines fréquences pourront être résolues par l'observateur. Les signaux à bande étroite couvrent nécessairement une longue période de temps, ce qui nécessite une haute résolution de fréquence pour observer les changements qui se produisent pendant ces longues périodes de temps. Inversement, de nombreuses fréquences doivent interférer dans un signal à large bande pour donner lieu à des événements très courts, ce qui affecte la résolution temporelle. La versatilité est donc une caractéristique essentielle de tout type d'analyseur temps-fréquence afin de s'adapter aux différents types d'ondes à analyser.

La technique mathématique principale pour obtenir des informations simultanées temps et fréquence, ou JTFR, est la transformée de Fourier à temps court (STFT). Elle consiste à isoler un court segment temporel du signal testé (SUT) en le multipliant par une fonction de fenêtre. Ensuite, une transformée de Fourier est effectuée à partir de cette courte portion du signal pour obtenir son contenu en fréquence. Le processus est répété en décalant la fonction de fenêtre à travers le temps pour balayer l'ensemble de la forme d'onde. En raison du principe d'incertitude, le choix de la taille de la fonction de fenêtre est essentiel. Pour un certain signal, la fenêtre doit être suffisamment petite pour permettre l'identification temporelle d'événements courts, mais suffisamment grande pour distinguer les diverses fréquences des unes des autres. Ainsi, la STFT présente des artefacts évidents du principe d'incertitude en fonction de la durée et de la forme de la fonction de fenêtre. Les implémentations de cette méthode exigent que la fenêtre soit facilement reconfigurable pour détecter une large gamme de signaux différents.

Les innovations développées au cours des derniers siècles en ce qui concerne la manipulation des ondes électromagnétiques ont permis de mettre au point des outils exceptionnels pour l'analyse des spectrogrammes, jouant un rôle fondamental dans des domaines tels que le contrôle non destructif des matériaux (1), le traitement des signaux biomédicaux (2), la classification de la parole et de la musique (3; 4; 5), le radar (6), et les communications (7). Cependant, en raison de contraintes matérielles, il reste difficile d'extraire le JTFR d'ondes électromagnétiques avec des largeurs de bande supérieures à quelques GHz avec des caractéristiques temporelles inférieures à la seconde. Une exigence exceptionnellement difficile à satisfaire pour ces applications est que le traitement doit être effectué aussi rapidement que le signal arrive, c'est-à-dire en temps réel. Pour de nombreuses applications réalisées sur site, une latence de traitement de quelques microsecondes peut avoir des conséquences considérables. Prenons l'exemple de la classification en temps réel des véhicules aériens sans pilote (UAV) (8), des communications à sauts de fréquence ultrarapides avec l'objectif exprimé de subvertir les interférences malveillantes (9), ou même de la surveillance des implosions dans les installations de fusion par confinement inertiel à l'aide de la vélocimétrie Doppler (10). Il existe des méthodes qui éliminent des sections du signal afin de traiter une petite partie des informations en temps réel (11), ou des méthodes qui ralentissent les courtes sections échantillonnées du signal (12). Ces mise en œuvres ne sont pas acceptables en cas d'événements transitoires de courte durée ou si la forme d'onde varie continuellement de manière inconnue, comme dans les applications mentionnées ci-dessus. Par conséquent, les systèmes en temps réel impliquant des lacunes d'analyse sont d'un usage limité.

Les exigences relatives à l'obtention de la JTFR des formes d'ondes électromagnétiques en temps réel sont principalement satisfaites par des méthodes de traitement digital du signal (DSP). L'acquisition est effectuée via un converteur analogique-numérique sur le SUT, puis un algorithme de transformée de Fourier rapide met en œuvre numériquement la STFT. Les éléments électroniques et les algorithmes modernes peuvent facilement s'adapter à des signaux acoustiques avec des résolutions de fréquence <kHz, et peuvent être reconfigurés pour analyser des signaux de radiofréquence avec des largeurs de bande de quelques centaines de MHz et des résolutions temporelles inférieures à la microseconde (13). Cela correspond à des millions de transformées de Fourier par seconde (<10 MFT/s). Cependant, les applications mentionnées précédemment impliquent des dizaines ou des centaines de GHz de largeur de bande et des caractéristiques se produisant à l'échelle de la nanoseconde ou en dessous. Le traitement numérique du signal est donc limité à cet égard et n'a pas la versatilité nécessaire pour traiter les signaux micro-ondes à grande vitesse. C'est pour cette raison qu'une approche analogique beaucoup plus rapide du traitement en temps réel des signaux sans espace est souhaitée.

Un certain nombre de méthodes photoniques ont été développées pour résoudre un ou plusieurs des problèmes affectant le DSP. En général, ces techniques consistent à convertir le signal électrique dans le domaine optique par modulation électro-optique afin de tirer parti de la largeur de bande disponible dans les technologies photoniques, où des largeurs de bande de plusieurs dizaines de GHz sont considérées comme relativement étroites. Une méthode basée sur la diffusion Brillouin stimulée a dépassé le DSP et atteint une largeur de bande de 12 GHz, tout en conservant une résolution de fréquence impressionnante, mais les taux de transformation de Fourier et les résolutions temporelles restent comparables à ceux fournis par les technologies numériques (14). Une autre méthode photonique basée sur la modulation du SUT d'entrée sur des formes d'ondes chirpées traitées par propagation dispersive dans des boucles de fibre a amélioré la résolution temporelle par rapport au DSP, jusqu'à 30 ns, mais est limitée à des largeurs de bande maximales inférieures au GHz (15). Une méthode basée sur l'effet Talbot (16) permet d'améliorer à la fois la largeur de bande et la résolution temporelle avec le DSP. Toutefois, dans ce cas, la largeur de bande de détection requise doit être au moins dix fois supérieure à celle du SUT, ce qui limite la technique à moins de 5 GHz.

Récemment, deux nouvelles méthodes de spectrogrammes photoniques ont été développées, qui dépassent largement les capacités du DSP en termes de largeur de bande et de résolution temporelle, mais qui ont jusqu'à présent été traitées comme des stratégies différentes (17; 18). Ces deux techniques consistent en une modulation de phase temporelle d'un signal d'intérêt suivie d'une propagation dispersive pour reproduire le contenu spectral du signal directement dans le domaine temporel. La première approche est le spectrogramme à lentille temporelle (TLS), une extension du système d'imagerie à lentille temporelle bien étudié (19; 20), adapté à l'imagerie spectrale résolue dans le temps de formes d'ondes continuelles. Une investigation du TLS proposé a été publiée, avec pour objectif spécifique la récupération de la phase de formes d'ondes optiques rapides. Cette démonstration a permis d'obtenir des largeurs de bande d'analyse extrêmement élevées (448 GHz) et des résolutions temporelles ultra-courtes (62,5 picosecondes), avec plus de 16 milliards de transformées de Fourier par seconde (17). Le second, le Talbot Array Illuminator Spectrogram (TAIS), ajoute polyvalence et simplicité aux spectrogrammes optiques à cartographie temporelle basés sur l'effet Talbot en supprimant les exigences strictes en matière de technologie (21; 22).

Dans cette thèse, un cadre pour un analyseur temps-fréquence spécifiquement destiné aux signaux micro-ondes est proposé en utilisant des composants optiques linéaires, ce qui offre à l'utilisateur un haut degré de versatilité pour personnaliser les spécifications de performance en fonction des exigences de l'application. La figure 1 donne un aperçu conceptuel du cadre proposé. Un cadre mathématique général reliant le TLS et le TAIS est présenté et les caractéristiques et les compromis de chaque spectrogramme sont examinés dans le cadre d'une étude approfondie sur les signaux micro-ondes de diagnostic et d'application. Les principaux résultats montrent que le TLS peut atteindre de très grandes largeurs de bande et des résolutions temporelles très étroites. Cependant, compte tenu des contraintes des composants électro-optiques pratiques utilisés pour la modulation de phase temporelle, le TLS ne peut jusqu'à présent atteindre qu'un nombre limité de points d'analyse et de résolution de fréquence. Le TAIS surmonte cette limitation en utilisant une modulation de phase temporelle intelligente à plusieurs niveaux pour obtenir facilement 40 fois plus de points d'analyse, ce qui se traduit par une meilleure résolution de fréquence. Cependant, le TAIS est limité dans sa largeur de bande maximale et sa résolution temporelle par d'autres composants impliqués. Le chapitre 3.3 et le tableau 3.1 présentent une analyse complète des compromis. Ainsi, le TLS et le TAIS présentent ensemble une gamme de conditions de conception possibles pour traiter les signaux continus à large bande ultrarapides les plus extrêmes, réalisés par le même équipement.

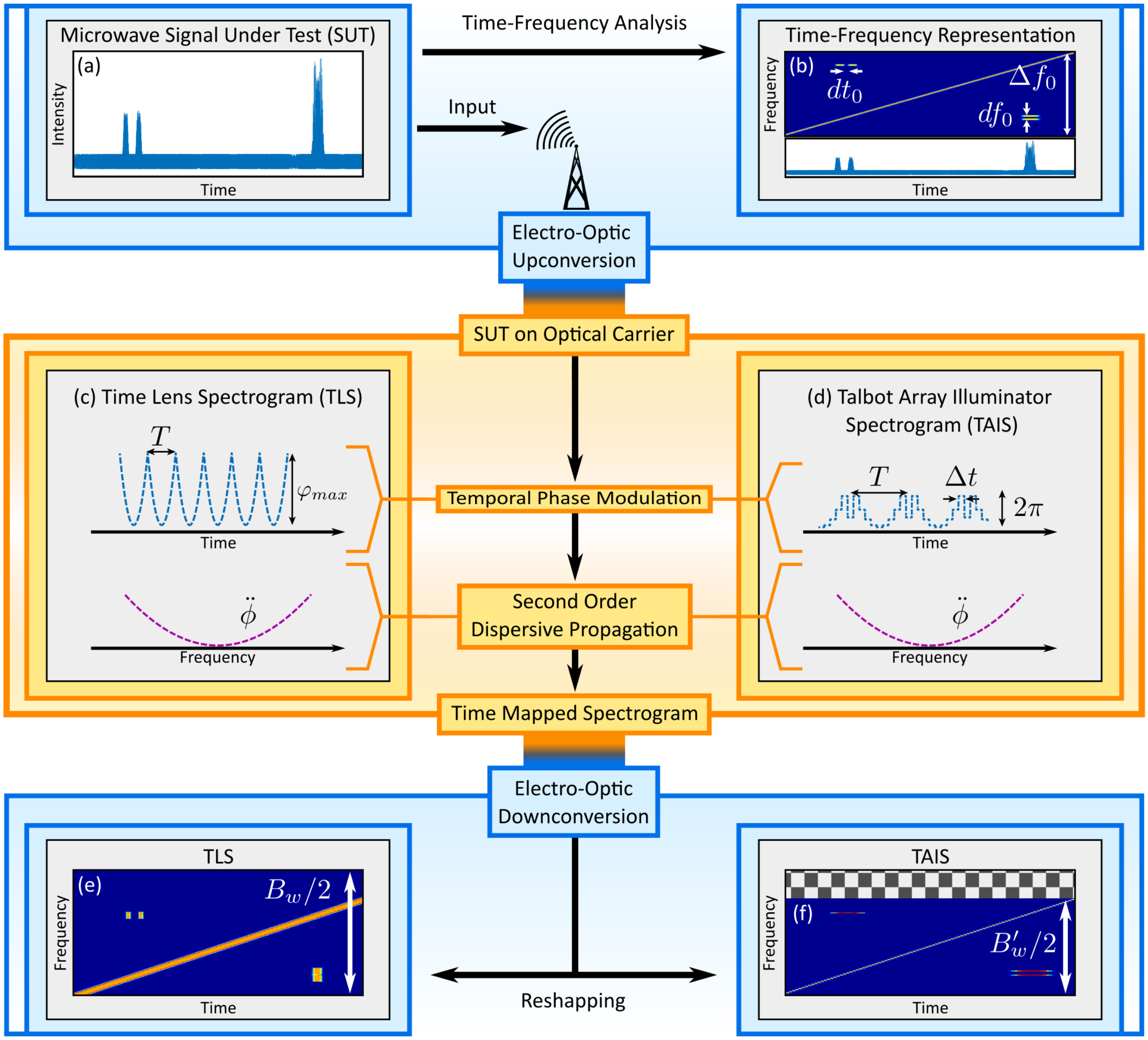

Figure 1 : Aperçu conceptuel des deux spectrogrammes photoniques. (a) SUT micro-onde représenté en intensité dans le temps. (b) Caractéristiques du SUT dans une représentation temps-fréquence consistant en un chirp linéaire, deux événements étroitement espacés dans le temps de dt_0, deux événements étroitement espacés en fréquence df_0, sur une largeur de bande micro-onde de Δf_0. Le signal est ensuite converti dans le domaine optique par modulation d'intensité sur une chauffeur optique. (c) Le TLS consiste en une modulation de phase temporelle selon des fonctions quadratiques consécutives, suivie d'une propagation dispersive de second ordre pour compléter les transformées de Fourier réalisées dans le temps. (d) Le TAIS est identique, à l'exception du fait que la modulation de phase temporelle est constituée par une configuration de phase discrète à plusieurs niveaux, enroulée à 2π avec une période de niveau constante Δt. La conversion électro-optique vers le bas par un photodétecteur reconvertit le signal dans le domaine électrique. La sortie de la transformée de Fourier consécutive réalisée dans le domaine temporel à partir des spectrogrammes est remodelée pour que chaque transformée de Fourier soit placée verticalement. Cela produit l'image du spectrogramme en deux dimensions (fréquence vs temps) montrée en (e) pour le TLS, fournissant une plus grande largeur de bande d'analyse B_w, et une plus grande résolution temporelle au prix de points d'analyse (moins bonne résolution en fréquence). Le signal micro-ondes est modulé sur la porteuse optique de manière à obtenir des spectres symétriques double face sur une largeur de bande complète B_w, soit deux fois la fréquence DC à la fréquence maximale. (f) Tracé en deux dimensions pour le TAIS, avec une largeur de bande d'analyse plus faible $B_w^{'}$ et une moins bonne résolution temporelle, mais avec une meilleure résolution en fréquence et un plus grand nombre de points d'analyse.

0.2 Méthodes

La démonstration expérimentale se compose d'une étape de génération de SUT à la figure 2(a), d'une étape de traitement de spectrogrammes optiques à la figure 2(b), et d'une étape de détection et de récupération à la figure 2(c).

Le SUT micro-onde est généré à l'aide d'un générateur de formes d'ondes arbitraires (AWG) avec un freqence d'échantillonnage de 92 GSa/s et amplifié par un amplificateur de radiofréquence (RFA). Une sortie de l'AWG est envoyée à un oscilloscope en temps réel (RTO) de 28 GHz pour lancer l'échantillonnage du RTO au même endroit du signal à chaque fois. Cela permet de visualiser le signal à l'aide du RTO avant la collecte des données. Dès que les données sont collectées, une copie du signal souhaité est récupérée et le déclenchement devient inutile. Pour analyser les signaux micro-ondes en espace libre, il serait possible de commencer la capture par une antenne de réception et de procéder ensuite de la même manière que pour le reste de la démonstration présentée ici.

L'étape du spectrogramme optique consiste en un laser à ondes continues (CW) réglé sur 1550 nm avec une largeur de ligne inférieure à 0.1 kHz, connecté à un IM électro-optique de 40 GHz qui reçoit le SUT électrique pour une conversion ascendante dans le domaine optique. Les fonctions de modulation de phase temporelle TLS et TAIS sont générées par le même AWG de 92 GSa/s qui a généré le SUT, ce qui permet d'utiliser le meilleur équipement possible disponible et non de répondre à une quelconque exigence de synchronisme. Les signaux électriques de modulation de phase temporelle sont amplifiés par un RFA avant d'alimenter un modulateur de phase (PM) électro-optique. Pour le TLS, un RFA d'une puissance saturée de 33 dB avec une largeur de bande de 32 GHz est utilisé, tandis que pour le TAIS, un RFA d'une largeur de bande de 50 GHz avec 23 dB de puissance saturée est utilisé. Pour maximiser l'excursion de phase possible dans le cas du TLS, un modulateur de phase de 30 GHz avec un $V_\pi = 2.6$ V est utilisé, et un modulateur de phase de 40 GHz avec $V_\pi = 3.1$ V pour le TAIS. Les modulateurs sont polarisés aux voltages demi-onde, pour diminuer la contribution du courant continu. Le SUT optique traverse le PM et passe par un réseau de Bragg à fibres linéairement chirpé (CFBG) introduisant une dispersion du second ordre de $\ddot{\phi} \approx 2{,}508$ ps^2 pour le TLS et $\ddot{\phi} \approx 15{,}415$ ps^2 pour le TAIS. Le réseau à moindre dispersion fonctionne sur l'ensemble de la bande optique C (largeur de bande >5 THz), tandis que le réseau à plus grande dispersion a une largeur de bande plus petite d'environ 650 GHz.

Pour une récupération presque optimale des spectrogrammes, une photodiode (PD) de 50 GHz est utilisée pour transférer le signal traité du domaine optique au domaine électrique, et un oscilloscope en temps réel (RTO) de 28 GHz pour passer du domaine électrique au domaine digital. Pour analyser les effets d'une largeur de bande de détection limitée sur le spectrogramme obtenu, deux situations sont testées avec une largeur de bande intentionnellement réduite. La première consiste à limiter la largeur de bande de détection du RTO dans la programmation du dispositif. La seconde consiste à utiliser une largeur de bande de 6 GHz pour la conversion optique-électronique. Pour évaluer la performance du TLS et du TAIS à récupérer les spectres globaux appropriés des SUT, les données du spectrogramme sont projetées sur l'axe des fréquences et normalisées, puis comparées à la trace d'un analyseur de spectre optique (OSA). L'OSA est utilisé à la place d'un analyseur de spectre RF ou de la transformée de Fourier rapide (FFT) du SUT électrique afin d'isoler les réponses spectrales du TLS et du TAIS des aberrations attendues résultant de la conversion ascendante électro-optique non idéale. Toutefois, la calibration de la fréquence discutée dans les résultats est également confirmée par la FFT du SUT électrique, et l'affaiblissement de l'étage de conversion électro-optique peut être observé en comparant les différents spectres de la figure 5.1.

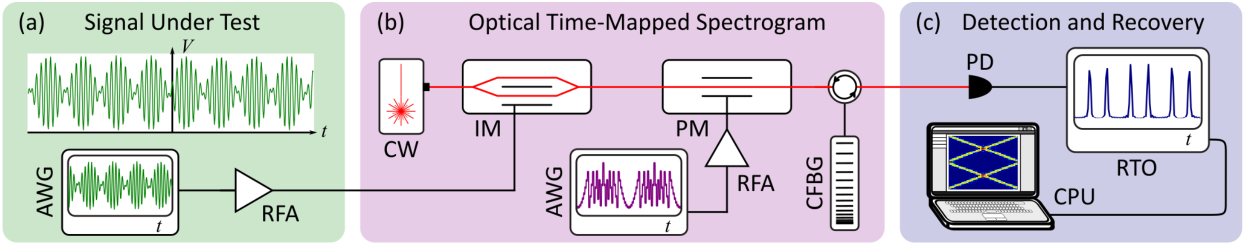

FIGURE 2 : Configuration expérimentale pour le test des deux spectrogrammes photoniques, le TLS et le TAIS. L'étape du SUT génère le signal micro-ondes électrique. L'étape du spectrogramme optique temporel convertit le signal micro-ondes dans le domaine optique, puis la modulation de phase du TLS ou du TAIS ainsi que la dispersion chromatique donnent lieu à des transformées de Fourier temporelles consécutives. L'étape de détection et de récupération consiste en une photodiode d'intensité de loi carrée, pour la conversion de la forme d'onde optique dans le domaine électrique, et la conversion analogique-numérique par un oscilloscope en temps réel. L'ordinateur transforme le spectrogramme temporel en une image en deux dimensions qui peut être visualisée.

0.3 Résultats

Les premiers résultats comparent l'une des méthodes photoniques proposées au DSP hors ligne standard pour un SUT dont la fréquence augmente lentement. La première méthode est le TAIS à largeur de bande totale de 46 GHz et la numérisation ultérieure par le DP rapide de 50 GHz et le RTO de 28 GHz. La seconde est le système traditionnel comportant une conversion analogique-numérique (ADC) du SUT électrique de l'AWG par le PD et le RTO, puis le calcul digital de la STFT (nécessairement hors ligne, pas en temps réel, pour se rapprocher de la performance du TAIS). Le SUT consiste en un chirp unique dont la fréquence varie de 0.5 GHz à 21 GHz, sur une durée de 5.35 μs. Les deux méthodes sont comparées alors que la largeur de bande de détection est méthodiquement abaissée en dessous de celle du SUT, de 28 GHz à 6 GHz. La tentative de récupération d'un SUT avec une largeur de bande beaucoup plus grande que celle de l'ADC (RTO) mettra en évidence la capacité unique du TLS et du TAIS à récupérer le spectrogramme de ces signaux de manière satisfaisante.

Le spectrogramme optique temporel du TAIS est présenté au-dessus de la STFT hors ligne du signal électrique à la figure 3. Comme la largeur de bande de l'oscilloscope est réduite, on s'attend à ce que le critère d'échantillonnage de Nyquist ne soit pas satisfait pour les fréquences plus élevées de l'objet testé, et donc à ce que les spectrogrammes STFT échouent à ces fréquences. La première rangée de spectrogrammes, affichant le TAIS, démontre de manière concluante que l'abaissement de la largeur de bande de détection n'affecte que la résolution en fréquence, et non la largeur de bande, comme indiqué dans la section précédente. Cette détérioration de la résolution en fréquence se traduit par un élargissement du chirp unique dans la direction de la fréquence. Dans la deuxième ligne, la STFT hors ligne présente une coupure nette de la largeur de bande à la fréquence attendue. À droite des spectrogrammes se trouve le spectre du SUT après modulation optique, pris avec un OSA, comparé à la projection de fréquence du TAIS à la limite RTO de 6 GHz. La STFT hors ligne dans le cas de la limite RTO de 6 GHz est comparée à la FFT hors ligne de l'ensemble du SUT électronique. L'OSA présente un affaiblissement de la fréquence vers les largeurs de bande plus élevées, comme prévu par l'effet de la conversion ascendante électro-optique non idéale, tandis que la projection de la fréquence du TAIS avec une largeur de bande de numérisation de 6 GHz entraîne un affaiblissement de la fréquence légèrement plus important.

Il est important de noter que le TAIS récupère toujours la totalité de la bande passante du signal avec un léger affaiblissement qui pourrait être compensé par la caractérisation des réponses en fréquence des étapes de conversion dans le cadre d'une étude future. La détection électronique classique, par contre, produit une coupure immédiate et un spectre irrécupérable à partir d'une

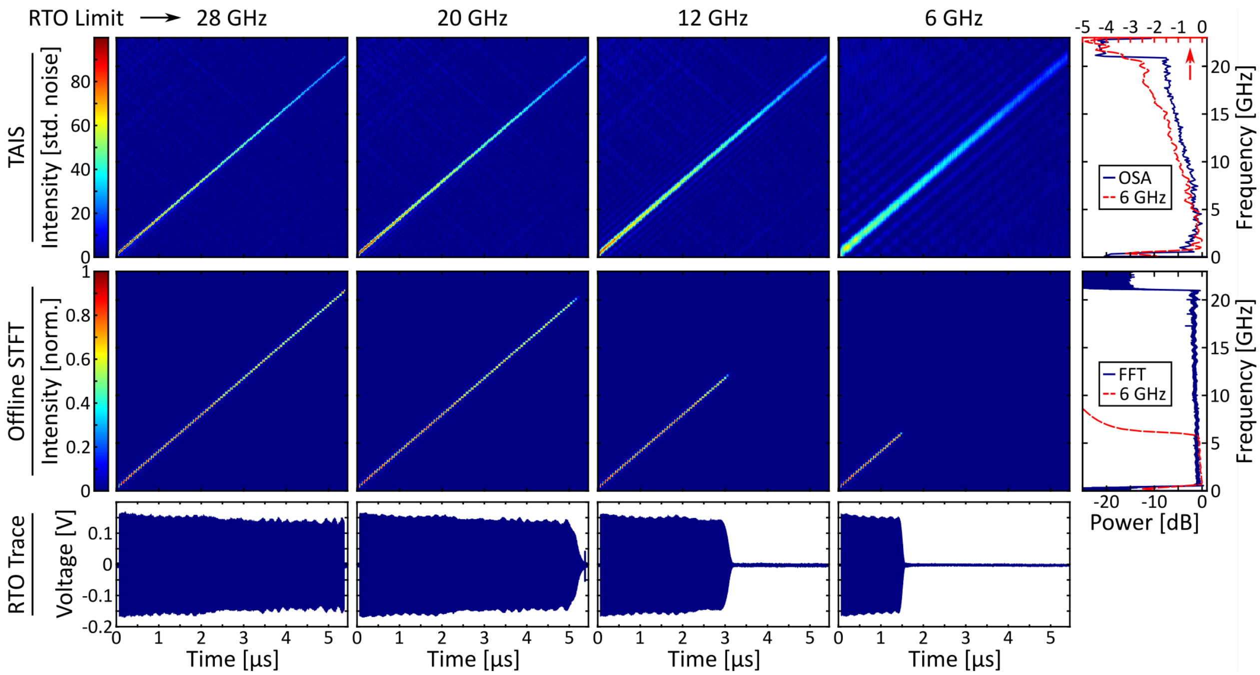

FIGURE 3 : TAIS comparé au STFT hors ligne (pas en temps réel) du SUT électronique. Le STFT est choisi pour avoir la même fenêtre temporelle que le TAIS et, en raison des limitations de la vitesse de traitement, cette approche DSP est nécessairement effectuée hors ligne après que le SUT a été numérisé et sauvegardé par le RTO. La coupure de la largeur de bande attendue en raison de l'échantillonnage sub-Nyquist de la STFT électronique est confirmée mais n'est pas présente dans le TAIS, qui montre une récupération de la largeur de bande complète même avec une largeur de bande RTO limitée. Le spectre à droite du TAIS compare la trace OSA à la projection du TAIS sur l'axe des fréquences pour le cas limité à 6 GHz, montrant une décroissance plus rapide mais identifiant toujours correctement les fréquences présentes. Le spectre à droite du STFT hors ligne compare la transformée de Fourier rapide (FFT) du signal électrique devant être généré par l'AWG (avant l'AWG), avec la FFT du signal électrique provenant directement de l'AWG numérisé par le RTO lorsqu'il est limité à une largeur de bande de 6 GHz. Entre ces trois spectres, on peut voir la détérioration due à l'étape de conversion ascendante électro-optique (FFT électrique vers OSA) et la détérioration due à la récupération du TAIS à 6 GHz (OSA vers projection de fréquence à 6 GHz). Sous les spectrogrammes, la coupure de fréquence peut être observée dans la trace temporelle du signal électrique lorsque la fréquence devient trop élevée pour être correctement échantillonnée avec la largeur de bande correspondante.

certaine fréquence, sans possibilité de compensation. Comme le TAIS fournit un grand nombre de points d'analyse par spectre, on peut se permettre d'utiliser des appareils de détection à bande passante plus étroite, car la détérioration de la résolution en fréquence permettra toujours d'obtenir un spectrogramme d'une résolution acceptable (environ 27 points d'analyse par spectre, après détérioration en utilisant une limite de bande passante de 6 GHz). Il en va de même pour le TLS. Cependant, en raison des limitations matérielles sur la force de la lentille temporelle de la modulation de phase électro-optique, seul un nombre inférieur de points d'analyse est disponible dès le départ. Par conséquent, il n'est pas possible de sacrifier une grande partie de la résolution de fréquence pour réduire la largeur de bande de détection nécessaire.

Les deuxième résultats démontrent la résolution extrêmement élevée en fréquence fournie par le TAIS. L'application suivante vise à fournir une démonstration concrète des possibilités de performances supérieures offertes par les deux spectrogrammes photoniques par rapport au DSP, ainsi qu'à d'autres méthodes photoniques spécialisées. En particulier, un signal de saut de fréquence ultra-rapide et à large bande avec plusieurs canaux est analysé par un seul système TAIS. L'SUT est composé de 20 niveaux de fréquence régulièrement espacés de 1 GHz à 21 GHz, s'allumant et s'éteignant de manière aléatoire, ce qui entraîne des événements de diverses durées allant jusqu'à l'échelle de la nanoseconde, qui ne peuvent pas être identifiés à l'aide des technologies DSP de pointe. En fait, même les méthodes photoniques récemment signalées pour la récupération de signaux de saut de fréquence (9; 23) sont soit très rapides en termes de méthodes de mesure instantanée de fréquence, soit plus lents mais pouvant accueillir plusieurs canaux simultanés.

Dans les résultats présentés, la plus longue durée d'événement consiste en deux sauts successifs, mais en principe, il n'y a pas de limite car les spectrogrammes sont tous deux en temps réel. La durée de saut la plus courte est réglée pour être égale à dix fois la résolution temporelle de TLS, soit $10 \cdot 696ps = 6.96ns$, ce qui est supérieur à la résolution du TAIS $T = 4.48ns$ d'un facteur de 1.56. Le nombre de points d'analyse disponibles du TAIS est 206 par spectre double face. Par conséquent, ce TAIS pourrait accueillir plus de 100 canaux de fréquence simultanés et arbitraires avec une période de saut inférieure à 5 ns. Le nombre potentiel de canaux devient encore plus important dans le cas du TAIS à large bande passante avec une détérioration de la détection de 716 points d'analyse. Les sauts du SUT n'étaient pas synchronisés avec le système TAIS, et par conséquent, les sauts arrivent à une position inconnue dans les fenêtres d'analyse.

Le TAIS est présenté dans la figure 4. Les spectres du SUT mesurés par l'OSA sont présentés dans la figure 4(a), ainsi que la projection de fréquence du TAIS résultant. La figure 4(b) affiche le TAIS pour une partie du signal de saut de fréquence. Remarquez la clarté impressionnante des sauts individuels, et gardez en tête qu'aucune autre méthode ne serait en mesure de récupérer ce signal en temps réel. La comparaison avec la STFT hors ligne dans la figure 4(c) montre que le TAIS récupère correctement la fréquence et le moment des événements avec une résolution suffisante. La partie du TAIS affichée dans ces deux figures contient plus de 80 événements, avec plusieurs fréquences présentes simultanément. Dans la figure 4(d), le nombre maximum de sauts présents à la fois est de 3, cependant, le nombre maximum prévu de canaux de fréquence serait de l'ordre d'un par point d'analyse sur un spectre à simple face, dans le cas des résultats présentés, environ 103. Dans la figure 4(d), (e), une autre partie du signal de saut de fréquence est montrée avec des événements très rapprochés et des fréquences multiples se produisant simultanément.

La résolution en fréquence supérieure est certainement un avantage que le TAIS offre pour les signaux de saut de fréquence, mais le TLS est avantageux pour augmenter la fréquence de saut en raison de sa remarquable résolution temporelle. Dans la partie principale de la thèse, il sera démontré que le TLS peut surpasser le TAIS pour la récupération de signaux de saut de fréquence si la vitesse de saut est trop rapide pour le TAIS, mais il est important de noter que le TLS souffre toujours d'une faible résolution en fréquence. En équilibrant le nombre de canaux de fréquence avec la période de saut, il serait possible de maximiser la capacité d'information potentielle pour le TLS et le TAIS en fonction des compromis de la section 3.3.

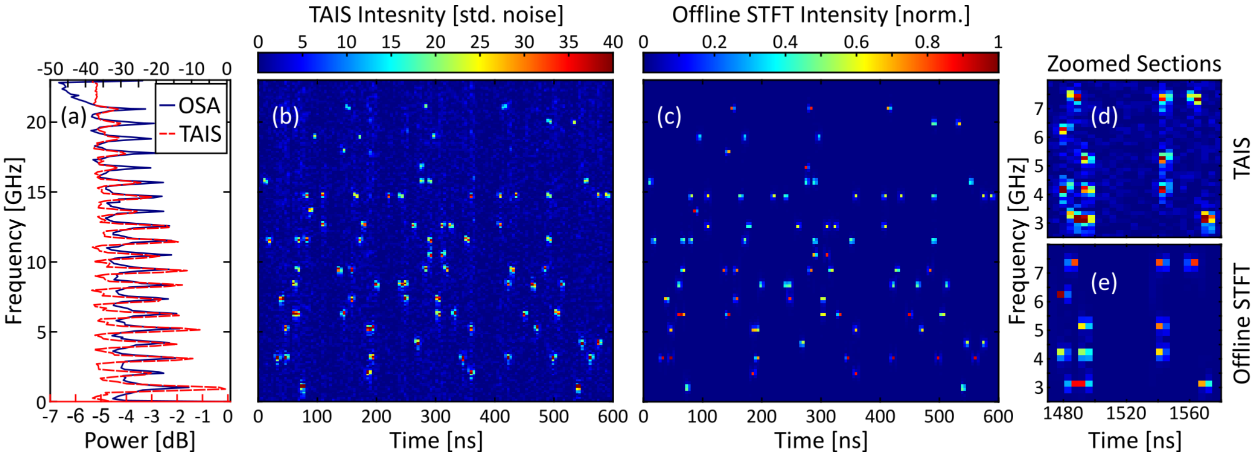

FIGURE 4 : Le signal à saut de fréquence analysé par le TAIS, comparé avec la STFT hors ligne (analyse non temps réel) de l'appareil électronique SUT. Le signal est composé de plus de 80 événements temps-fréquence se produisant sur une durée d'environ 600 ns et avec 20 niveaux de fréquence régulièrement espacés de 1 à 21 GHz. Plusieurs événements de fréquence peuvent se produire simultanément ou très rapprochés dans le temps. (a) La projection du TAIS sur le domaine de fréquence est superposée sur le spectre provenant de l'OSA mesurant les micro-ondes sur l'appareil SUT optique. (b) Le spectrogramme en temps réel obtenu par le TAIS. (c) La STFT hors ligne du signal électrique provenant de l'AWG, en utilisant une fenêtre d'analyse de la même taille que le TAIS. (d), (c) Deux petites sections zoomées d'une autre partie du signal à saut de fréquence sont montrées pour le TAIS et la STFT hors ligne respectivement.

0.4 Conclusions

Cela conclut un bref résumé des principaux résultats présentés dans cette thèse. Un lien théorique entre le spectrogramme du lentille temporel et le spectrogramme de l'illuminateur Talbot array a été démontré. Leurs capacités pour l'analyse de signaux micro-ondes, à large bande passante, sans interruption et en temps réel ont été présentées, ainsi qu'une analyse technique et expérimentale approfondie de leurs paramètres de conception et de leurs compromis. En utilisant des appareils électro-optiques disponibles commercialement, un signal de 46 GHz de largeur de bande a été récupéré en utilisant uniquement une photodiode de 6 GHz. D'un intérêt particulier et immédiat sont les applications découlant de la récupération d'un signal de saut de fréquence ultra-rapide avec des sauts à l'échelle de la nanoseconde et de multiples canaux simultanés sur 20 GHz de largeur de bande réelle. Ces spectrogrammes présentent jusqu'à présent les performances les plus impressionnantes pour les communications cognitives dans la littérature.

Une brève démonstration de la capacité à récupérer des signaux optiques avec des informations de phase est également présentée dans la partie principale du thèse. La possibilité de récupérer des communications cohérentes à l'aide de ces spectrogrammes d'une manière qui repose uniquement sur une détection basée sur l'intensité, et non interférométrique, est propre à ce système. La simplicité par rapport aux techniques de détection cohérente impliquant des oscillateurs locaux stables ou un traitement numérique intensif rend le TLS et le TAIS compétitifs pour les télécommunications optiques dans certaines applications. De plus amples détails sur les possibilités en spectroscopie, caractérisation ultra-rapide et LIDAR se trouvent dans les publications créditées.

1 INTRODUCTION

1.1 Overview

Of the many ways information can be encoded in a signal, the most familiar may be through changes in frequency over time. The ability of the human ear to pick out the intensity and timing of frequencies in a sound wave is what allows us to process and understand speech and music. Without the ability to tell frequencies apart, we would likely all be communicating in some sort of morse code (although even morse code has some frequency information), and music would no doubt be less interesting. Thinking in terms of changes over time is so ingrained in our understanding of the world, it is even harder to imagine if we did not have temporal information about the sound we hear. Therefore almost everyone has first-hand experience as to why resolving a signal in both time and frequency is necessary. This intuition leads naturally to the concept of joint time-frequency representations (JTFR), where the time and frequency content of a signal are laid out in a two-dimensional image. Yet it is well known that simultaneous time-frequency information of JTFRs is intrinsically ambiguous. Depending on the duration of the portion of a signal considered, only certain frequencies will be resolvable to the observer. Narrow band signals necessarily extend over a long time duration, requiring high frequency resolution to observe changes occurring over such long time periods. Conversely, many frequencies must interfere in a broadband signal to give rise to very short events, affecting time resolution. Thus, versatility is a key enabling feature of any kind of time-frequency analyser to adapt to the various types of waves to be analysed.

The main mathematical technique to obtain simultaneous time-frequency information, or JTFRs, is the short-time Fourier transform (STFT). It consists of isolating a short time segment of the signal under test (SUT) by multiplying it with a windowing function. Then, a Fourier transform is taken from this short portion of the signal to obtain its frequency content. The process is repeated by shifting the windowing function in time to scan through the entire waveform. Due to the uncertainty principle, the choice of the windowing function's size is critical. For a given signal, the window needs to be small enough to temporally identify short events, but large enough to resolve frequencies from one another. As such, the STFT exhibits clear artifacts from the uncertainty principle depending on the duration and shape of the windowing function. Implementations of this approach require the window to be easily reconfigurable to detect a wide range of different signals.

The innovations for manipulating electromagnetic waves developed in the past few centuries have enabled the development of exceptional tools for spectrogram analysis, demonstrating fundamental roles in fields such as nondestructive material testing (1), biomedical signal processing (2), speech and music classification (3; 4; 5), radar (6), and communications (7). However, due to hardware constraints, it remains challenging to retrieve the JTFR of electro-magnetic waves with bandwidths above a few GHz with sub-ns temporal features. An exceptionally challenging requirement for such applications is that the processing must be done as quickly as the signal is arriving, i.e., in real-time. For many in situ applications, processing latency of a few microseconds can result in tremendous consequences. Consider for example real-time Unmanned Aerial Vehicle (UAV) classification (8), ultrafast frequency hopping communications with the expressed purpose of subverting nefarious interference (9), or even monitoring implosions within inertial confinement fusion facilities using Doppler velocimetry (10). There exist methods which discard sections of the signal in order to process a small portion of the information in real-time (11), and other methods to slow down short sampled sections of the signal (12). These are not an acceptable implementations if short transient events are involved or if the waveform is continuously varying in an unknown fashion, such as those involved in the aforementioned applications. Hence, real-time schemes involving analysis gaps are limited in their usage.

The demands for obtaining the JTFR of electro-magnetic waveforms in real-time are primarily met through digital signal processing (DSP) methods. Acquisition is performed via an analog-to-digital converter on the SUT and then a fast Fourier transform algorithm digitally implements the STFT. Electronic components and modern algorithms can easily adapt to slow acoustic signals with <kHz frequency resolutions, and can be reconfigured to analyse radio frequency signals with bandwidths of a few hundred MHz with sub-microsecond time resolutions (13). This corresponds to millions of Fourier transforms per second (<10 MFT/s). However, the applications mentioned previously involve tens or hundreds of GHz of bandwidths and features occurring on the nanosecond scale or below. DSP is thus limited in this regard and does not have the needed versatility to treat high-speed microwave signals. It is for this reason that a much faster analog approach to real-time gapless processing is desired.

There have been a number of photonic methods aimed at resolving one or more of the issues affecting DSP. In general, these techniques rely on upconverting the electrical signal to the optical domain by electro-optic modulation to leverage the bandwidth available from photonics technologies, where bandwidths of tens of GHz are considered relatively narrowband. A method based on stimulated Brillouin scattering has surpassed DSP and achieved up to 12 GHz bandwidth, while maintaining impressive frequency resolution, but the Fourier transform rates and time resolutions remain on par with those provided by digital technologies (14). Another photonics method based on modulation of the input SUT on chirped waveforms processed by dispersive propagation in fiber loops has improved the time resolution in comparison to DSP, down to 30 ns, but is limited to sub-GHz maximum bandwidths (15). An approach which improves upon both the bandwidth and the time resolution capable with DSP is a method based on the Talbot effect (16). Still, in this case the required detection bandwidth needed must be at least ten times higher than that of the SUT, limiting the technique to below 5 GHz.

Recently, two new photonics spectrogram methods have been developed which have both shown to far exceed the capabilities of DSP in both bandwidth and time resolution but have been so far treated as different strategies (17; 18). These two techniques consist of a temporal phase modulation of a signal of interest followed by dispersive propagation to map the spectral content of the signal directly onto the time domain. The first approach is the Time Lens Spectrogram (TLS), an extension of the well-studied Time Lens imaging system (19; 20), adapted for time-resolved spectral imaging of continuously varying waveforms. An investigation of the proposed TLS has been published, with the specific focus of recovering the phase of fast optical waveforms. This demonstration accomplished extremely high analysis bandwidths (448 GHz) and ultrashort time resolutions (62.5 picoseconds), achieving over 16 billion Fourier transforms per second (17). The second, the Talbot Array Illuminator Spectrogram (TAIS), adds versatility and simplicity to optical time mapped spectrograms based on the Talbot effect by removing stringent hardware requirements (21; 22).

In this thesis, a framework for a time-frequency analyser specifically targeted to microwave signals is proposed using linear optics components, which provides the user with a high degree of versatility to customize the performance specifications depending on the demands of the application. A conceptual overview of the proposed framework is shown in Figure 1.1. A general mathematical framework connecting the TLS and the TAIS is shown and the characteristics and trade-offs of each spectrogram are considered through an extended study on both diagnostic and application-oriented microwave signals. The main results show that the TLS can achieve very large bandwidths and very narrow time resolutions. However, considering the constraints of the practical electro-optic components used for the temporal phase modulation, the TLS can so far achieve only a limited number of analysis points and frequency resolution. The TAIS overcomes this limitation using a smart multilevel wrapped design of the temporal phase modulation to easily achieve 40 times more analysis points, resulting in better frequency resolution. However, the TAIS is limited in maximal bandwidth and time resolution by other components involved. A full discussion of the trade-offs is found in Chapter 3.3 alongside Table 3.1. Thus, the TLS and the TAIS together present a range of possible design conditions to treat the most extreme ultrafast continuous broadband signals, implemented by the same hardware.

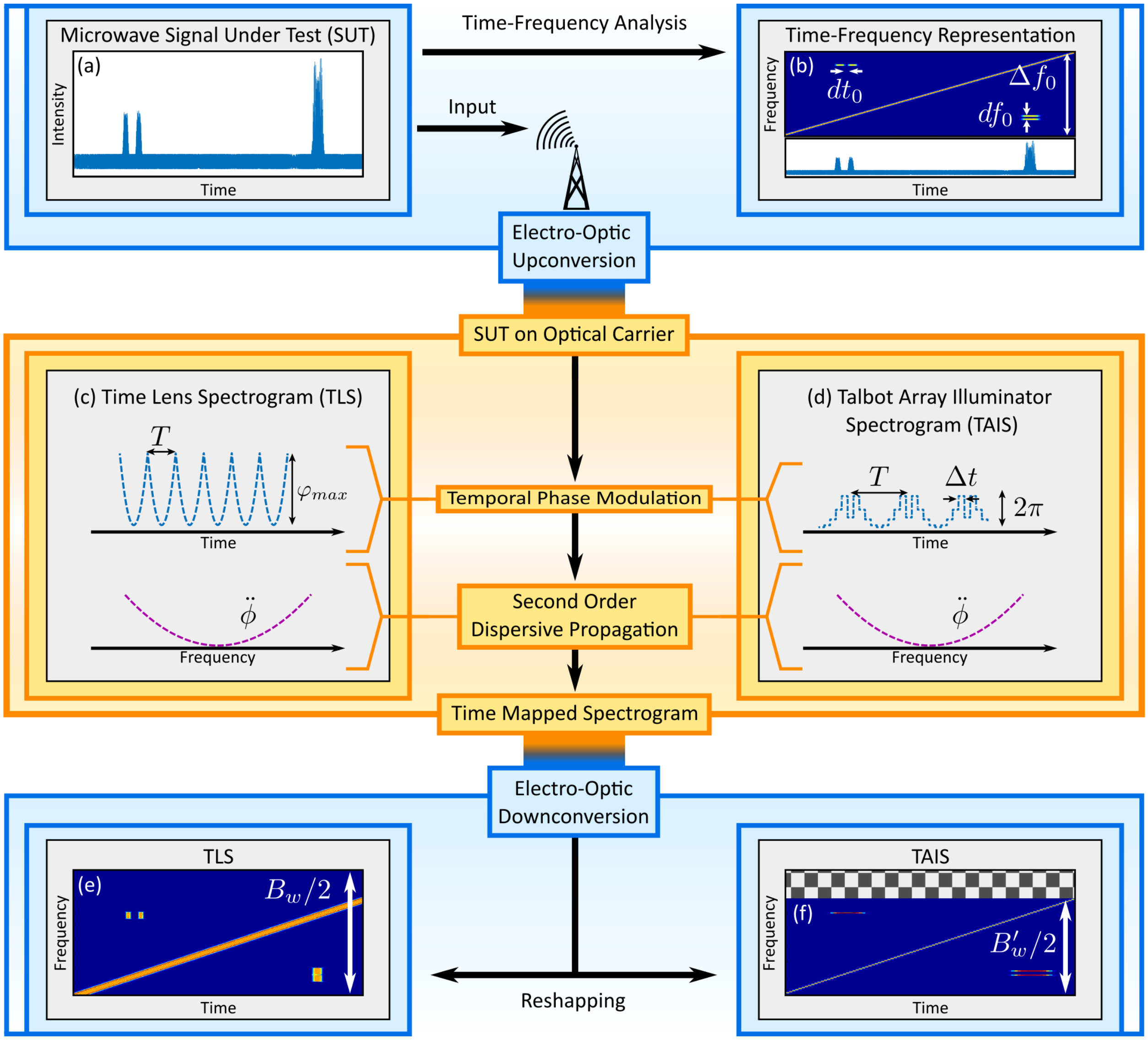

FIGURE 1.1 : Conceptual overview of the two photonics spectrograms. (a) Microwave SUT shown in intensity over time. (b) Features of the SUT in a time-frequency representation consisting of a linear chirp, two events closely spaced in time by dt_0, two events closely spaced in frequency df_0, over a microwave bandwidth of Δf_0. The signal is then upconverted to the optical domain by intensity modulation on an optical carrier. (c) The TLS consists of temporal phase modulation according to consecutive quadratic functions, followed by second order dispersive propagation to complete the time mapped Fourier transforms. (d) The TAIS is the same, with the exception that the temporal phase modulation is a discrete multi-level phase pattern wrapped to 2π with constant level period Δt. Electro-optic down conversion by a photodetector converts the signal back into the electrical domain. The time mapped consecutive Fourier transform output from the spectrograms is reshaped to place each Fourier transform vertically. This produces the frequency vs time 2D spectrogram image shown in (e) for the TLS, providing a larger analysis bandwidth B_w, and higher time resolution at the cost of analysis points (worse frequency resolution). The microwave signal is modulated onto the optical carrier in a way that results in symmetric double-sided spectra over a full bandwidth B_w, twice the DC to maximum frequency. (f) 2D plot for the TAIS, with a lower analysis bandwidth $B_w^{'}$ and worse time resolution, but with an improved frequency resolution and number of analysis points.

1.2 Thesis Objectives

The thesis is divided into 6 parts. Chapter 1, "Introduction", is an extended abstract which you just read. It includes a motivation, context, statement of the problem, and the solution which this thesis presents.

Chapter 2, "Background", introduces some of the more important concepts which are needed for the theory and results. This chapter includes what I consider to be the highlights of the history, development, and mathematics for the more essential aspects of the thesis, but is by no means exhaustive. The chapter begins with a very qualitative analogy, using music and the human ear to introduce notions relating to time-frequency analysis. This analogy is made more rigorous in the following section, giving an introduction to the history and mathematics of Fourier analysis. From Fourier analysis and the frequency representation of waves, the uncertainty principle introduces the effects of finite time windows, and restates the ideas of time and frequency resolutions. The remaining three sections include three distinct ideas which are required for the theory and derivation chapter. The first of these briefly gives the mathematical definition of a spectrogram and its discrete version. The next section describes the time lens, beginning from the construction of a thin spatial lens. The final section describes the Talbot effect, and qualitatively explains the idea of the Talbot array illuminator (TAI).

Chapter 3, "Theory and Derivation", begins with the theoretical derivation for the TLS, arriving at the definition of the spectrogram previously defined in the background chapter. Then, by discretizing the spectrogram and working backwards, a discrete phase pattern is found. The discrete phase pattern, which is a discretized version of the time lens, is found to satisfy one of the TAI phase patterns and the surrounding relations. This connects the TLS and the TAIS as time-frequency representations. Then, the trade-offs for each spectrogram are stated considering available hardware. The chapter ends with some notes on expected nonidealities and their expected consequences.

Chapter 4, "Experiment", contains the experimental details for the majority of the data presented in the results chapter. The chapter begins with the general setup which is similar for both the TLS and the TAIS. Then, the traces of the individual phase modulation patterns used are displayed. Following this, details on how the results are displayed are discussed. Finally, some of the methods of calibrating the system are mentioned.

Chapter 5, "Results", contains the main contributions of the thesis. Firstly, the bandwidth of the TLS and TAIS are calibrated using a single frequency tone. Then, an increasing chirp and decreasing chirp are used to confirm the expected frequency resolution. The next section described the effect of limiting the detection and digitization bandwidth on the recovered spectrogram. In particular, these results demonstrate conclusively that a 6 GHz detector is capable of recovering the time-mapped spectrogram of a microwave signal occupying a range of frequencies from DC to 46 GHz. This super-bandwidth recovery phenomenon is then compared to the results for a digital signal processing scheme. The digital processing of the electronic signal is done offline, because no modern devices are sufficiently fast to analyse this signal. The difference between the recovered spectrograms highlights the advantage of the optical processing method rather than the digital processing orthodoxy. A signal with very short, asynchronous transients below 100 ps is then recovered by the TLS, which is well below the system's time resolution of 696 ps. This test also conclusively proves these spectrograms are gapless, in the sense that there are no gaps in acquisition and any event will be recovered, regardless of the time of arrival or synchronicity with the time lens array. Further short events are tested, in the form of frequency hopping signals. Over 20 simultaneous frequency channels are turned on and off at nanosecond speeds as a strong application oriented demonstration of the TLS and TAIS. Signals of this speed are only able to be recovered in real-time with photonics methods, but it remains challenging for these methods to realize a many-level hopping system (9; 23). Therefore, the speed of the TLS and the number of analysis points provided by the TAIS allow for orders of magnitude improvements even beyond other photonics methods for cognitive communications. A small final results section presents the recovery of optical signals, including arbitrary phase patterns, as an important extension of the TLS and TAIS array of potential applications. A significant body of results on optical signals are demonstrated in my previous publications, but are omitted here to retain the focus on microwave signals.

Chapter 6, "Conclusion", summarizes the main results of the thesis, and presents multiple directions for future work. This includes extending the phase modulation to more lenses, using different hardware, and further investigating the theoretical connections between the TLS and the TAIS. After this is a list of contributed journal publications, conference publications, and a pending patent.

2 BACKGROUND

This chapter serves to introduce the concepts involved in the remaining chapters. Readers who are familiar with the concept of time and frequency distributions, Fourier transforms, time lenses, the Talbot effect, and the TAI, can skip to the relevant section or directly to chapter 3, but may find the following explanations enjoyable just the same. The first section is a very general and qualitative introduction to the ideas relating to the spectrogram through music. The following two sections on Fourier analysis and the uncertainty principle make these qualitative ideas mathematical. This is in preparation for the mathematical description of the spectrogram, which is what the analog devices presented are trying to replicate. The remaining sections on the time lens and the Talbot effect (including the TAI) are not explicitly related to one another, but are nevertheless required background for the theory and results of the thesis.

2.1 Music: An Intuitive Example

Sheet music is the most intuitive example of a joint time-frequency representation (JTFR), and music humanity's earliest subject of time-frequency analysis. A musical piece loosely consists of a choice of notes (or frequencies) being played to make some pattern in time. In this way, to properly play a musical piece, a musician requires both frequency and time information. The oldest recorded instructions of this type for how music should be played are found on a cuneiform tablet from the Old Babylonian period (approximately 1900 to 1600 BCE) (24). While the cuneiform tablet is written instructions in sentence form, sheet music is a graphical representation (25). On a staff of modern

FIGURE 2.1 : Example of a standard piece of western sheet music. Three staffs are shown, with notes placed on bars (horizontal lines) at certain times. The symbol used for each note denotes the amount of time it should be played before the following one.

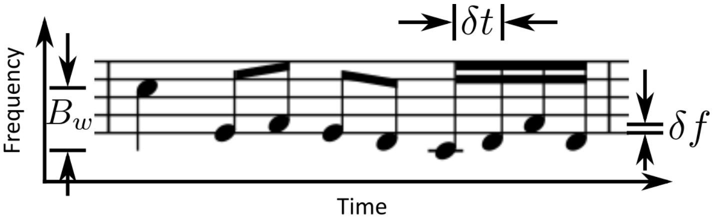

FIGURE 2.2 : Example of sheet music in the rough layout of a JTFR. The vertical axis is frequency increasing upwards, and the horizontal axis is time increasing to the right. This is also the layout which is used for most of the JTFRs in the Results 5 of this thesis. Assume that this sheet music was written with a musician of a particular skill level in mind, then these few bars displayed are a good representation of the whole piece. Then, the lowest to highest frequency would be known as the bandwidth B_w. Also, a tone to a semi-tone is the minimum frequency step, and an eighth note the shortest time interval to play a note, so the frequency resolution δf and time resolution δt are exactly these values.

sheet music, frequency is represented as increasing vertically by the horizontal bars, and time progressing to the right. The temporal duration of the notes is shown by using various symbols to denote ratios of an integer time signature, and placed on bars to associate them with standard tones as in Figure 2.1. This is exactly what is meant by a time-frequency representation.

Standard notes in western culture begin at 16.351 Hz (or cycles per second) which is approximately the lowest frequency that an average human ear can recognize as a frequency, and named C_0. The frequency which is double this (C_1 at 32.701 Hz), is denoted with the same letter, and the difference is called an octave, because the nomenclature cycles through 7 letters from A to G. This continues up until 16,744 Hz, or C_{10}, after 10 octaves which is approximately the highest frequency that an adult ear is capable of hearing. The way the other notes are divided into each octave can vary depending on the system used for the purpose of emphasizing the harmony between certain tones. The most common division of this entire frequency range is into 120 discrete frequency points, known as the chromatic scale (25). In calling sheet music a JTFR, one would be motivated to make more associations. This is shown in Figure 2.2, where the analogy is visually shown. The bandwidth of the JTFR would be the difference between the highest and the lowest frequencies, or 16,744 Hz - 16.351 Hz. The frequency resolution would be the bandwidth divided by the number of divisions. It is here the first problem is encountered, as in the chromatic scale the frequency resolution would actually be varying, increasing with frequency (the equal temperament scale has a logarithmically constant step size). This is the only way in which sheet music is sometimes less intuitive and more complicated than the JTFRs to come. In a simple JTFR, the minimum discernable step size or difference between any two frequencies is known as the frequency resolution, and it will be constant for the developments of this thesis. On the temporal side of things, it is technically possible to have a never ending song, as most people who have been on a road trip will be familiar with. Maximum temporal widths are defined for many JTFRs, but for an ideal system it is desirable to not have this limitation. The time resolution then is the minimum time step which one can define on the staff, which is around a 256^{th} note for human musicians. Along with the bandwidth, time width, frequency and time resolutions, there is one more interesting parameter that can be specified for sheet music. With all the information above for a specific piece, a musician may still wonder: how loud are they to play each note? In sheet music there are 8 levels of intensity for each note, from pianissimo to fortissimo. In JTFRs, the ratio of fortissimo to pianissimo would be known as dynamic range, where as the number of intensity levels (in the case of discrete levels) would be known as bit depth.

Sheet music is an easy and intuitive visual example of a JTFR which makes it clear to musicians how to play a piece of music. Considering the amount of effort composers undergo to create this representation, it may seem curious as to how appreciating a melody comes so naturally to so many without formative training in musical theory. The answer is that humans each have organs designed specifically to create JTFRs. The human ear is a remarkably complex system, and the process by which it converts pressure waves in the air into neural stimuli, quite surprising. Inside the human ear there is a spiral structure containing approximately 15,000 hair cells known as cilia. These cilia are of varying lengths and arrangements, which are stimulated by varying frequencies of pressure waves from sound. The stimulated cilia create DC and AC currents, which result in activating nerve fibers leading to the brain. The cilia of the outer regions of the spiral are activated by high frequencies (around 16,000 Hz for a healthy adult), while the center of the spiral is activated by low frequencies (around 16 Hz). As a note of music enters the ear, it stimulates the cilia based on frequency for the duration of the note, and so frequency and time information is simultaneously sent to the brain. With these cilia the human ear can recognize more than 1,400 distinct frequencies (25). It would be reasonable then to say that musical notation, or equivalently the musicians' ability to read it, has not yet caught up to the capabilities of the human ear. The minimum temporal duration a tone is required to play so as to be recognized as a tone, rather than as a click or beep, is approximately 13 milliseconds (the time resolution). On average, adults may be able to recognize two frequencies spaced apart by a few Hz (the frequency resolution) depending on the frequency range considered. The longest duration sound a human can hear is bounded by their lifetimes, but more typically by their attention spans. Finally, the frequency bandwidth of the human ear tends to decrease with age, beginning with the highest frequencies.

I hope with the analogies to sheet music and the functioning of the human ear that JTFRs have become much less mysterious. Extending the notions of bandwidth, time and frequency resolutions for signals other than audio is a small conceptual jump. It requires only forgetting about some details of the physical nature of the wave under consideration, as well as the devices doing the processing. In speech and music signals the frequencies discussed have been in the Hz to tens of kHz range, time durations from milliseconds to minutes, and the processing devices the ear and brain. For microwave signals, as is the subject of this thesis, the frequencies studied will be in the MHz to hundreds of GHz range, time durations from picoseconds to microseconds, and the processing devices optics and high speed electronics.

2.2 Fourier Analysis

The ideas of JTFRs are made rigorous by Fourier analysis and the eponymous Joseph Fourier. Born in France in 1768 (26), Jean-Baptiste Joseph Fourier is known for (among other things) his theory of heat, developed, coincidentally, after spending roughly 3 years as governor of lower Egypt at the request of Napoleon Bonaparte (27). The results of Fourier's theory of heat depended on the technique he developed of treating any function (e.g., even, odd, periodic, non-periodic, and even discontinuous with some additional conditions), as an infinite sum of trigonometric functions like sine or cosine. Fourier even demonstrated how an even function, cosine, could be written as a sum of odd functions, sines. This result is unsurprisingly not the start nor the finish line, but is part of a long line of people and cultures devoting their lives to what is known as harmonic analysis. Many previous contributions in using trigonometric functions to solve problems set the stage for Fourier's development, by mathematical giants such as Joseph-Luis Lagrange (Fourier's professor), Carl Friedrich Gauss, Leonhard Euler, and Jean le Rond d'Alembert.

Relating this technique to the previous section, Fourier's results imply that a piece of music, which when played produces a function of pressure over time in the air, would be able to be completely described by a sum of sine or cosine waves with varying weights. This is maybe not surprising in the case of music, where it is already natural to talk about frequencies and waves. The real power of this technique is that it was ultimately generalized to all functions, not just periodic structures like waves. There are many conceptual angles from which to view the Fourier transform. The simplest may be to think of the Fourier transform as an algorithm which takes a function, and returns the weights of all the different waves of all possible frequencies required to create it. This is done in a unique way, such that for a function f of a variable x defined on an interval of length l, there should only be one possible representation in terms of sums of sines, for example. This statement would be mathematically written in the following way.

$$f(x) = c_0 + c_1 \sin\left(\frac{2\pi x}{l}\right) + c_2 \sin\left(\frac{2\pi 2x}{l}\right) + c_3 \sin\left(\frac{2\pi 3x}{l}\right) + ... \tag{2.1}$$

or equivalently using summation notation,

$$f(x) = c_0 + \sum_{n=1}^{\infty} c_n \sin\left(\frac{2\pi n x}{l}\right). \tag{2.2}$$

Here the capital sigma, $\sum$, represents the summation of all terms, with n going from 1 to ∞. The c_0 term is referred to as the constant or DC (Direct Current) term, and can also be thought of as the sine wave with frequency zero. Physically this represents a vertical offset of the resulting wave. The graphical representation of what this equation represents is shown in Figure 2.3. The "amount" of each frequency is given by the weights c_n. Constructing any function $f(x)$ defined on an interval amounts to finding the correct weights of each frequency. The weights can be calculated using

$$c_n = \frac{2}{l}\int_0^l f(x)\sin\left(\frac{2\pi nx}{l}\right)dx. \tag{2.3}$$

I won't derive this relation, but it can be done by multiplying both sides of equation 2.2 by $\sin(2\pi mx/l)$ and then integrating over the interval. After using a trigonometric identity, the integrals will all be zero with the exception of where $m = n$, when the integral is $l/2$. This is known as the orthogonality property of the Fourier sine series. In the language of linear algebra, sines and cosines form a basis for the space of functions defined on an interval. That is to say, with the set of all sines and cosines with frequencies integer multiples of the fundamental, it is possible to construct every possible function on the interval. In the same language, one can think of the coefficients calculated by equation 2.3 as projections of a general vector $f(x)$ onto the basis vector $\sin(2\pi nx/l)$. In a usual projection of two vectors, the binary operation known as the dot product is used, but here since the vectors are functions, integration of their product is used instead. Returning to plain language, this equation can be summarized as: how much of $\sin(2\pi nx/l)$ is in $f(x)$?

I will use a simple example to demonstrate these ideas further, computationally and graphically. Consider that the function $f(x)$ to be approximated is the function according to Figure 2.4.

This simple step function is shown in Figure 2.5. Calculate the equation for a general term c_n by using the definition of $f(x)$ from 2.4 and equation 2.3, and separating the integral into two parts,

$$\begin{aligned}
c_n &= \frac{2}{l}\left[\int_0^{l/2} 1\sin\left(\frac{2\pi nx}{l}\right)dx + \int_{l/2}^{l} -1\sin\left(\frac{2\pi nx}{l}\right)dx\right] && (2.5)\\
&= \frac{2}{l}\left[-\frac{l}{2\pi n}\cos\left(\frac{2\pi nx}{l}\right)\right]_0^{l/2} + \frac{2}{l}\left[\frac{l}{2\pi n}\cos\left(\frac{2\pi nx}{l}\right)\right]_{l/2}^{l} && (2.6)\\
&= \frac{1}{\pi n}\left[-\cos(\pi n) + \cos(0) + \cos(2\pi n) - \cos(\pi n)\right] && (2.7)\\
&= \boxed{\frac{2}{\pi n}\left[1 - (-1)^n\right]}. && (2.8)
\end{aligned}$$

There are two things to notice about this final result. The first is that c_n gets smaller as n increases based on a multiple of the harmonic series, meaning higher frequencies become less significant. The second is that when n is even, $c_n = 0$. This is expected as all sines with even multiples of the fundamental mode would contribute to constructing a function which is periodic with $l/2$, which $f(x)$ is not. One can, after finding the weights, write the first few terms of the Fourier series.

$$f(x) = \frac{4}{\pi}\sin\left(\frac{2\pi x}{l}\right) + 0\sin\left(\frac{2\pi 2x}{l}\right) + \frac{4}{3\pi}\sin\left(\frac{2\pi 3x}{l}\right) + 0\sin\left(\frac{2\pi 4x}{l}\right) + \frac{4}{5\pi}\sin\left(\frac{2\pi 5x}{l}\right) + ... \tag{2.9}$$

or equivalently in the following summation notation,

$$f(x) = \sum_{n=1}^{\infty}\frac{4}{\pi(2n-1)}\sin\left(\frac{2\pi(2n-1)x}{l}\right), \tag{2.10}$$

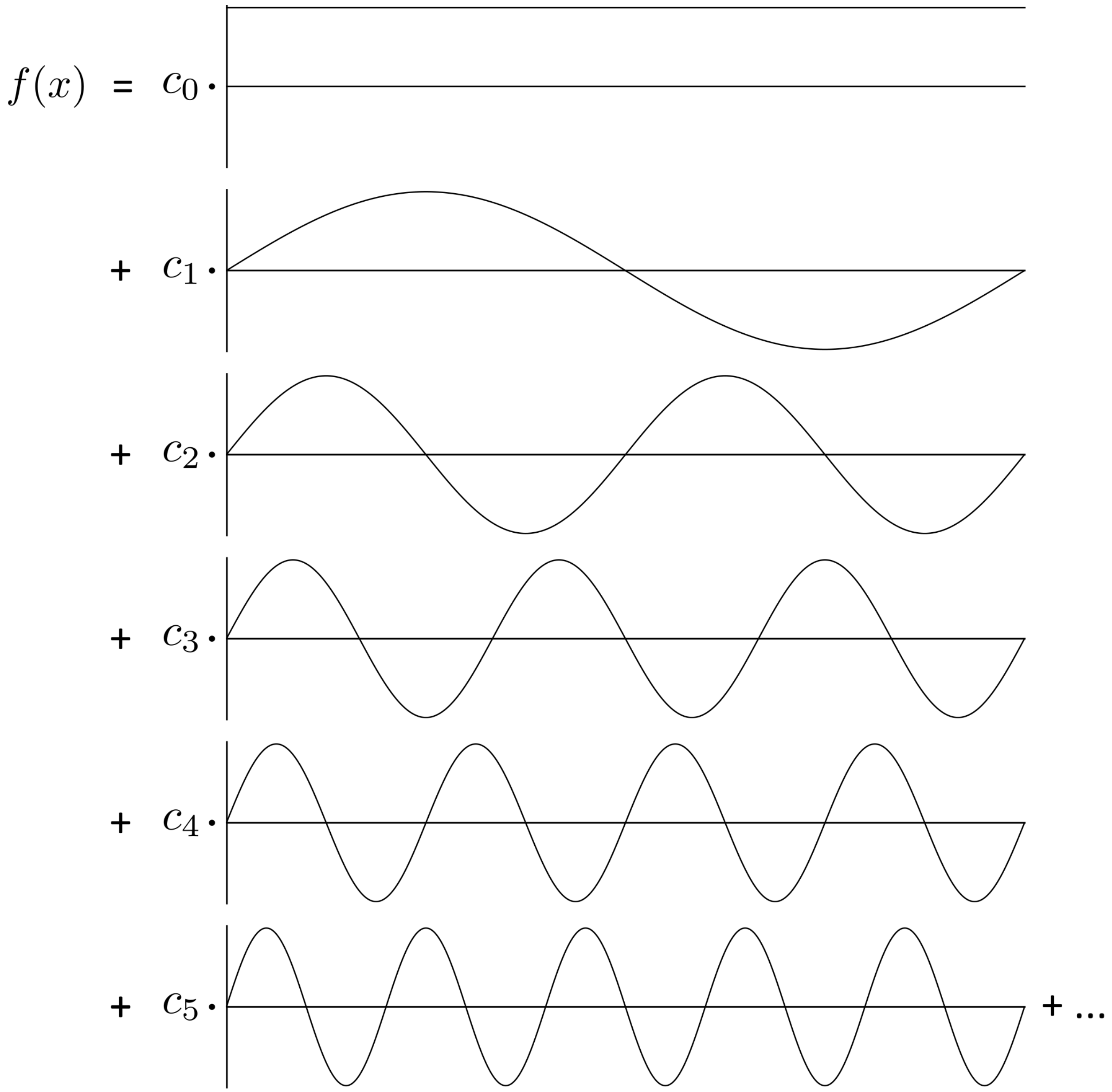

FIGURE 2.3 : Graphical representation of the Fourier sinusoid series. Any periodic function $f(x)$ can be constructed by an infinite sum of sine functions with weights c_n for $n \in \{0, ..., \infty\}$. Each sine has an increasing frequency such that the n$^{\text{th}}$ contains n times as many cycles as the fundamental frequency. The c_0 term is the constant term which allows for arbitrary vertical offsets, and is considered to be "zero" frequency. The fundamental frequency is defined by the interval over which the function is defined.

$$f(x) = \left\{ \begin{array}{lll} 1, & \text{if} & x < l/2 \\ -1, & \text{if} & x \geq l/2 \end{array} \right\} \tag{2.4}$$

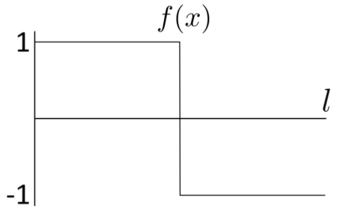

FIGURE 2.4 : Piecewise equation and graph of a simple decreasing step function. The function is only defined on the interval between $0 \leq x \leq l$.

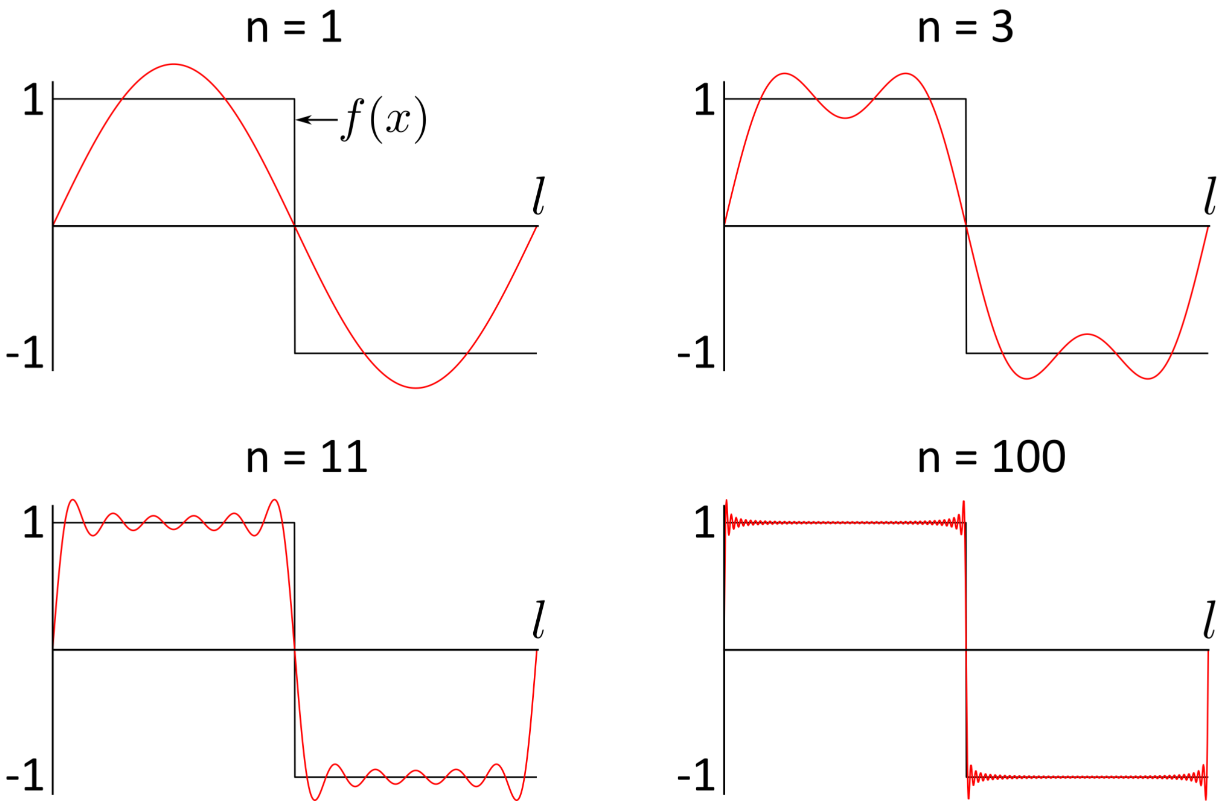

FIGURE 2.5 : Partial sums of the Fourier sine series for a step function $f(x)$ defined as in equation 2.4. Four approximations are shown, the first when there is only the fundamental frequency mode. The second for n = 3 is when the fundamental and 3 times the fundamental are summed. The third n = 11 contains 6 nonzero summation terms and is beginning to look like $f(x)$. The fourth is when n = 100 and the step function is well approximated by the partial sum including 49 nonzero terms.

where the odd terms are all ignored by the inclusion of $2n-1$. The partial Fourier sums, calculating up until n = 1, 3, 11, and 100, are shown in Figure 2.5. Increasing the number of terms in the sum, it is seen how smooth sines can begin to approximate a sharp step function. As an extra detail, an interesting artifact occurs near the edges of the step. The approximation seems to be overshooting, with an increasingly sharp peak near the step at $x = l/2$. This is known as the Gibbs phenomenon (28), named after Josiah Gibbs who was one of the mathematicians and physicists to investigate these features in the late 1800s and early 1900s. Although it can be shown mathematically that the approximation does converge in the limit, two qualitative observations can argue for not worrying about the overshoot. Firstly, notice the value of every term in the approximation is exactly zero, and thus the value of the approximation will always be zero at that point, as expected from the function to be approximated. Secondly, even though the overshoot of the approximation near the point $x = l/2$ persists for all approximations with finite terms, the measured "area" or integral difference between the approximation and the function rapidly approaches zero.

Up until now, only the interval $0 \leq x \leq l$ has been considered. The only goal was to approximate $f(x)$ well on this interval alone. But the sine function is well defined for the entire real number line $(-\infty, \infty)$, as are all of the c_n defined. Therefore, it is possible to see what the discrete sum results

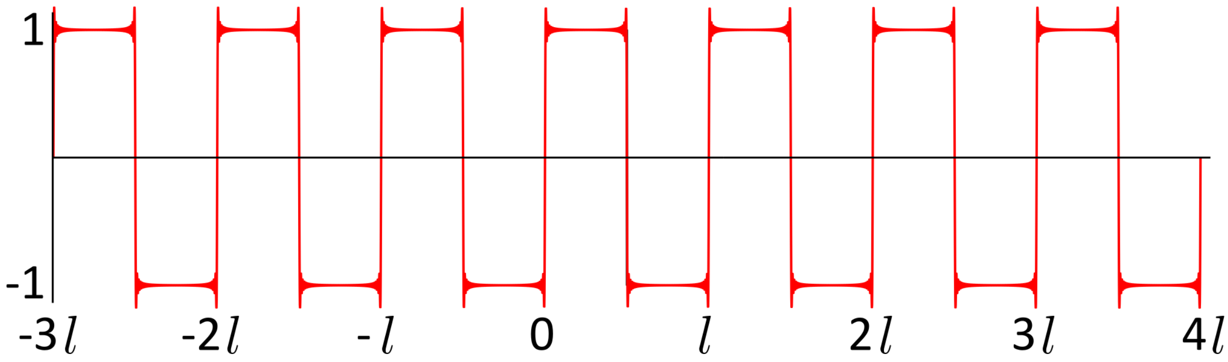

FIGURE 2.6 : Fourier series shown on a larger interval than the original function $f(x)$ was defined on. The periodicity of the n = 100 partial sum is clearly seen for every l.

in for a larger interval, to gain a better understanding of the Fourier series. This extension onto the interval $-3 \leq x \leq 4$ is shown in Figure 2.6. This figure reveals something very crucial to understand about the Fourier series, and also applies to the more general Fourier transform yet to be defined. The key is that the Fourier representation of a periodic function is discrete, and conversely the Fourier representation of a discrete function is periodic (29; 30). This naturally alludes to the following question: what is the Fourier representation (or transform) of a continuous, nonperiodic function?

It is reasonable to conjecture that the Fourier transform of a nonperiodic function defined over the whole real number line $(-\infty, \infty)$ would necessarily include a continuous range of frequencies, rather than a discrete number by integer jumps as in the previous example. Consider the following qualitative argument for this. Extend the interval over which the previous function $f(x)$ is defined; what would that do to the fundamental frequency? The frequency of the first sine was one cycle for every l, or $f_1 = 1/l$. The next frequency was necessarily twice this, or $f_2 = 2/l$. Now compute the limit as the interval of definition becomes infinite:

$$\lim_{l \to \infty} \frac{1}{l} = 0, \tag{2.11}$$

$$\lim_{l \to \infty} (f_{n+1} - f_n) = \frac{1}{l} = 0. \tag{2.12}$$

As a larger interval of definition is considered, the fundamental frequency becomes infinitesimal. The step between any two consecutive frequencies also becomes infinitesimal. This is not a rigorous proof but it should be sufficient to give a conceptual understanding as to why an aperiodic signal will not have a Fourier representation which is able to be described by discrete frequencies. This has then sufficiently motivated, although not proved, the following definition for the Fourier transform $\mathcal{F}$ of a function $g(x)$.

$$\mathcal{F}\{g(x)\} = \int_{-\infty}^{\infty} g(x) e^{-i2\pi f x} dx, \tag{2.13}$$

where the integral is a summation, but over a continuous frequency parameter f, rather than discrete steps. I have also now switched to the exponential notation for a wave, which comes from Euler's formula,

$$e^{i\theta} = \cos(\theta) + i\sin(\theta). \tag{2.14}$$

Equation 2.13 gives the "coefficients" of the wave $exp(-i2\pi fx)$. See section 5.7 for a very brief note on the use of complex notation in the Fourier transform. Together these coefficients create a continuous function in frequency space, where the image of the function is the "amount" of that frequency contained in the function $g(x)$. This is the standard procedure in linear algebra for a change of basis operation, changing how the vector (function in this case) is represented. To recreate any function $g(x)$, one may use a sum of all the waves along with their weights, given by a function which will be called $G(f)$, in the following way.

$$g(x) = \int_{-\infty}^{\infty} G(f)e^{i2\pi fx}df \tag{2.15}$$

is aptly named the synthesis equation, because it is used to synthesize any function $g(x)$ desired. The interpretation and specific nomenclature for the frequency f depends on the wave or function being considered. For example, if x is a variable of time t, then f is cycles per unit time, also known as Hz. If x is a unit of length, then f becomes a spatial frequency, cycles per length. x could also be units of frequency, then f would have the units of time or space, and the whole process would be flipped on its head. In the following sections, some properties of the Fourier transform and ways to use it for even more general analysis will be explored.

2.3 Windowing and the Uncertainty Principle

The previous section described with a simple example how the interval over which a function is defined specifies a fundamental or minimum frequency which can contribute to the synthesis of that function. This is known as the uncertainty principle of classical wave theory. Qualitatively, for a function of a specified time duration, there is not enough time for slower waves to exist as full cycles. This becomes important when only a finite window of the function is available or chosen to be analysed by the Fourier transform. In practice, a window function is used when one is interested in the frequencies contained within a certain time (or length) of a function, rather than the entire function. The most basic example is a rectangular cutoff function which is unity within the region of interest, and zero everywhere else. A good physical example of a window function is a window, which only allows light through a rectangular hole in a wall. Both of these examples are shown in Figure 2.7.

From the perspective of the Fourier transform, a window function is usually a non-periodic function with zeros everywhere except for a short time within the window of analysis. Therefore, it is expected from the discussion of the previous section 2.2 that the Fourier transform should

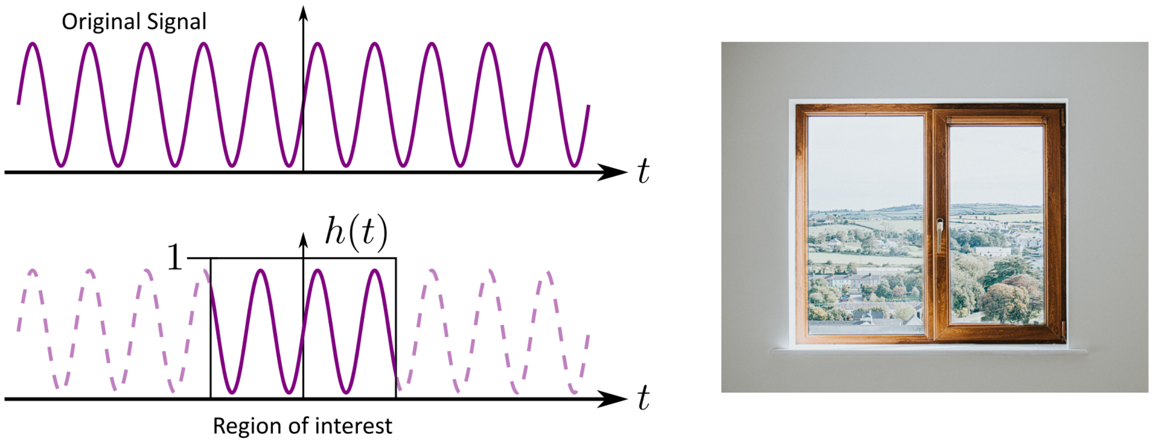

FIGURE 2.7 : Two basic examples of signal windowing. The first case, a sine wave is windowed by a function $h(t)$ which is equal to one in the region of interest and zero everywhere else. In the second example, the walls block the landscape, while area of the window permits light to pass virtually unchanged.

in general not be discrete. If the function within the window is itself a periodic structure then the Fourier transform will also be periodic over a certain number of periods determined by the number of periods falling within the window. The fundamental minimum frequency difference between any two frequencies in the Fourier transform is defined by the window in a similar way as in the previous section 2.2. Although now for a continuous spectrum, the steps between frequencies will be not be discrete, but continuous and blurred depending specifically on what shape of analysis window has been chosen. For this entire thesis, only the case of the rectangular window will be employed, without including more advanced windowing functions such as triangular, cosine, or others (31). A rectangular window of size T is defined as

$$R(t) = \left\{ \begin{array}{ll} 0, & \text{if} \quad t > |1/2| \\ 1, & \text{if} \quad t \leq |1/2| \end{array} \right\}. \tag{2.16}$$

For this rectangular window, the fundamental minimum frequency, or equivalently frequency resolution, can be reasonably defined as

$$f_T = \delta f = 1/T. \tag{2.17}$$

One other popular choice for a windowing function is a Gaussian function (or normal distribution). This is because a Gaussian is self similar to its image under a Fourier transform, meaning the Fourier transform of a Gaussian is simply a scaled Gaussian over a different variable. The Fourier transform of the window is particularly important due to the convolution theorem,

$$\mathcal{F}\{g(t) \cdot h(t)\} = \mathcal{F}\{g(t)\} * \mathcal{F}\{h(t)\}, \tag{2.18}$$

where $g(t)$ is the signal of interest, multiplied by the window function $h(t)$. The operation on the right hand side of the equation is convolution, defined for two functions $n(t)$ and $m(t)$ as

$$(n * m)(t) \equiv \int_{-\infty}^{\infty} n(\tau) \cdot m(t - \tau) d\tau. \tag{2.19}$$

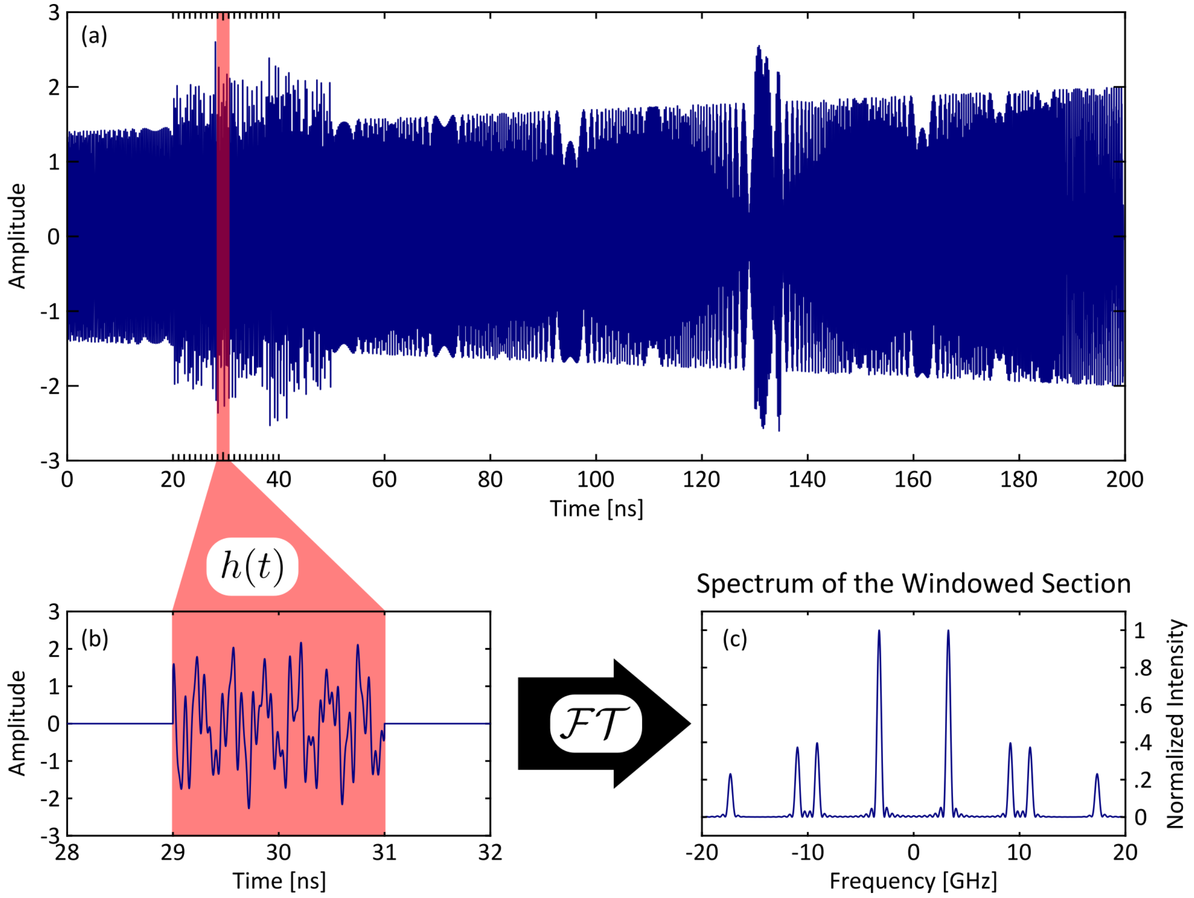

Figure 2.8 : (a) A signal with fast features over 200 ns. For the long signal shown in (a), maybe there is one small section of interest, highlighted with a thin red box in (a), or maybe there is interest in seeing what frequencies occur within that short time. (b) The long signal from (a) is windowed by a function $h(t)$ to isolate the region of interest. Here $h(t)$ is just a rectangle with height equal to one and width equal to 2 ns. (c) The Fourier transform of this windowed region of interest is computed and displayed. Notice the spectrum is symmetric around 0 GHz, which is an expected feature of the Fourier transform.

This theorem states that the Fourier transform of point-wise multiplication of two nicely defined functions is equivalent to the convolution of their Fourier transforms. Put more concisely, multiplication in one domain is convolution in the Fourier domain. For a fun result on rectangular windowing functions, see the appendix 7.1. This theorem implies that the windowing function chosen produces predictable features after the windowed signal is Fourier transformed. This can be seen in Figure 2.8, where a region of interest is isolated from a long signal in 2.8(a) by multiplying with a rectangular window function, the result of which is shown in 2.8(b). After the Fourier transform, the spectrum in 2.8(c) contains multiple sharp peaks, indicating multiple very narrow frequency lines. The frequency lines are not infinitely narrow, and have some width, expected from the finite duration of the windowing function used. In fact, the shape of the peaks will closely resemble the shape of $sinc$ functions, as the $sinc$ is the Fourier transform of a rectangular window.

Consider modifying the size of the window in Figure 2.8(b) by a factor of 4 to 0.5 ns as in Figure 2.9 (a). The expectation from 2.17 is that the frequency resolution should worsen by a factor of approximately 4, which is confirmed by Figure 2.9(b). Therefore reducing the window size

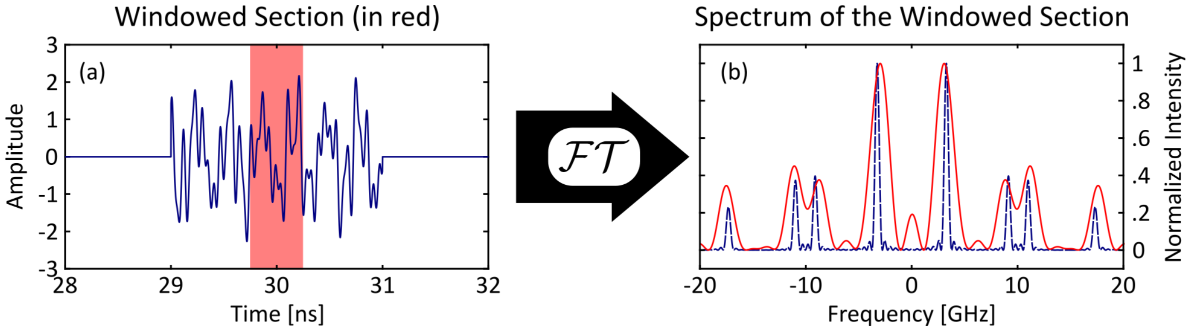

FIGURE 2.9 : (a) A four times smaller window of 0.5 ns width is used to take only a smaller part of the SUT (red shaded area). (b) The Fourier transform of the smaller time section produces a spectrum with four times worse frequency resolution, shown as a red solid line, and is compared to the spectrum of the larger window shown in a blue dashed line.

worsens the frequency resolution, while increasing the window size makes it better. Notice also if the goal is to localize certain frequency components to a short time of the signal, then reducing the window size allows for a better estimate of timing, while taking larger sections of the signal does not provide as good temporal resolution. This is the way in which time and frequency resolutions are considered in classical wave theory to be inversely proportional. Explicitly, the uncertainty principle is

$$\delta f \cdot \delta t = 1. \tag{2.20}$$

There are many more considerations which have not been mentioned, for example, the use of standard deviations to improve the estimates of the resolutions, or the full-width half-maximum points. Ultimately, whether or not certain frequencies or time events can be resolved from one another involves an element of subjective observation. As long as the specific resolution used is reasonable and made clear at the beginning, there should be little confusion. In this thesis, the time resolution will be defined as the width of the rectangular window (and in this thesis, only rectangular windows are used), while the frequency resolution will be defined as the inverse of the time resolution as in 2.20.

2.4 Spectrogram Analysis

While the Fourier transform of the windowed signal in Figure 2.8 displays the frequency content within that window, recall the goal of JTFRs is to describe how the frequency content of a signal evolves over time. Therefore, repeating this process for multiple windows at different parts of the signal will allow for the frequency content to be sampled those various parts. This idea leads naturally to the short time Fourier transform (STFT) of a signal (defined in 2.22). Assume that no two windows overlap with one another, and that windows are placed edge to edge so that every part of the function falls under one of the analysis windows (gapless). Then the STFT process will be carried out as in Figure 2.10. The consecutive rectangular windows are shown in Figure 2.10(b), and each one must be Fourier transformed separately if all the information of the signal is to be recovered. Explicitly, if there were some fast event happening between the two example spectra shown in Figure 2.10(c) and 2.10(d), and if the segments in between were discarded rather than transformed, that fast transient event would be lost. For the example shown in Figure 2.10, the computational intensity of the STFT process is evident. Each window is only 2 ns long. Therefore, if the signal is to be processed in real time, each Fourier transform must be computed in that same time. Currently, this is far beyond the capabilities of digital electronic signal processing (computers) (13). There are some methods which allow for parallel systems to evenly distribute the workload among multiple processing units by taking short sampled segments of the signal and slowing them down (12). However, the real time spectrum analyser stage to do the Fourier transform in the digital domain is still required. Assuming the fastest speeds of those digital devices, in the millions or tens of millions of Fourier transforms per second, then 100 to 1000 devices and parallel optical systems would be needed to compare to the results shown in this thesis (over a billion Fourier transforms per second for a continuous and gapless signal in real time, without digital signal processing).

By visually inspecting the temporal trace of the signal in Figure 2.10(a), or by inspecting the complete spectrum of the signal (all frequencies contained within the signal) as in Figure 2.11, it is still not obvious what features comprise this signal. I guarantee you cannot predict how this signal was constructed, but it will become perfectly clear after plotting the JTFR. For this signal, the spectrogram is chosen as the JTFR rather than the STFT. There is a slight difference between the two, but one is calculated from the other. In particular, the spectrogram $SPGM(t, f)$ is a JTFR with dependence on time and frequency defined as follows:

$$SPGM(t, f) = |STFT(t, f)|^2, \tag{2.21}$$

where the $STFT$ stands for the short time Fourier transform, and is defined as

$$STFT(t, f) = \int_{-\infty}^{\infty} a(\tau)h(\tau - t)e^{-i2\pi f\tau}\, d\tau, \tag{2.22}$$

where $h(t)$ is the window function, $a(t)$ is the full signal, and the product of the two is Fourier transformed using the definition from section 2.2 in 2.13. Simply put, the spectrogram is the intensity of the STFT, which due to the Fourier transform, returns complex values. The spectrogram of the example SUT is shown in Figure 2.12. In a similar way to sheet music, section 2.1, all the components of the signal can be observed upon immediate visual inspection. In particular, the signal consists of a downwards linear frequency chirp from 20 GHz to around 2.5 GHz, increasing in intensity, an upwards quadratic chirp from 3 GHz to around 14.5 GHz and constant intensity, a fast transient event at 12 GHz at the time where the two chirps cross, and finally, a time-frequency smiley face.

Very briefly, it was mentioned that the consecutive Fourier transforms are a computationally demanding process for digital electronics (and for the example in Figure 2.10, not possible with modern methods). In the next section, a well known analog method for computing individual Fourier

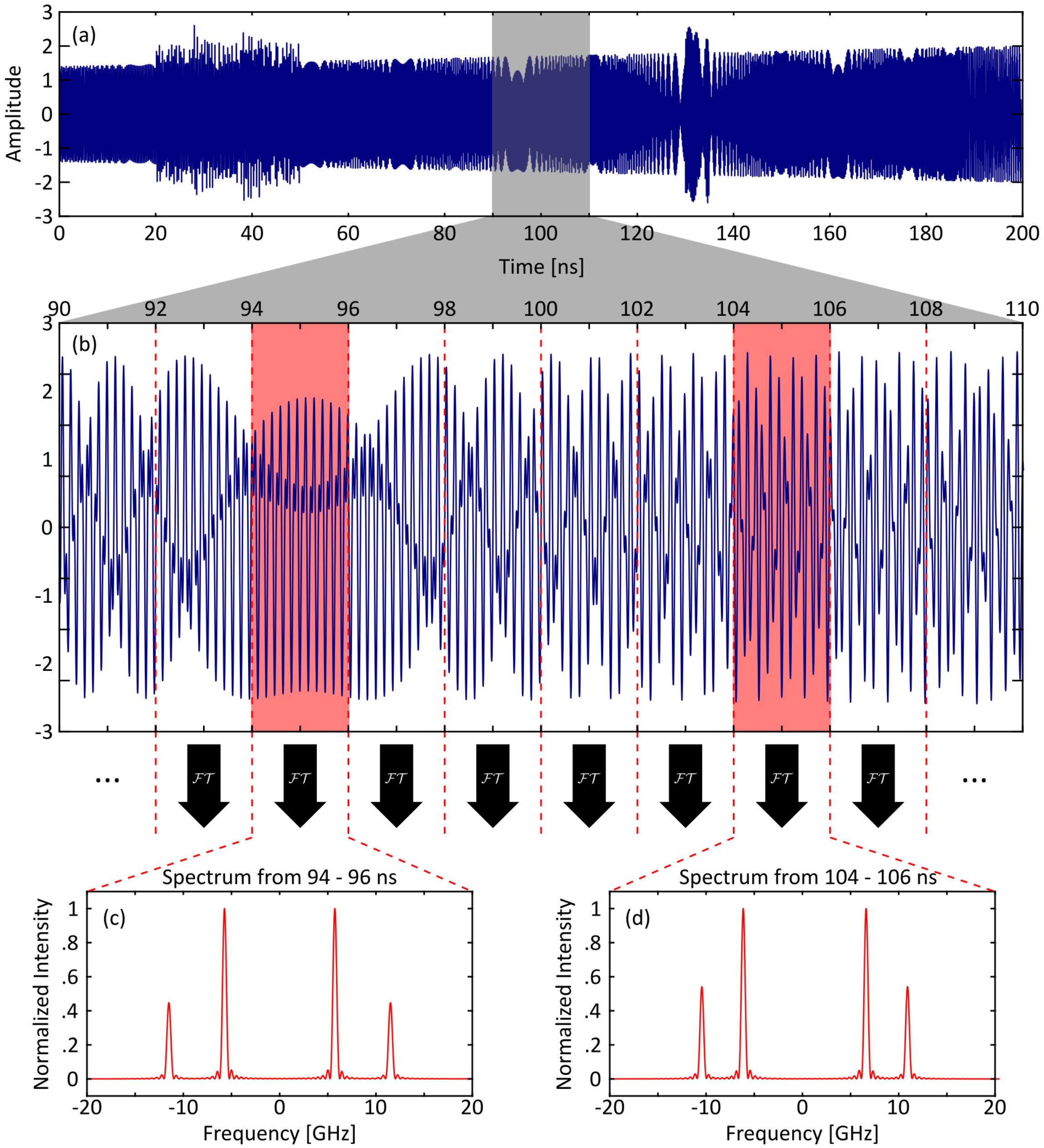

FIGURE 2.10 : (a) A SUT with fast interfering features. (b) A blown up section of the signal to show the windowing process by taking consecutive windows of 2 ns and performing the Fourier transform on each one. (c), (d) The results of the Fourier transform for two windows, shown in shaded red in (b), are displayed, showing fairly similar spectra.

transforms, the Time Lens, is discussed. It would remain after this discussion to find a way to use the analog method for gapless analysis, which is one of the major contributions of this thesis.

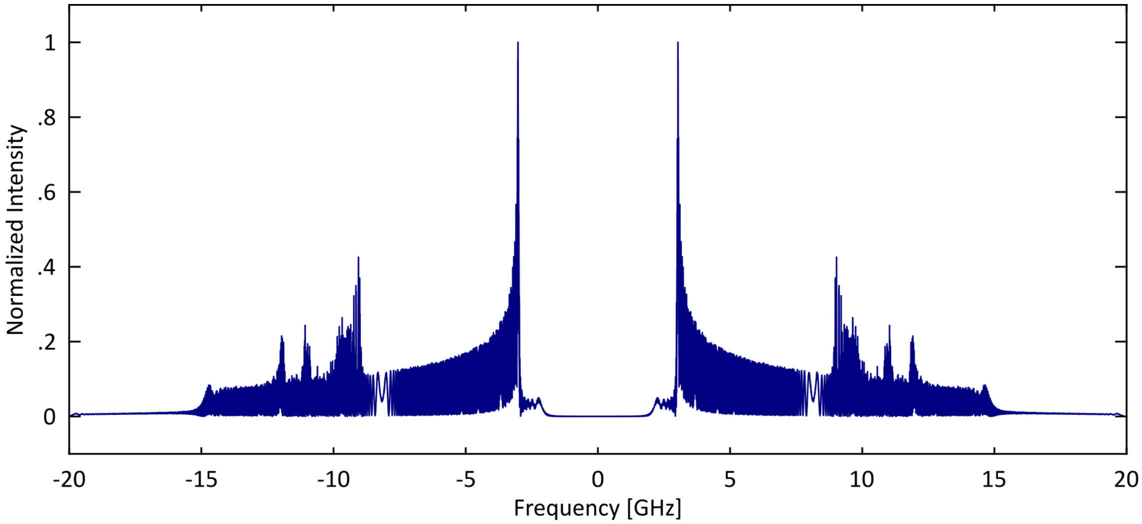

FIGURE 2.11 : The Fourier transform of the entire SUT shown in 2.10(a) is displayed.

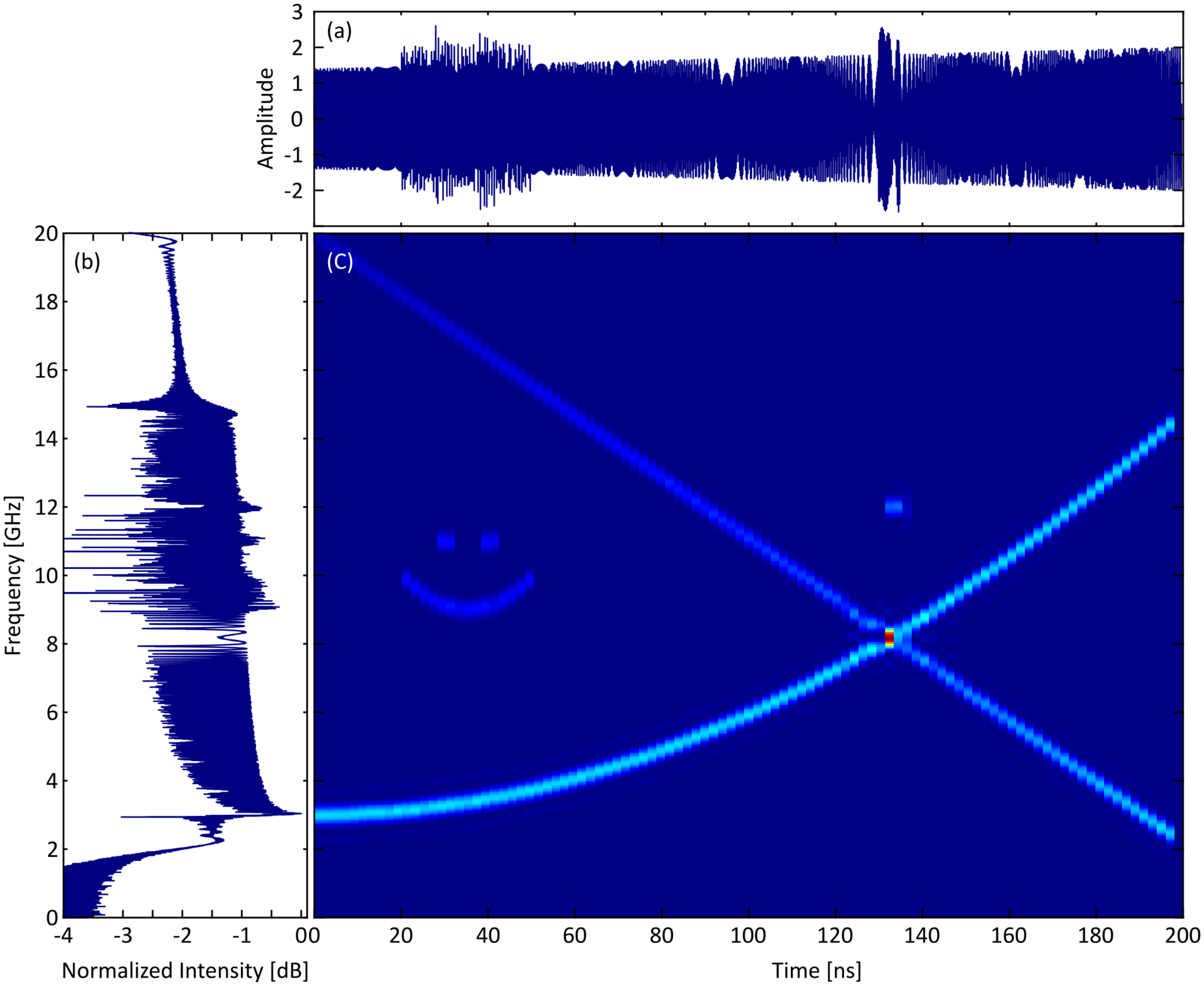

FIGURE 2.12 : (a) The temporal trace of an example signal. (b) Positive spectrum of the entire signal in logarithmic units. (c) Spectrogram (absolute square of the STFT). All the time-frequency features that were used to construct this example signal are shown clearly by visual inspection.

2.5 Time Lenses

In one sentence, a time lens does exactly the same operation as a thin spatial lens, but over the domain of time rather than space. In ray optics, a spatial lens with diffraction focuses light to a point. In physical optics, which provides a more accurate model of electromagnetic phenomenon, a thin spatial lens with diffraction does a Fourier transform. If the lens is large enough, the Fourier transform begins to look more and more like it is converging to a point. In this section, the Fourier transforming property of a thin spatial lens system will not be proved, since there are many textbooks which already discuss this in great detail (32; 33). Instead, this section will elaborate on space-time duality, temporal imaging, and frequency to time mapping.

It was observed in the late 1960s that the problems of light propagation in both space and time are very mathematically similar (34; 35), under certain approximations. This mathematical similarity is the cause for the parallelism in nomenclature, known as the space-time duality. Significant contributions were made by Brian Kolner in developing the analogy and properly defining terms such as focal lengths and magnification factors in the time domain (36; 19; 37). This work followed extensive studies into chirped radar and analog electronic signal processing (38; 39). As a result of these works, space-time duality has been heavily relied on in the field of optical signal processing (40; 20; 41).

For both the case of time and of space, the actual observable property of the light for most simple experiments is often the power, rather than the electromagnetic oscillations that light is known to be. One of the reasons for this is that optical and infrared light used in both imaging and fiber optic communications oscillates at upwards of 100 THz. Observing these oscillations directly is not obvious, although there are successful modern techniques involving interferometry. The "Wizard of Schenectady" Charles Steinmetz gives an impressively intuitive motivation for using exponential wave notation, specifically due to the primary observable of light being power (42). He notes that, for a monochromatic wave being made up of primarily a single frequency, separating the fast oscillations into a phasor notation is extremely useful. In this notation, the amplitude of the wave at any point is known as the phase, and the absolute square of the amplitude is the intensity, which relates to power. This definition (phase as exactly the amplitude of a wave) is slightly confusing as it does not agree with how phase is discussed in modern microwave photonics and optical communications (43; 44). In particular, when modern texts refer to phase, they are referring to a relative phase between two sine waves in different portions of the same or different signals, or equivalently the phase of a wave relative to one global origin. As a brief example, microwave photonics may be interested in delaying one optical path by a certain amount to produce a constant phase difference relative to another arm. Steinmetz was the first to introduce and standardize the use of the complex polar coordinate scheme in electrical engineering. In his 1893 publication, he explains that this treatment is well known in other fields, but does not directly reference optics. Regrettably, I cannot find a reliable source on who was the first to use the complex exponential notation in optics due to the unavailability of many old papers, but it should have happened sometime between when the wave nature of light was being advocated by Fresnel in the early 1800s (45), and its integration into standard electrical engineering in the late 1800s (42).

In the complex exponential notation, a fast oscillating carrier wave $exp(i2\pi fz)$ with a frequency f, moves in the normal direction z constructed by the plane (x, y). The wave can be given an initial amplitude $U(x, y)$ depending on the transverse coordinates x and y, to produce

$$u(x, y, z) = U(x, y)e^{i2\pi fz}. \tag{2.23}$$

Then the intensity at any transverse point, or the actually observable part of the wave, would be written as

$$I(x, y) = \left|U(x, y)e^{i2\pi fz}\right|^2 = U(x, y)e^{i2\pi fz} \cdot U^*(x, y)e^{-i2\pi fz} = |U(x, y)|^2 , \tag{2.24}$$

where U^* denotes the complex conjugate. This means that the solution of the differential equation describing the evolution of the electromagnetic wave has been separated into a part which propagates only in the z direction, and another part which is diffusive in the transverse direction. These are essentially the approximations used in Kolner (19) to formulate the space-time duality. This can only be done if the wave is approximately monochromatic and propagating almost entirely in a single direction (paraxial rays). The effect of a thin spatial lens is shown below in Figure 2.13, where the actual lens is enlarged for conceptual clarity. In this diagram, three paraxial rays are highlighted incident on the lens, out of the full spatial image $U(x, y)$. The rays propagate towards the positive z axis with a single frequency f. Using the thin lens approximation, the incident angle on the glass is small, and so each light "ray" will exit at the same transverse coordinates (x, y) as the incidence. This means that for any ray considered, the amount of glass it propagates through is only dependent on its transversal incident point. In particular, for a lens which is radially symmetric on the transverse plane, the amount of glass will depend on the radius to the origin ρ, where $\rho^2 = x^2 + y^2$. Therefore, it is possible to calculate the path length through air and through an amount of glass by using the physical shape of the lens, which is assumed to be quadratic. By the refractive index of light in glass, the speed is slower and the wavelength is shorter. Therefore between the incident and exit planes shown with dotted lines, the path length varies. In the middle of the lens, there is more cycles of the carrier wave in comparison to the edges. The resulting complex wave directly on the other side of the lens can be written generally as

$$u_{out}(x, y, z) = U(x, y)e^{i2\pi fz}e^{i\frac{c}{2}\rho^2} = U(x, y)e^{i2\pi fz+i\frac{c}{2}\rho^2}, \tag{2.25}$$

where c contains information about the physical properties of the lens, including the index of refraction of the material used. Notice however that the intensity profile remains the same under the

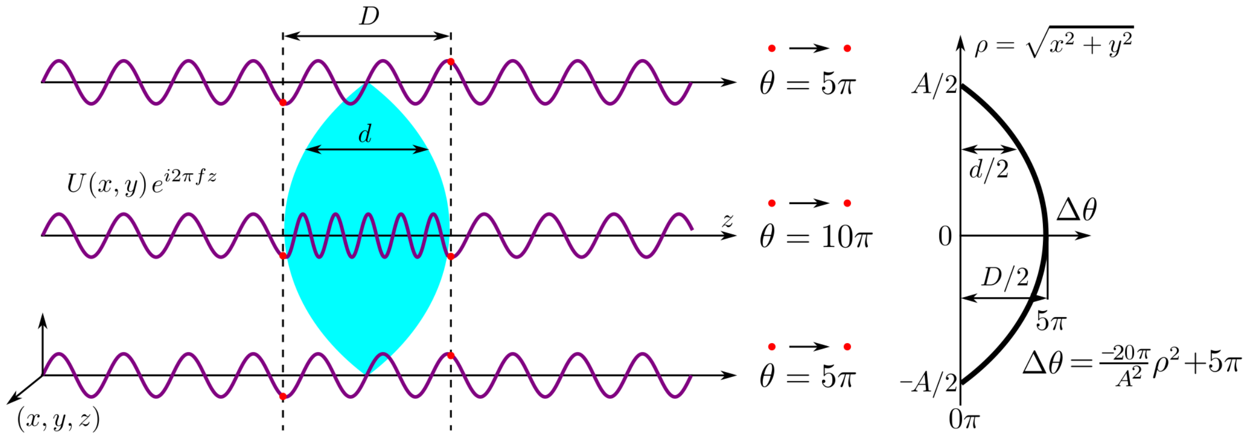

FIGURE 2.13 : Conceptual diagram of a thin spatial lens. Three rays travelling in the z direction are shown entering and exiting the lens at the same transverse point (x, y) that it entered. Due to the refractive index of glass, light travels slower and therefore has shorter wavelengths, as shown for the centre ray. Right before and right after the lens, shown in dotted lines, there is a difference in accumulated phase. The red dots highlight the vertical amplitude of each wave, which may result in, for example, a phase difference of $\Delta\theta = 5\pi$. For a circular lens of aperture size A, one may describe the accumulated phase difference $\Delta\theta$ depending on transverse incident point ρ using the shape of the lens, which is here quadratically convex.

approximations made

$$I_{out}(x,y) = \left|U(x,y)e^{i2\pi fz+i\frac{c}{2}\rho^2}\right|^2 = |U(x,y)|^2 = I_{in}(x,y). \tag{2.26}$$

The spatial lens coupled with diffraction in space is what produces the Fourier transform of $U(x, y)$ at the image plane after a certain propagation distance z. If the intensity is simply a flat function, then the light is focused to a point. Except it is not really a point, it is an airy disk, which is the Fourier transform of a circular aperture, and will become smaller and more point like as the lens becomes infinitely large.

The time lens is this exact principle, but now in the temporal domain. Mirroring the statement of the previous paragraph, a time lens coupled with dispersion is what produces the Fourier transform of an intensity function at the input after a certain propagation distance z.

Taking inspiration from the spatial case, separate the dynamics in terms of a constant velocity (speed of light) propagation in a single direction, and a dispersion of the overall intensity shape of that wave. For a temporal wave there are no transverse directions to the direction of propagation, but it is possible to refer to an intensity shape $U(\tau)$ over a moving time frame τ nonetheless. Consider Figure 2.14, which depicts evolution of an intensity profile through the propagation of some system. By imagining detectors at points z_1, z_2, and z_3, the propagation of the carrier and the diffusion of the intensity profile can be artificially separated. If the detectors all set their recording times to zero when an agreed upon frequency (normally the carrier frequency) would propagate through the system and reach them, then the dispersion of the intensity function can be easily observed and compared at each point throughout the system under consideration. Conceptually this last point means that the choice has been made to follow the intensity profile in a moving time

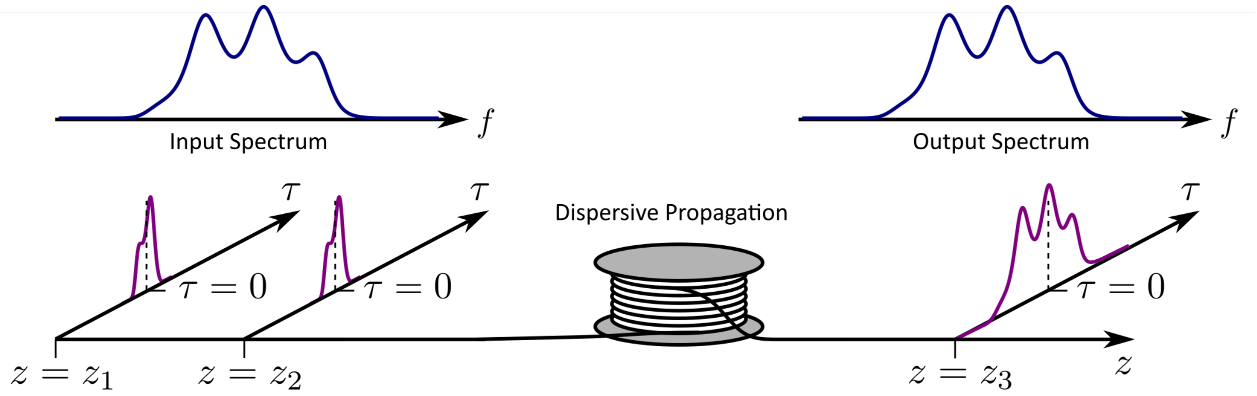

FIGURE 2.14 : Conceptual diagram of a moving time frame specifically to follow the evolution of the intensity envelope and disregard the carrier wave propagation. Detectors placed at points along the z axis of propagation would see certain intensity profiles. Shifting all of their centre times to follow the carrier wave allows for easy analysis of how the intensity profile changes at each point in the system. This system is a conceptual example of a dispersive Fourier transformer, where the spectral information is mapped or copied into the time domain.

frame which is set to the speed of the carrier frequency, sometimes known as retarded time. This is also an extremely useful method computationally, as often simulating the actual carrier wave oscillations is ignored due to the demanding hardware requirements.

The particular situation in Figure 2.14 is that of the dispersive Fourier transformer. This system is particularly useful as an introduction to the frequency-to-time mapping concept, which is essential for the rest of the time lens and TLS developments. In this figure, an initial short pulse has some initial spectrum. It can be shown mathematically that propagating this pulse through a sufficiently long dispersive medium, such as an optical fiber, is analogous to Fresnel diffraction in free space which results in the Fourier transform of the initial input image (with an ignored phase factor) (46). The temporal intensity profile at the output of the system in Figure 2.14 follows the profile of the spectrum at the input, successfully having mapped frequency-to-time. For the dispersive Fourier transformer, the output spectrum is unchanged, as the frequencies do not change in intensity throughout the fiber but simply accumulate a frequency dependent delay, or spectral phase. This is not true for the time lens system to be described. Even though the frequency-to-time mapping still reproduces the spectrum in the time domain at the output, the initial temporal phase modulation will alter the spectrum.

Using ideas from a spatial lens in Figure 2.13, and the moving time frame in Figure 2.14, a scenario is constructed as in Figure 2.15. Consider a fast optical carrier wave has some intensity shape I over time shown in purple dashed lines, and create a moving time frame τ that follows the speed of the optical carrier shown in black. By changing the input voltage into an electro-optic modulator, the optical path length can be varied. If the voltage is changing fast enough, then the path length through the modulator will vary over the course of $I(\tau)$. Consider the wave propagating along the system, three different points of the intensity pattern will have three different times of arrival to the modulator (compare with Figure 2.13 transverse coordinates of incidence). For each time of arrival, there is a certain path length through the modulator which determines how many cycles

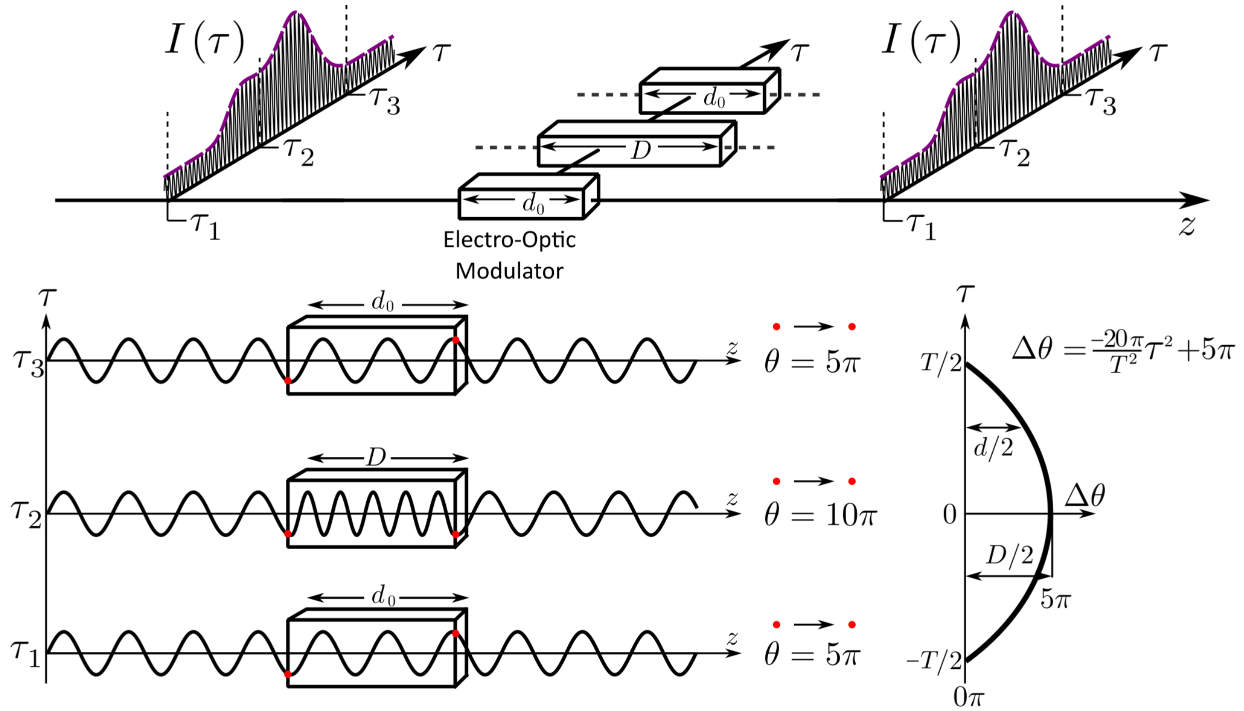

FIGURE 2.15 : Conceptual diagram of a time lens. A fast optical carrier wave shown in black solid lines has some intensity shape I over a moving time frame τ, and in the direction of propagation z. At various points τ_1, τ_2, and τ_3, the intensity pattern sees different optical path lengths (ranging from d_0 to D), and therefore completes different amounts of cycles before exiting the device. This creates a time of arrival dependent phase shift $\Delta\theta$, based on the input voltage in the case of an electro-optic modulator. Compare this figure to 2.13. Here T is the temporal "aperture", or width, of the time lens.

of the wave are needed to traverse the device, equivalent to phase accumulated. The path length is also varied slow enough such that the optical path length remains approximately constant relative to the fast oscillations of the carrier frequency. Therefore, the path length of the device depends on the time of arrival, just as for a spatial lens the path length depends on transverse location of incidence. In Figure 2.15 the variation depicted is quadratic. A time lens mathematically then can be described in the same way as the thin spatial lens, after properly renaming the variables.

$$U_{out}(t) = U_{in}(t)e^{i2\pi ft}e^{i\frac{c}{2}t^2} = U_{in}(t)e^{i2\pi ft + i\frac{c}{2}t^2}, \tag{2.27}$$

where c is some constant describing the properties of the lens, and the variations of the lens are slow in comparison to the oscillations of the optical wave.

There are a number of ways of implementing time lenses, such as electro-optic modulation, four-wave mixing, and cross phase modulation. In the case of electro-optics, a standard approach is to use the sine wave from an RF oscillator to drive the modulator (47; 20). The RF oscillator produces a sine wave as in Figure 2.16 which is matched to, for example, the repetition rate of a pulse train. This sort of time lens can be integrated in all sorts of systems for processing optical time limited events, such as short pulses (20). The optical and electronic waves can also switch roles as in the case of a time lens Fourier transformer (21). In this system, pulses are sent through an

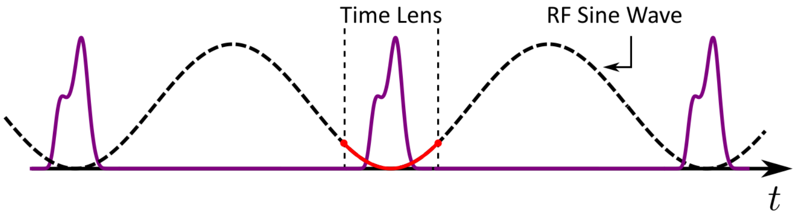

FIGURE 2.16 : Basic diagram of how an RF sinusoid is positioned to relative to a pulse train. Each trough of the sine wave approximates a quadratic function, and therefore can be used as a time lens.

amount of dispersion to acquire a linear chirp (quadratic phase). The optical pulses then become the time lenses and an RF signal can be intensity modulated on top. Notice the signal originates in the RF domain in contrast to the previous case where it originated in the optical domain.

In both cases, a time lens is be coupled with an appropriate amount of dispersion to produce a Fourier transform of a portion of a signal. Part of the interest in adding a time lens to a dispersive Fourier transformer is that the required dispersion can be significantly reduced. Time lens systems and the frequency-to-time mapping concept are extremely useful as once the frequency information of the signal is mapped into the time domain, it can be recovered using simple real-time temporal detection techniques such as photodetectors.

2.6 The Talbot Effect

The Talbot effect is named so after the person who first encountered the phenomenon. Henry Fox Talbot was an English scientist and member of the Royal Society who, while working on early photography, noted an interesting occurrence relating to gratings. In one of his public letters in 1836 he mentions in a few paragraphs an experiment to observe a recurrence of coloured lines from solar light after passing through a grating (48). This is the experiment he described. First, a dark room is prepared with a radiant point of intense solar light. The light is directed horizontally by a mirror for "about ten or twenty feet" towards a grating. The grating is described as "A plate of glass covered with gold-leaf, on which several hundred parallel lines are cut...". Talbot received this grating from none other than Joseph Ritter von Fraunhofer. Following this, a lens is used to refocus the light onto a white sheet. The first observation Talbot made was sharp vertical lines parallel to those of the grating and of varying colours. Originally these were red and green, however after moving the lens away from the grating, blue and yellow, until finally back to red and green. He made a few more interesting experiments with multiple gratings or a copper plate with periodic holes. He routinely demonstrated these images to colleagues but seems to have never formalized his findings. Some of these appearances he described as "...impossible to describe...", ever changing as a kaleidoscope and varying ad infinitum.

To understand why the alternating colours seem to appear at different grating-lens lengths, another important character must be introduced: Nobel laureate John William Strutt, 3rd Baron Rayleigh. Lord Rayleigh was studying photographic copying for optical gratings when he accidentally came across H.F. Talbot's accounts of observations similar to those he had noted during his study. Lord Rayleigh changed his approach after reading these accounts and noted specifically how it would be useful for varying the intervals in photographic copying of his gratings (49). The following is a short account of how he came to find the "revival length" of Talbot's images and how his experiment differed from that of H.F. Talbot. Instead of solar light, Rayleigh used a fish-tail gas-flame masked by a vertical slit as a source. While Talbot specified the use of "...a lens of considerable magnifying power...", 44 years later Rayleigh needed only "...a lens of moderate magnifying power...". Moreover Rayleigh's account is much more precise and is likely the reason he arrived at a quantitative relation. In comparison, Talbot maintained only a seemingly passing interest in the images as a novel demonstration.

The grating chosen was an old coarse grating made by photographing, with a period of 0.0104 inches. The grating was placed at a distance of about 27 feet from the source. While Talbot had predicted a mathematical source would see an infinitely repeating revival of the red/green and blue/yellow pairs, Rayleigh correctly reasoned that this phenomenon would likely dissipate after a certain distance due to the finite size of the grating. He also correctly reasoned that the revival length should be wavelength dependent. He proceeded to record a table for grating-lens lengths for the optimal points of the red and green light separately. He did so using pieces of coloured glass held up to the eye for the purpose of monochromatizing the images. The lens would be moved until either the red or the green were sharp and appeared with the correct period, then the distance from the grating would be recorded. He proceeded from 1.75 inches up until 9 feet while still observing the revivals (after which the revivals began to lose brightness and quality).

During Rayleigh's experiment, he observed that as the distance increased, the proper period was lost and shorter periods could be seen but fluctuations in brightness prevented consistent recording of these. Coincidentally there are positions where the revival length for red and for green are so similar as to be indistinguishable without the aid of the coloured glass. One especially important observation which relied on the use of the coloured glass was that of the "sign" of the image. Rayleigh considered one particular distance of 33.25 inches, an optimal point for green (corresponding to the 7th revival). Near to this distance occurs a good revival for red at 34.5 (corresponding to the 8th revival). When using the green coloured glass a needle point was used to mark the center of a bright band. Switching to the red coloured glass the same needle point instead marked the center of a dark band. His conclusion was that the effect was "...not a mere shadow in any ordinary sense of the term." The revivals alternate light and dark bands at a distance which depends on wavelength. This self imaging effect is shown in Figure 2.17 along a single transverse dimension. In Figure 2.17 (a), the alternating self images are seen by the dark spots changing position slightly every Talbot period. Figure 2.17 (b) shows multiple colours combined in an RGB image, to highlight the frequency dependent nature of the self images. In this figure, the Talbot carpet for only three discrete frequencies are computed. This would apply to any electronic device combining RGB colours to form an image. Natural light, comprised of a broad and continuous spectrum, would have a very different looking carpet.

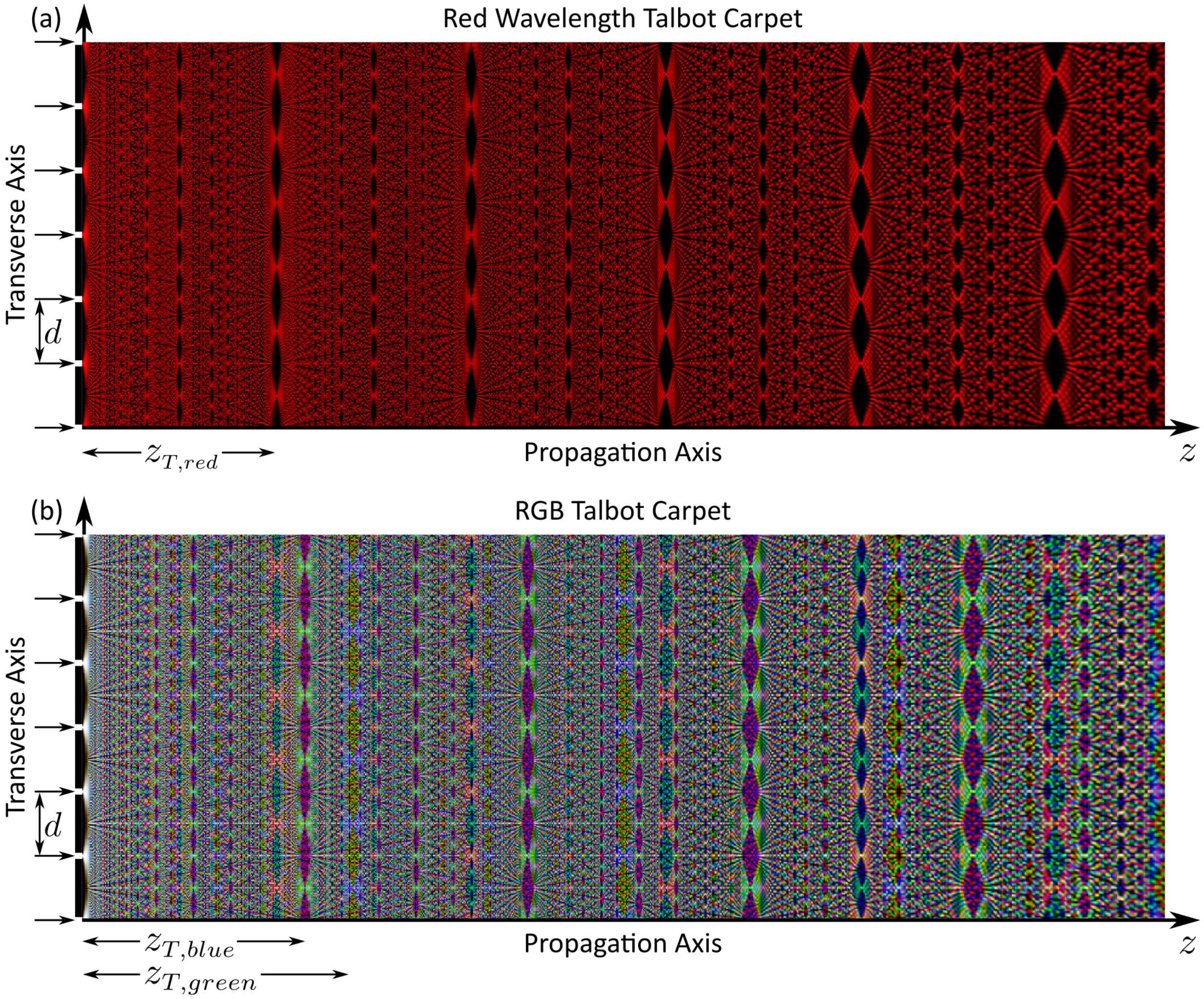

FIGURE 2.17 : (a) Talbot carpet for red light, where the image is initially a set of finite width apertures, and the light propagates to the right in the z direction. The deterioration of the self images comes from the finite number of apertures simulated, along with a finite resolution in both axes. d is the period of the thin slit apertures. (b) A red-green-blue image formed by combining the Talbot carpets for red, green, and blue light. The self images of the transverse axis can be seen to occur at different distances of propagation for each colour, corresponding to different Talbot lengths z_T for each colour.

Lord Rayleigh's theoretical approach to the problem, although more complete than Talbot, is presented somewhat less rigorously than modern treatments (50), and involves quite a few approximations. For a more in depth mathematical discussion on self imaging following Montgomery (51), see the Appendix 7.3. The derivation begins with a general result from vibrations on membranes (52) which he applies then to the field just after the grating to find that the intensity has a term periodic in the z direction given by

$$z_{2T} = \frac{\lambda}{1 - \sqrt{1 - \frac{\lambda^2}{d^2}}}, \tag{2.28}$$

where d is the period of the aperture as in Figure 2.17, λ is the wavelength, and z_{2T} is the Talbot length. Using the binomial approximation, as well as a grating with a period much larger than the wavelength, he finds the following relation,

$$z_{2T} \approx \frac{\lambda}{1-(1-\frac{1}{2}\frac{\lambda^2}{d^2})} = \boxed{\frac{2d^2}{\lambda}}. \tag{2.29}$$

Notice however there is a 2 in the numerator. That is there because in fact the revivals are periodic in twice the grating period squared over the wavelength. As was mentioned before, this accounts for the alternating "sign" of the revival. The Talbot length is defined here as z_T, ignoring the sign of revivals. Using the mean interval between revivals and a corrected grating period, Rayleigh experimentally confirmed his result by calculating wavelengths from equation (2.29). This equation predicted that the red and green light he was using to have had a wavelength of $\lambda_R = 6.4 \times 10^{-5} cm$ and $\lambda_G = 5.59 \times 10^{-5} cm$, respectively. The true wavelengths transmitted by the red and green glasses were found by other means to be $\lambda_R = 6.64 \times 10^{-5} cm$ and $\lambda_G = 5.76 \times 10^{-5} cm$, respectively. At this point Lord Rayleigh's well documented reports and the accessible technology garnered real interest in the effect as more than simply an interesting way to make pretty lines in a Cambridge dark room.

Many more developments have been made with the Talbot effect since its discovery in the 18th century. A.W. Lohmann was a German physicist who worked on holography and time-frequency representations, but also published results relating to the Talbot effect. Lohmann along with J. Jahns published a paper in 1978 proposing a reciprocal experiment to that of Ernst Lau which they called a Talbot interferometer (53), for the usual purposes of an interferometer. In another paper with James A. Thomas, Lohmann described an array illuminator based on the Talbot effect (54). Array illuminators are devices with the goal of splitting incoming light into an array of smaller images or beams (55). This can be done using an array of pinholes, an array of lenses, or phase gratings constructed by a periodic pattern of varying glass thicknesses. This last example inspired the the utilization of the Talbot effect in the design of the phase grating (56; 54).

The design of phase gratings based on the Talbot effect comes from the phase of light at fractional distances to the Talbot length z_T in the Talbot carpet shown in Figure 2.17. In Figure 2.18, the temporal Talbot effect is shown for an initial signal comprised of square shaped pulses. The self images at Talbot lengths are all identical, up to a shift, with the original pulses which are assumed to have zero phase. At a fractional propagation distance to the Talbot length, there is a fractional image formed (57; 58; 59; 60). Propagation in an optical fiber is energy preserving, as energy into a fiber must come out somehow, and for an ideal fiber the only way out is at the other end. This means that the signal energy is conserved, and however the input frequencies have interfered at the output the power must adjust to compensate. In the case shown in Figure 2.18, the fractional image at half the Talbot length is twice the periodicity, and therefore each pulse has half the power to conserve signal energy. Assuming the signal does not have sufficient power to induce any frequency mixing phenomenon, the energy in each frequency at the output is the same as the input. Modifying the temporal shape of the waveform without modifying the energy distribution

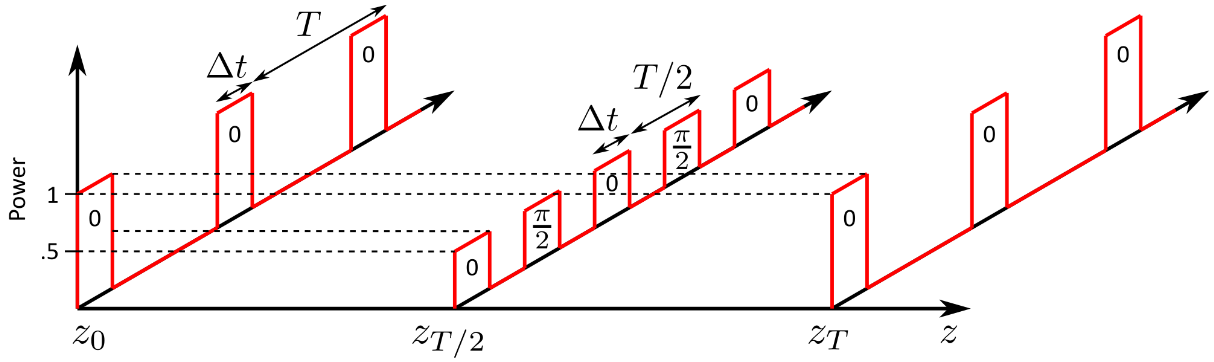

FIGURE 2.18 : An initial signal comprised of square shaped pulses is shown at an initial propagation distance z_0 of a system. After complete propagation through the system to the Talbot length, z_T, the pulses will self image and reconstruct. At an intermediate point $z_{T/2}$, a fractional distance to the Talbot length z_T, there will be a fractional self image. In the example shown, the fractional image reproduced is at half the Talbot length. Therefore, the frequency of the pulses $1/T$ is twice that of the original signal $2/T$, the power is half, while the pulse width Δt and shape remains the same. The phases of the pulses are shown underneath each pulse, assuming zero relative phase between the pulses at the input.

of the frequencies implies that there must be a temporal phase attached to any fractional image. These fractional images have been used as Rayleigh predicted: to easily modify the periodicity during the manufacturing of gratings. They have also been used extensively as a simple way to control the periodicity of optical pulse trains from mode locked lasers(61; 62; 63).

From these fractional images, an array illuminator can be constructed when the width of the square pulses approaches the periodicity of the fractional image. If $\Delta t = T/2$ from the previous example in Figure 2.18, then a situation depicted in Figure 2.19 occurs. Taking the $z_T/2$ propagation point as the input, a phase pattern according to a fractional Talbot image can be put onto a continuous source to produce pulses at the output. The amount of dispersion required as well as the amplification of power are dependent on the specific fractional self image phase used. The particular phase pattern of the fractional image is found by computing Gauss sums (64; 65; 66). For a image at a fractional distance pz_T/q with p and q co-prime, the period of the fractional image will be T/q. The phases of the n^{th} pulse of the fractional image at this distance will be

$$\varphi_{n,p,q} = \pi\frac{s}{q}n^2 \mod 2\pi, \tag{2.30}$$

where s is an integer solving

$$sp = 1 + q\epsilon_q \mod 2q, \tag{2.31}$$

and ϵ_q is the parity of q (equal to zero when q is even and one otherwise). A binary phase grating is simplest ($q = 2$, $p = 1$, and $s = 1$, $\varphi = 0, \pi/2$), but higher numbers of levels are of course possible (67). Higher order phase patterns produce sharper and higher intensity peaks, which can be used to make gratings from white light (54), or amplify arbitrary signals lost under noise (68; 69). For general fractional distances, the propagation in an optical fiber must satisfy

$$2\pi|\beta_2|z = \frac{p}{q}T^2, \tag{2.32}$$

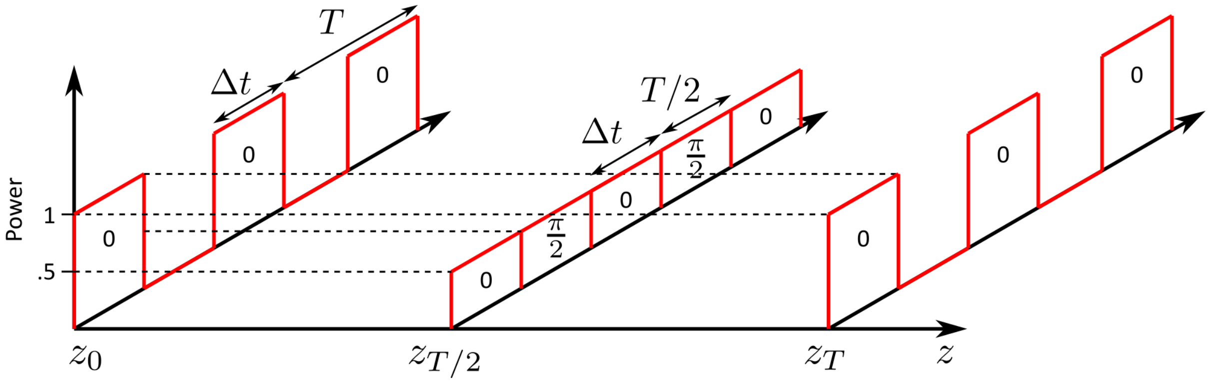

FIGURE 2.19 : An initial signal comprised of square shaped pulses of widths $\Delta t = T/2$ is shown at an initial propagation distance z_0 of a system. At an intermediate point $z_{T/2}$, a fractional distance to the Talbot length z_T, there will be a fractional self image. At the fractional self image, the rectangular pulses meet to form a near continuous signal. Changing perspectives to think of this continuous signal as the input, it is possible to put a phase pattern on a DC signal an produce pulses at the output. This must occur after a propagation distance corresponding to the fractional length of the phase pattern used, in this case $z_T/2$.

where β_2 is the second order dispersion parameter for the fiber, z is the length of the fiber, and T is the periodicity of the integer self image (61).

3 THEORY AND DERIVATION

3.1 The Time Lens Spectrogram

The essential difference between previous Fourier transformers based on the time lens and the TLS is that in the TLS the lenses are placed edge to edge. Note, in this thesis a time lens is defined as the temporal phase modulation, independent from the dispersion required afterward to perform the Fourier transform (see section 2.5). This difference is one of the foundational concepts of this thesis, differentiating it from previous work on the time lens for time limited waveforms or interstitched time lens systems. It requires additional constraints in the derivation of the imaging conditions for the system, which will be outlined in this section.

To perform a gapless spectrogram completely in the analog domain, two phase transformations are implemented on the signal. The first is a consecutive set of time lenses, described in section 2.5, followed by chromatic dispersion. To reiterate certain key points, the concept of a time lens comes from the mathematical duality between spatial paraxial light propagation and narrow-band temporal light propagation (19). Secondly, a time lens coupled with dispersion results in a frequency-to-time mapping of the spectral information into the temporal domain, to be detected by a photodetector. A time lens is any device able to impart a time dependent phase $\varphi(t)$ on a temporal waveform, following a quadratic function over time to mimic the thin lens results of spatial optics. In the following derivation, only the baseband frequency components of the optically modulated signal are considered. All of the waveforms will be multiplied with a fast varying optical carrier wave

$$a_{carrier}(t) = e^{i2\pi f_c t}, \tag{3.1}$$

where f_c is in the hundreds of THz range. Ignoring the optical carrier, the operation of the time lens on the baseband waveform is

$$a_{Lens}(t) = a(t) \cdot e^{i\varphi(t)} = a(t) \cdot e^{i\frac{C_L}{2}t^2}, \tag{3.2}$$

where C_L contains information on the strength of the time lens, and a_{Lens} denotes the waveform after being transformed by the lens. The parameters of the time lens are visualized in Figure 3.1. The time lens has a maximum phase excursion

$$\varphi_{max} = \varphi\left(\frac{T}{2}\right) = \frac{C_L}{8}T^2, \tag{3.3}$$

where T is the temporal width, or aperture, of the time lens. Each time lens provides a bandwidth

$$\Delta\omega = C_L T, \tag{3.4}$$

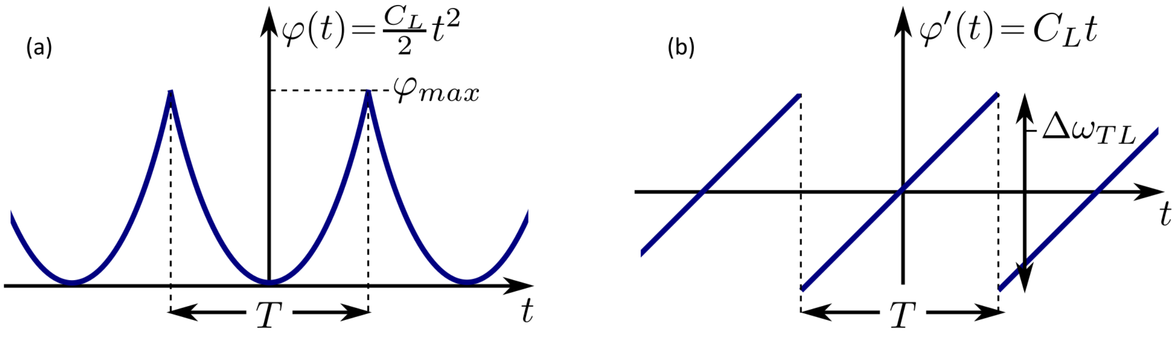

FIGURE 3.1 : Visualisation of edge to edge consecutive time lenses. (a) The phase $\varphi(t)$ of each lens follows a quadratic function over time, with strength C_L. Each time lens has a width T, equivalent to its aperture. (b) Plot of instantaneous frequency $\varphi'(t)$ of the phase. The bandwidth $\Delta\omega_{TL}$ defines the maximum bandwidth of the JTFR to follow.

where $\omega = 2\pi f$ is the angular frequency. This bandwidth will also be confirmed later in this section to be the bandwidth of the JTFR, $\Delta\omega = 2\pi B_w$. The time lenses are shown in Figure 3.2(b), integrated into the TLS system.

The remaining component required to complete the FT in time is an analog to spatial dispersion. For a temporal SUT, chromatic dispersion will produce a quadratic frequency dependent phase modulation

$$A_{FT}(\omega) = A_{Lens}(\omega) \cdot e^{i\frac{\ddot{\phi}}{2}\omega^2}, \tag{3.5}$$

where A_{FT} is the spectrum of the wave after dispersion, and A_{Lens} is the spectrum before dispersion. The symbol $\ddot{\phi}$ stands for the strength of the second order dispersion parameter. In fiber optics it is common to see this multiplied by a length in kms, but for the results in this thesis, only reflection mode chirped fiber Bragg gratings are employed, so $\ddot{\phi}$ is the complete parameter. This transformation is represented in the TLS overview of Figure 3.2 as component (c), coming after the time lens. As discussed in section 2.5, these two transformations have previously been confirmed to produce a Fourier transform in the time domain (47; 21; 20). The previous work involving time lenses has only focused on time limited or periodic waveforms. This is because, as for a spatial FT imaging system, the temporal FT imaging system results in a frequency-to-time mapped spectrum which is much longer in the time domain than the original waveform (21). This means that if lenses (quadratic functions) are placed too closely together, the resulting images will be corrupted by complex interference patterns that are not analyzable without prior knowledge of the SUT. As Figure 3.2 qualitatively shows, if the lenses are indeed to be placed edge to edge, then each Fourier transform must be mapped to a time of equal size (T). The lenses must be placed edge to edge for analysis of continuous signals, otherwise portions falling in between lenses, and potentially crucial pieces of information, are necessarily discarded.

The consecutive placement of the time lenses in the TLS contrasts the usual method by which troughs of a sinusoid are used to approximate quadratic functions (47). The proper conditions to allow this placement are presented in (17). Assuming a rectangular aperture as defined in 2.16 for

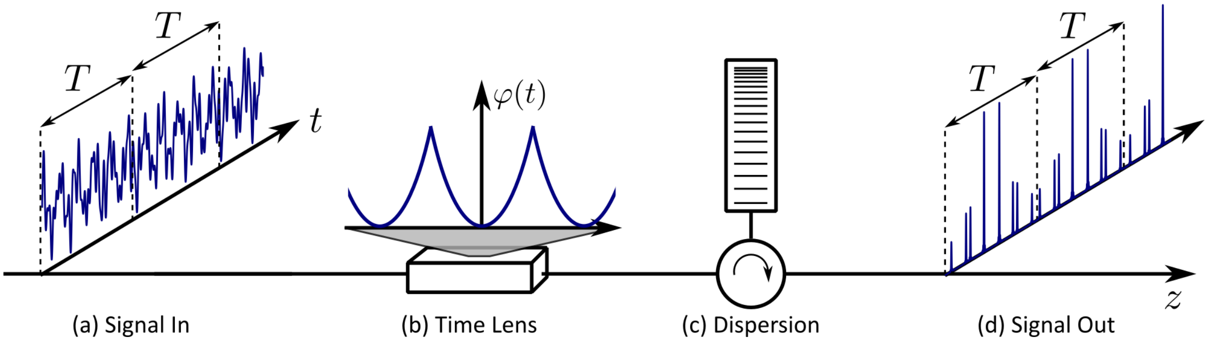

FIGURE 3.2 : Conceptual overview of the TLS. (a) An input temporal signal, already prepared in the optical domain. (b) The time lens stage consisting of edge to edge quadratic phase functions (lenses). (c) Chromatic dispersion, or equivalently, a frequency dependent delay. (d) Output consecutive Fourier transforms mapped into the time domain. The output spectra should not overlap and therefore must be contained within a time T; the width of the lens aperture/window.

each time lens of width T, the complete lens array is written as,

$$L(t) = \sum_{n=-\infty}^{\infty} R\left(\frac{t-nT}{T}\right) e^{i\frac{C_L}{2}(t-nT)^2}. \tag{3.6}$$

It is useful to introduce a shifted time $t' = t - nT$. Multiplying this lens array by the input signal $a(t)$ results in the following equation:

$$a_{Lens}[n,t') = a[n,t')e^{i\frac{C_L}{2}(t')^2}, \tag{3.7}$$

where $a[n,t')$ denotes the n^{th} segment of $a(t)$ windowed by a rectangular function of width T and shifted to the zero time. Since each of these are non-overlapping, each windowed segment can be treated individually. Imposing a chromatic dispersion is equivalent to applying a phase in the spectral domain over angular frequency and so

$$\mathcal{F}\left\{e^{i\frac{\ddot{\phi}}{2}\omega^2}\right\} = \frac{1}{\sqrt{i2\pi\ddot{\phi}}}e^{i\frac{1}{2\ddot{\phi}}(t')^2}. \tag{3.8}$$

Therefore, the output wave in the temporal domain after both transform can be found by the definition of the convolution

$$a_{out}[n,t') = a_{Lens}[n,t') * \frac{1}{\sqrt{i2\pi\ddot{\phi}}}e^{i\frac{1}{2\ddot{\phi}}(t')^2}. \tag{3.9}$$

$$a_{out}[n,t') = \frac{1}{\sqrt{i2\pi\ddot{\phi}}}\int_{-\infty}^{\infty} a_{Lens}[n,\tau)\cdot e^{i\frac{1}{2\ddot{\phi}}(t'-\tau)^2}d\tau, \tag{3.10}$$

where τ is a dummy variable which will be integrated out to produce a function over t'. After rearranging the exponential phases,

$$a_{out}[n,t') = \frac{e^{i\frac{(t')^2}{2\ddot{\phi}}}}{\sqrt{i2\pi\ddot{\phi}}} \int_{-\infty}^{\infty} a[n,\tau) \cdot e^{i\left(\frac{C_L}{2}-\frac{1}{2\ddot{\phi}}\right)\tau^2} \cdot e^{i\frac{t'\tau}{\ddot{\phi}}} d\tau. \tag{3.11}$$

The next step is to set the time mapped frequency to be $\omega = 2\pi f = -t'/\ddot{\phi}$. The negative sign is included to arrive at a standard form in the following step, and it simply means the frequency axes are reversed in comparison to increasing time. In analogy with the spatial system, define a mapping or magnification factor $M = 2\pi|\ddot{\phi}|$, as well as the imaging condition $C_L\ddot{\phi} \approx 1$ in order to neglect the second phase term,

$$a_{out}[n,-fM) = \frac{e^{i\pi Mf^2}}{\sqrt{iM}} \int_{-\infty}^{\infty} a[n,\tau) \cdot e^{i2\pi f\tau} d\tau. \tag{3.12}$$

This output waveform is easily recognizable as the Fourier transform 2.13 of the input segment $a[n,t)$, multiplied by some frequency dependent phase. The rewritten equation

$$a_{out}[n,-fM) = \frac{e^{i\pi Mf^2}}{\sqrt{iM}} \mathcal{F}\{a[n,\tau)\} \tag{3.13}$$

can be recognized as the n^{th} component of the STFT from section 2.4 (see also Appendix 7.2). By taking the square magnitude, retrieve the n^{th} spectrogram component of the signal, multiplied by a constant (magnification factor),

$$|a_{out}[n,-fM)|^2 = \left|\frac{e^{i\pi Mf^2}}{\sqrt{iM}} STFT[n,f)\right|^2 = \frac{1}{M} SPGM[n,f). \tag{3.14}$$

Then it has been shown that the spectrogram is mapped directly into the time domain according to the frequency-to-time mapping factor $f = t'/(\ddot{\phi}2\pi)$. It remains to position each of the segments as the vertical slices of a two dimensional image over time to produce a spectrogram image as in Figure 3.3.

Finally, to ensure that there is not interference between the n^{th} transformed spectra and the $n \pm 1$ segments, impose the following condition.

$$|a_{out}[n,-fM)|^2 = 0, \qquad \text{for all} \qquad |fM| \geq T/2, \tag{3.15}$$

where the above condition on the frequency of the SUT implies the system has a maximum analysis bandwidth of $B_w = T/|M|$, and that the SUT must have a bandwidth equal to or less than this. Here the notation for analysis bandwidth is defined as twice the maximum frequency $B_w = 2f_{max}$ from

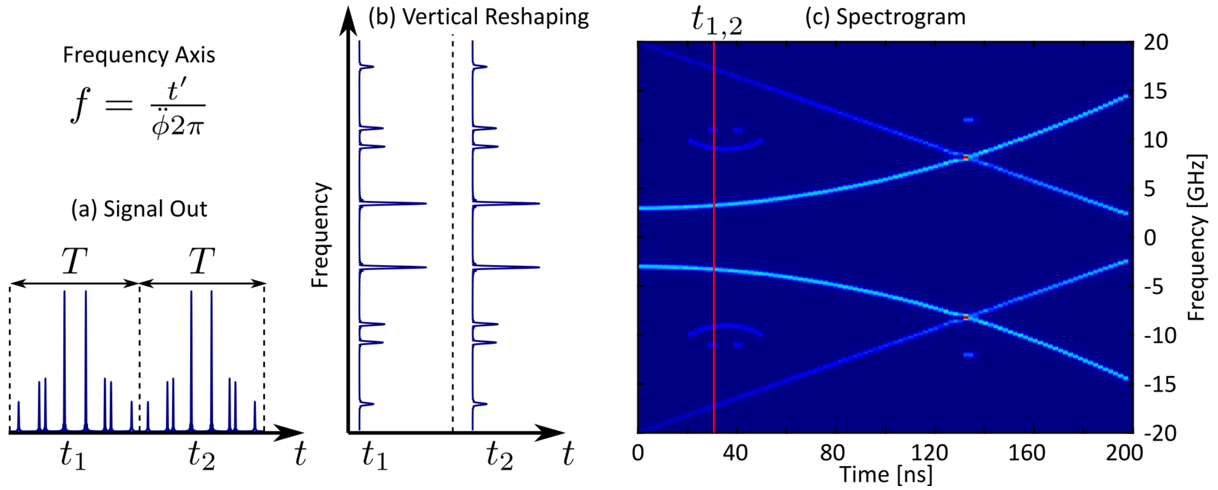

FIGURE 3.3 : Conceptual process of taking consecutively frequency-to-time mapped spectra and reshaping them to produce a spectrogram image. (a) Output time-mapped spectra from the TLS. (b) Place each spectra vertically alongside one another, over their time of arrival. Define the frequency axis using the frequency-to-time mapping factor. (c) Set the intensity as colour and plot all together. The red line on the spectrogram plot indicates the final location of the spectral slices shown in (a) and (b).

the inequality in 3.15. Notice also that

$$B_w = \frac{T}{|M|} = \frac{T}{2\pi\ddot{\phi}} = \frac{C_L T}{2\pi} = \Delta\omega_{TL}, \tag{3.16}$$

the bandwidth of the time lens. Using this result, define the number of analysis points per spectrum as the analysis bandwidth divided by the frequency resolution,

$$\eta_{TLS} = \frac{B_w}{\delta f} = \frac{T^2}{2\pi|\ddot{\phi}|}. \tag{3.17}$$

This can be rearranged further to depend on what has been experimentally one of the most challenging hardware requirements. For the TLS, this is the maximum phase excursion φ_{max} of each time lens, defined as the phase at the edge of each quadratic function of width T,

$$\varphi_{max} = \frac{C_L}{8} T^2. \tag{3.18}$$

Therefore, the maximum number of analysis points is dependent solely on this design parameter,

$$\eta_{TLS} = \frac{4}{\pi}\varphi_{max}. \tag{3.19}$$

Equations 3.18 and 3.19, along with the imaging condition $C_L\ddot{\phi} = 1$, will be used in the derivation of the following section.

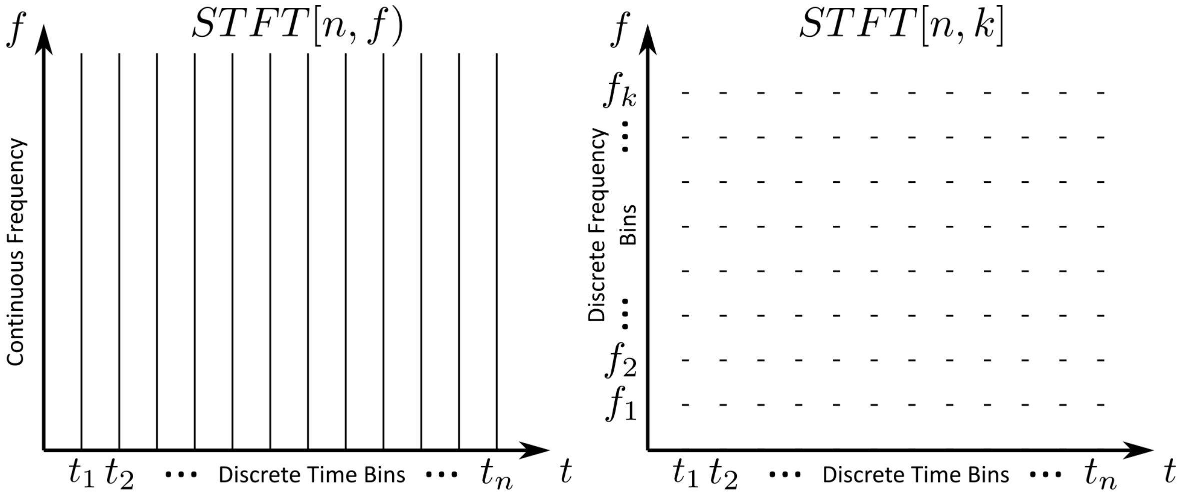

FIGURE 3.4 : The STFT is partially discrete due to the windowing of the time lenses. Each time lens has no overlap and so the frequencies occurring during one time window are independent of the ones outside that window. While the TLS is mapped into the analog time domain, the consecutive spectra remain continuous functions. A sampling or digitization of the output spectra will induce a discrete frequency axis. The derivation in this section uses this process to motivate the TAI phase pattern in the original phase modulation.

3.2 Talbot Array Illuminator Spectrogram

In this section, a theoretical connection between the TLS and the TAIS will be made. The program proposed is to discretize the spectrogram resulting from the TLS, and work backwards to find the required phase modulation at the input. The concept of this discretization is shown in Figure 3.4. As a brief motivation, the TAIS will solve a key issue of the TLS that arises in practice; that is, the maximum phase excursion. It does this by wrapping the phase to 2π, similar to a Fresnel lens. A key difference however is that a Fresnel lens requires high bandwidth near the edges of the lens, while the TAIS uses relatively constant bandwidth over the entirety of the lens. Further discussions on the motivation and trade-offs of the TAIS in comparison to the TLS are left to section 3.3, while Fresnel lenses are discussed in section 6.2 as future work.

On the output time mapped spectrogram from the TLS 3.14, take η samples of each segment. This divides the bandwidth into even frequency steps $\Delta f = B_w/\eta$, and the frequency at the k^{th} sample of the spectrum is $f_k = k\Delta f$. Recalling the definition of the analysis bandwidth, $B_w = T/|M|$, the temporal period at which the time-mapped waveform is sampled is $t_k = -f_k M = -k\Delta f M = -kT/\eta$. By the sifting property of the Dirac delta, this k$^{\text{th}}$ sample can be recovered in the following way

$$a_{out}[n, -f_k M] = \int_{-\infty}^{\infty} a_{out}[n, -fM]\delta(f - f_k)df. \tag{3.20}$$

The first term is related to 7.23, the discretized STFT for time index n and frequency index k by

$$a_{out}[n, -f_k M] = \frac{e^{i\pi M f_k^2}}{\sqrt{iM}} STFT[n, k]. \tag{3.21}$$

Now after having linked the discrete time-mapped spectrogram to the discrete STFT, it is time to explore the effects of this discretization. Substitute 3.9 into 3.20 to get

$$a_{out}[n, t_k) = a_{out}[n, k] = \frac{1}{M} \int_{-\infty}^{\infty} \left(a_{Lens}[n, t') * \frac{1}{\sqrt{iM}} e^{-i\frac{\pi}{M}(t')^2} \right) \delta(t' - t_k) dt'. \tag{3.22}$$

The following step is motivated in this way: since the Dirac delta is symmetric, and since the convolution is well defined even for generalized functions, sampling the result of a convolution can be shown to be identical to sampling one of them before convolution,

$$a_{out}[n, k] = \frac{1}{M} \left(\int_{-\infty}^{\infty} a_{Lens}[n, t') \delta(t' - t_k) dt' \right) * \left(\frac{1}{\sqrt{iM}} e^{-i\frac{\pi}{M}(t')^2} \right). \tag{3.23}$$

This is an approximation, which leads to the rest of the results below. For a complete understanding of when this procedure is valid, a more rigorous definition of the convolution for generalized functions must be called upon (70; 71; 72). I expect that this step is also likely the reason for the restriction of the results to even number of levels in the multilevel phase pattern. Focusing now just on the first term before dispersion results in the lens function sampled at discrete points,

$$a_{Lens}[n, k] = \frac{1}{M} \int_{-\infty}^{\infty} a_{Lens}[n, t') \delta(t' - t_k) dt'. \tag{3.24}$$

Using 3.7, the definition of the waveform after the lens results in

$$a_{Lens}[n, k] = \frac{1}{M} a[n, t_k) \cdot e^{i\frac{C_L}{2}(t_k)^2}, \tag{3.25}$$

with a resulting phase,

$$\varphi[k] = \frac{C_L}{2} \left(\frac{kB_w}{M\eta} \right)^2. \tag{3.26}$$

First, substitute for the analysis bandwidth $B_w = T/M$. Then, use 3.18, the definition of the maximum phase excursion from the previous section on the TLS to get

$$\varphi[k] = 4\frac{\varphi_{max}}{\eta^2} k^2. \tag{3.27}$$

Recall the number of analysis points of the TLS system is given by 3.19. Choose $\eta = \eta_{TLS}$ to give the same number of analysis points as the TLS, then the final discretized phase is

$$\varphi[k] = \pi \frac{1}{\eta} k^2. \tag{3.28}$$

This temporal phase modulation follows a discrete quadratic phase in the same form as the TAI (18; 61; 65; 73). An example of the discretization process is shown in Figure 3.5. This phase function may be wrapped to 2π as in 3.5(b) and still give an equivalent modulation. In practice these phase steps are generated as a multi-level phase pattern, with each phase constant over a temporal width Δt. To complete the analogy, it remains to present the required dispersion in a

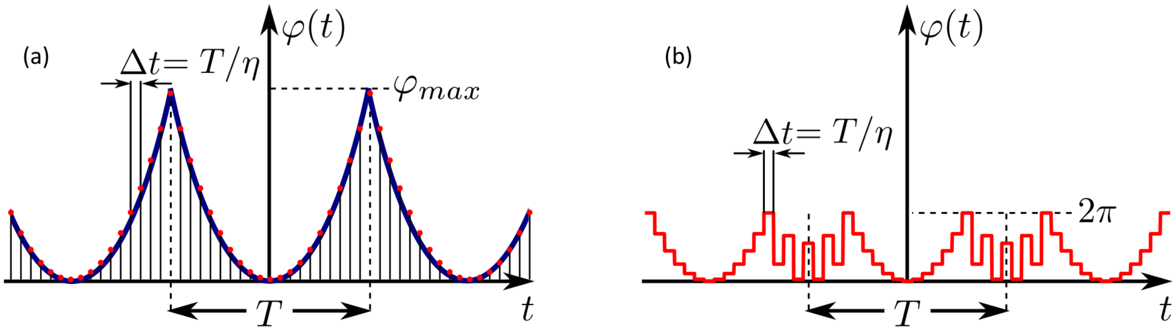

FIGURE 3.5 : (a) Quadratic time lens functions shown in a blue solid line. The phase function is discretized at even segments of time $\Delta t = T/\eta$ shown by vertical lines, where η is the pattern length. The sampled phase at each discretized point is shown with red dots. (b) The discretized phase can be wrapped to 2π, and the multilevel phase pattern with this wrapping is shown with a solid red line.

familiar form. From the TLS imaging condition, the maximum phase relation, and the resolution of the TLS,

$$\ddot{\phi} = \frac{1}{C_L} = \frac{T^2}{2\pi\eta}. \tag{3.29}$$

Using the sampling period of the discretization $\Delta t = T/\eta$,

$$\ddot{\phi} = \frac{\Delta t^2 \eta}{2\pi}, \tag{3.30}$$

which is the dispersion condition for the TAIS (18). Continue to find the maximum analysis bandwidth in terms of the new variable Δt. Consider B_w/η, and use the preceding definitions to find

$$\frac{B_w}{\eta} = \frac{T}{|M|\eta} = \frac{T}{2\pi\ddot{\phi}}\frac{\pi}{4\varphi_{max}} = \frac{T}{2\pi\ddot{\phi}}\frac{2\pi}{C_L T^2} = \frac{1}{T}. \tag{3.31}$$

Multiply both sides by η to get

$$B_w = \frac{\eta}{T} = \frac{1}{\Delta t}. \tag{3.32}$$

Equation 3.32 describes the maximum bandwidth of the TAIS, which is dependent just on the temporal sampling period Δt. A simple rearrangement will show the TAIS retains the same number of analysis points, frequency resolution, and time resolution as the TLS. Furthermore, all of these agree with what was derived by Azaña (18) for even pattern length. The TLS and TAIS are not, however, redundant. The physical realisability of each the TLS and TAIS are not the same. The difference between the limiting considerations for implementing each will result in complementary, overlapping, but not identical use cases and target applications. This discussion will be the topic of the next section.

3.3 Comparison and Trade-offs

The TLS and the TAIS are theoretically equivalent up to discretization, but their complementary implementation using the same setup enables a particularly interesting degree of flexibility. Comparison of the design equations for the TLS and the TAIS is shown in Table 3.1, and these parameters are illustrated in Figure 1.1. Since electro-optics is commercially available, packaged, and easy to implement, electro-optics is employed to perform the temporal phase modulation and use an arbitrary waveform generator (AWG) to generate the modulation function. The commercially available devices which Prof. Azaña's group has can accommodate a modulation function of up to around 7π phase excursion over 40 GHz bandwidth. Alternatives in nonlinear optics could be considered which provide significantly higher phase excursions above 100π (74), but this would significantly increase the complexity of the system. Chirped fiber Bragg gratings are used for the dispersive propagation, which have the advantage of providing hundreds of kilometers of equivalent single mode fiber dispersive propagation in a small footprint over the entire optical C-band. For the following discussion, comparing the TLS to the TAIS, it will be assumed that the experiment is done using modern available technologies with the approximate performances above.

From 3.19, it has already been seen how a higher number of analysis points η for the TLS is limited by the maximum phase excursion φ_{max}. For electro-optics, this value is around 7π, which results in around a maximum of 28 analysis points using 3.19. The maximum phase excursion of electro-optic modulation could be circumvented by wrapping the TLS phase to 2π to implement a Fresnel lens, but the edges would demand more and more bandwidth to be generated properly (32), and consequently a faster AWG.

The TAIS is the discretization of the TLS but sampled at regular intervals Δt and so the bandwidth requirement is distributed more evenly throughout the entire phase modulation function. This means overall the TAIS can provide a manipulation equivalent to a time lens, but with the potential for a significantly larger maximum phase excursion, as well as longer temporal analysis window width T. In turn, this results in a spectrogram with significantly more analysis points per spectra and therefore higher frequency resolutions (see the third row, third column of Table 3.1). What limits this temporal analysis window width, however, is the dispersion $\ddot{\phi}$ required to satisfy the imaging conditions as shown in Table 3.1. To reduce the required dispersion, one can decrease the width of the phase steps Δt, but only to the maximum allowable by the bandwidth of the phase modulator and AWG. Thus, based on the chosen devices and using Table 3.1, the TAIS allows for analysis bandwidths of around 100 GHz, with frequency resolutions near 100 MHz, and approaching 1000 analysis points per spectra.

On the other hand, parabolic phases can be generated with just a few samples from the AWG. This contrasts the high number of phase levels required by the TAIS multilevel phase function. Thus, from a generation perspective, the TLS allows for much smaller time resolution and analysis window T down to around 60 ps, in comparison to the TAIS, due to the smaller minimum number of

Parameter	Symbol	TLS	TAIS	Optimal Implementation
Time Resolution	δt	T	$T = \Delta t\, \eta$	TLS
Frequency Resolution	δf	$\frac{1}{T} = \frac{T}{8\varphi_{max}\lvert\ddot{\phi}\rvert}$	$\frac{1}{T} = \frac{\Delta t}{2\pi\lvert\ddot{\phi}\rvert}$	TAIS
Analysis Bandwidth	B_w	$\frac{T}{2\pi\lvert\ddot{\phi}\rvert} = \frac{4\varphi_{max}}{\pi T}$	$\frac{T}{2\pi\lvert\ddot{\phi}\rvert} = \frac{1}{\Delta t}$	TLS
Analysis Points	η	$\frac{4}{\pi}\varphi_{max}$	$\frac{T}{\Delta t} = \frac{2\pi\lvert\ddot{\phi}\rvert}{\Delta t^2}$	TAIS

TABLE 3.1 : Comparison of design equations for the TLS and the TAIS for relevant parameters named in the first column. The symbol used for the parameter throughout the paper is shown in the second column. The equations chosen in the second and third column relate to the most difficult hardware consideration for the TLS and the TAIS, respectively. In the final column, the optimal spectrogram is chosen to implement the best value for each parameter considered.

points required to adequately generate the phase modulation function. Increasing the sample rate of the AWG would always be useful, as both smaller time and TAI lenses could be generated with better precision. Furthermore, the strength of the lens C_L scales linearly with the maximum phase but quadratically with the size of the analysis window, thus allowing the TLS to reach higher analysis bandwidths since this is not limited by the speed of the modulation generation scheme. Of course the bandwidth of the modulation scheme still comes into play with the number of samples per second achievable to make such a small analysis window, but that bandwidth does not correspond to the resulting analysis bandwidth. Therefore, if only small amounts of dispersion are available, or maximal bandwidth is desired, it is more appropriate to use the TLS. Thus, the TLS can achieve over 400 GHz analysis bandwidths, with over 25 analysis points per spectra. A list of the optimal choices for each desired system performance is summarized in the last column of Table 3.1.

3.4 Predicted Nonidealities

There is an additional assumption which has been implicit in all the previous discussions. Once the spectra are mapped into the time domain by the frequency-to-time mapping of either the TLS or the TAIS, the detector and ADC must have sufficient bandwidth to properly recover and digtize the output waveform. For real-time applications, this typically implies the use of a high-speed radio-frequency oscilloscope, which has $\approx$ 100 GHz of acquisition bandwidth when considering state-of-the-art performance (75). Each of these spectrograms have spectra with η analysis points over an output temporal duration of T. Therefore, recovering the waveform with more samples than η per spectrum will result in no new information about the spectrogram. Accordingly, for ideal detection, it is required to employ a scheme providing a sample period equal to

$$\frac{T}{\eta} = \frac{1}{B_w}. \tag{3.33}$$

In other words, the detection bandwidth must be equal to the analysis bandwidth of the spectrogram, and by extension the SUT bandwidth, for ideal recovery of the spectrograms. What about when this condition is not satisfied? As shown by the experimental results of sections 5.2 and 5.3, employing a detector with lower bandwidth than required will result in a degraded number of analysis points per spectrum. This is caused by a broader response time of the detector, smudging the frequency resolution by an amount

$$\delta f_{det} = \left(\frac{B_w}{B_{det}}\right)\delta f, \tag{3.34}$$

where δf_{det} is the degraded frequency resolution, B_{det} is the bandwidth of the detection scheme, and $\delta f = 1/T$ is the ideal frequency resolution. However, the total analysis bandwidth of the spectrogram will be unaffected. This super-bandwidth detection (when $B_{det} < B_w$) is allowed and does not violate any Nyquist sampling rules since it is not in fact the original SUT that is being detected, but the SUT's local frequency spectrum mapped along the time domain. The information along the time axis is now (time varying) frequency information. Under-sampling this time mapped frequency information affects the frequency resolution, not the time resolution. In fact, the time resolution of the JTFR is still a large multiple of the detection sample period. This result means that since the processing is done optically, it is possible to analyse signals whose bandwidths far exceed the detection and digitization bandwidths. While this super-bandwidth recovery is a feature of both spectrograms, the TAIS will easily outperform the TLS, until hardware or clever techniques allow for much higher phase modulations. Recall the TAIS can provide an extremely high number of analysis points, meaning more analysis points can be sacrificed while still recovering the JTFR with reasonable clarity.

Finally, it should be noted that as with all optical signal process strategies, the electro-optic conversion of the SUT assuredly leads to partial deterioration of the signal. Optimizing the modulation conditions to ensure best performance is not trivial (76) and is affected by multiple components including the RF amplifier, the chosen intensity modulator, and the optical carrier. For the results presented here, a MZM style IM is used with a voltage bias to produce an optical signal with as little a DC component as possible. This implies that arms of the MZM are out of phase from one another by π radians, and the MZM is operated in the linear regime. A full study on the impact of nonidealities in the electro-optic conversion stage to the TLS and TAIS is important but is left as future work.

4 EXPERIMENT

4.1 Set-up

The experimental demonstration consists of an SUT generation stage in Fig 4.1(a), an optical time-mapped spectrogram processing stage in Figure 4.1(b), and a detection and recovery stage shown in Figure 4.1(c).

The microwave SUT is generated using an arbitrary waveform generator (AWG) with a sampling rate of 92 GSa/s and amplified by a radio frequency amplifier (RFA). An output from the AWG is sent to a 28 GHz real-time oscilloscope (RTO) to trigger the sampling of the RTO at the same place in the signal every time. This is convenient for visualizing the signal using the RTO before data collection. As soon as data is collected, one copy of the desired signal is recovered and triggering becomes unnecessary. To analyse free space microwave signals, it would be possible to first capture by a receiving antenna and then proceed in the same way as the rest of the demonstration shown here.

The optical spectrogram stage consists of a continuous wave (CW) laser set to 1550 nm with a linewidth below 0.1 kHz connected to a 40 GHz electro-optic IM which receives the electrical SUT for up-conversion to the optical domain. The TLS and TAIS temporal phase modulation functions are generated by the same 92 GSa/s AWG that generated the SUT, making use of the best possible equipment available rather than for any requirement of synchronicity. The electrical temporal phase modulation signals are amplified by an RFA before driving an electro-optic phase modulator (PM). For the TLS, an RFA with a saturated power of 33 dB with 32 GHz bandwidth is used, while for the TAIS, a 50 GHz bandwidth RFA with 23 dB of saturated power. To maximize the possible phase excursion in the TLS case, a 30 GHz phase modulator with a V_π =2.6 V is used, and a 40 GHz phase modulator with V_π =3.1 V for the TAIS. The modulators are biased at the half wave voltages, to diminish the DC contribution. The optical SUT passes through the PM and proceeds to a linearly chirped fiber Bragg grating (CFBG) introducing a second-order dispersion of $\ddot{\phi} \approx$ 2,508 ps^2 for the TLS and $\ddot{\phi} \approx$ 15,415 ps^2 for the TAIS. The lower dispersion grating operates over the full optical C-band (>5 THz bandwidth), while the larger dispersion grating has a smaller bandwidth of around 650 GHz.

For near-optimal recovery of the time-mapped spectrograms, a 50 GHz photodiode (PD) is used to transfer the processed signal from the optical back to the electrical domain, and a 28 GHz real-time oscilloscope (RTO) to go from the electrical to the digital domain. To analyse the effects of limited detection bandwidth on the resulting spectrogram, two situations are tested with intentionally reduced bandwidth. The first is limiting the detection bandwidth of the RTO in the device programming. The second is using a 6 GHz bandwidth PD for the optical to electronic conversion.

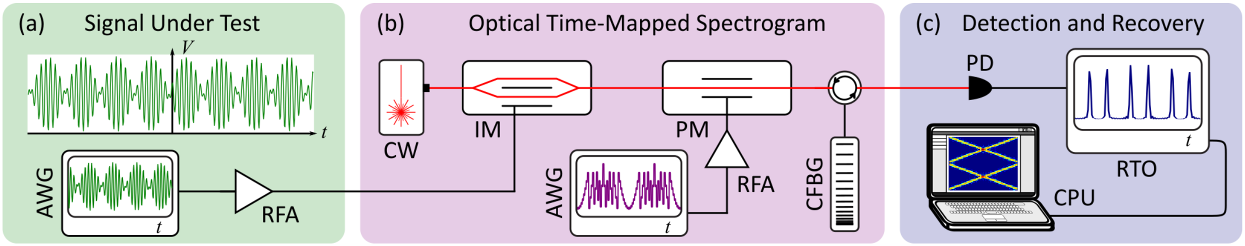

FIGURE 4.1 : Experimental setup for the test of the two photonics spectrograms, both the TLS and the TAIS. The SUT stage generates the electrical microwave signal. The optical time-mapped spectrogram stage up-converts the microwave signal into the optical domain, and then either the TLS or the TAIS phase modulation along with chromatic dispersion results in consecutively time-mapped Fourier transforms. The detection and recovery stage consists of a square-law intensity photodiode, for conversion of the optical waveform to the electrical domain, and analog to digital conversion by a real-time oscilloscope. The computer reshapes the time-mapped spectrogram into a 2D image to be visualized.

To evaluate the performance of the TLS and TAIS to recover the proper global spectra of the SUTs, the spectrogram data is projected onto the frequency axis and normalized, and then compared with an optical spectrum analyser (OSA) trace. An OSA is used instead of an RF spectrum analyser or the fast Fourier transform (FFT) of the electrical SUT to isolate the spectral responses of the TLS and TAIS from the expected aberrations resulting from the nonideal electro-optic up conversion. Nevertheless, the frequency calibration discussed in the results section is also confirmed with the FFT of the electrical SUT, and the roll-off of the electro-optic conversion stage can be seen by comparing the various spectra in Figure 5.1.

4.2 Temporal Phase Modulations

Three different spectrogram systems will be tested with three different design settings. These design settings are summarized in Table 4.1, and Table 4.2 computes the expected parameters using the equations from Table 3.1. A reminder of the interpretation of some of these parameters is shown in the modulation plots of Figure 4.2. The first is the TLS with time lens aperture T = 696 ps, dispersion parameter of $\ddot{\phi} \approx$ 2,508 ps^2, and phase excursion of φ_{max} =7.68π, allowing for a theoretical analysis bandwidth of B_w = 44.1 GHz with $\eta \approx$ 31 number of analysis points. The second is the TAIS with η = 206 phase levels, Δt = 1/(46 GHz) = 21.7 ps level period, dispersion parameter of $\ddot{\phi} \approx$ 15,415 ps^2, and aperture size of T = 4.48 ns, allowing for B_w = 46 GHz. The final spectrogram setting is a higher bandwidth TAIS with η = 824 phase levels, Δt = 1/(92 GHz) = 11.0 ps level period, dispersion parameter of $\ddot{\phi} \approx$ 15,415 ps^2, and aperture size of T = 8.96 ns, giving B_w = 92 GHz. The theoretical phase modulation inputs into the AWG are shown in black dotted lines in Figure 4.2(a) and 4.2(b) for the TLS and the TAIS with η = 206, respectively. In the case of the TLS, there is a large pre-compensation for distortions caused by amplification, resulting in an asymmetric lens. Shown in red solid lines are the phase functions generated by the AWG and recovered directly from the RTO. Comparing the shapes of the two phase functions does not reveal any significant distortions by the AWG.

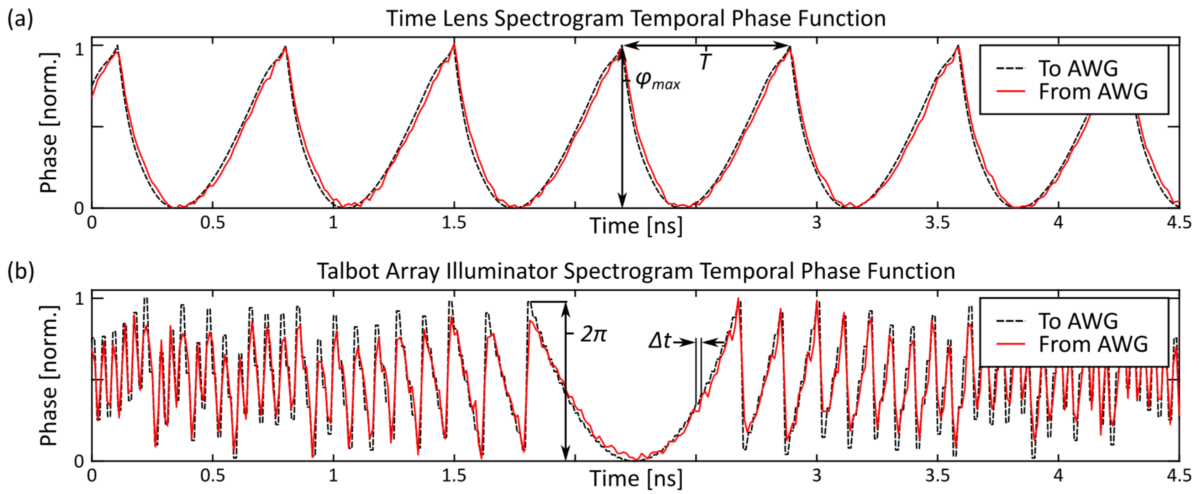

FIGURE 4.2 : (a) The theoretical time lens phase sent to the AWG shown in black dotted lines is compared to the generated signal from the AWG shown in red. Each quadratic function is skewed to compensate for distortion by the RF amplifier. (b) Theoretical and experimental TAI phases, where over the 4.5 ns only one pattern can be seen, representing one T. The function is wrapped to 2π and each discrete phase level has a width of Δt.

Experimental Design	Symbol	TLS	TAIS	HB TAIS	Units
Time Lens Aperture/Pattern length	T	0.696	4.48	8.96	ns
Number of Phase Levels	η	-	206	824	-
Equivalent Maximum Phase Excursion	φ_{max}	7.68π	51.5π	206π	rad.
Dispersion	$\ddot{\phi}$	2,508	15,415	15,415	ps^2

TABLE 4.1 : Comparison of experimental design parameters for three experimental cases: the TLS, the TAIS, and the high-bandwidth (HB) TAIS. The parameter name is in the first column, while the symbol used to represent it is in the second column.

Parameter	Symbol	TLS	TAIS	HB TAIS	Units
Time Resolution	δt	0.696	4.48	8.96	ns
Frequency Resolution	δf	1.44	0.223	0.112	GHz
Theoretical Analysis Bandwidth	B_w	44.1	46.0	92.0	GHz
Theoretical Analysis Points	η	31	206	824	-

TABLE 4.2 : Resulting experimental characteristics based on the experimental design parameters found in table 4.1. The values are calculated based on the formulas found in table 3.1 (note $\Delta t = T/\eta$). The three columns TLS, TAIS, and HB TAIS are the three design specifications tested in the main part of the results.

4.3 Presentation Details

Some important details about how the results are presented are discussed in this section, particularly the reshaping of the time mapped spectrograms into a 2D image as well as the specific normalization used.

In general, the lens apertures (in the case of the TLS), or the pattern lengths (in the case of the TAIS) are not integer multiples of the sampling period of whatever digitization method is used (in this case a RTO). Therefore, each output spectrum of the time mapped spectrogram may have variable number of samples. This is a slight problem for visualization, as in the case that the number analysis or sample points per spectrum is low, then the centre frequency will be seen to visually shift up and down on the frequency axis based on the fraction of the sample point remaining in each spectrum. This is not an issue if the sample rate is chosen to be a multiple of the Fourier transform rate, but for this experiment that was not the case. To solve this an array was created with column length equal to the maximum of the discrete samples per spectrum. Data is then filled into this array, starting at the first sample point falling within the theoretical time extent of the lens. In this way artifacts on the very remaining row of the spectrogram are created, which may or may not be duplicates of the proceeding column, first row. I chose this method as it does the best job at centering every spectrum as well as possible over any amount of time, rather than reshaping the array with fixed dimensions and having the resulting spectrogram necessarily "tilt upwards or downwards" after a certain amount of time, ruining the frequency axis.

The resulting spectrogram image is then normalized in the following way. The mean and standard deviation of a sufficiently large section of the time mapped signal are taken. The mean of this noise is subtracted and the result is divided by the standard deviation, so that the final spectrogram is in intensity units of the standard deviation of the noise. Any signal below 1 in this vertical scale is within the standard deviation of noise, and so not likely to be properly recovered. All signals shown have good clarity in this scale, because the effect of noise was not a primary target of investigation in these results. However, it is expected that since phase manipulations are in theory energy preserving, that each of the methods described (TLS and TAIS) would amplify the peak intensity of a continuous signal in direct relation with the analysis points of each spectrum, minus the system losses.

4.4 Phase Strength and Pattern Length

For the TLS, a first essential calibration involves the strength of the lens. Theoretically, the maximum phase excursion should be $\varphi_{max} = 7.68\pi$ for the first experimental test. The electro-optic phase modulator provides an optical phase shift based on the input electrical voltage. This electrical voltage is directly from an amplifier with frequency dependent gain on the signal from the arbitrary waveform generator. Therefore it is necessary to adjust the amplifier or AWG signal strengths to obtain the proper phase modulation strength at the phase modulator. A continuous wave optical signal with no microwave intensity modulation (i.e., DC signal) is input into the TLS system and the output is observed with an RTO while the strength of the AWG is varied.

5 RESULTS

5.1 Frequency Calibration

A frequency calibration is done using a single constant tone at 15 GHz to confirm the expected frequency-to-time mapping law. This will in effect ensure the actual or experimental bandwidth is near to the theoretical, or to correct it if there is meaningful error. The same 5.35 μs SUT is given to both the TLS and the TAIS, while a slightly shorter 4.49 μs signal is given to the high bandwidth TAIS due to granularity requirements of the AWG. The spectrograms are shown in Figure 5.1(a), 5.1(b), and 5.1(c) for the TLS, TAIS, and high bandwidth TAIS, respectively. The spectra of the optically modulated SUTs recovered from the OSA and the FFT of the electrical SUTs are compared to the projections of the spectrograms onto the frequency axis (frequency marginals). Before calibration, each of the frequency axes are off by a certain amount, due to ignorance of the effective pattern strength within the phase modulator, as well as the effective dispersion of the chirped fiber Bragg gratings, resulting in an incorrect B_w. From the theory and design conditions, we expect bandwidths of $B_w =$ 44.1 GHz, 46.0 GHz, and 92.0 GHz, for the TLS, TAIS, and high bandwidth TAIS, respectively. Since the lens functions and SUTs are generated using different outputs of the same AWG (not a necessary condition), doubts about the true frequency of the 15 GHz tone would lead to doubts about the time lens apertures (i.e. time resolutions) as well. However, since the spectrum of the optically modulated SUTs and the FFT of the electrical SUTs indicate tones of 15 GHz down to their respective resolutions, we have confidence in the size of the time lenses for the TLS and TAIS and thus, the temporal resolutions. The recovered spectrograms clearly display the expected two straight lines (in this case, vertical lines) of a double-sided spectrogram for a single frequency tone. By scaling the frequency axis of the spectrograms to set these lines at the 15 GHz they are known to be, the experimentally measured bandwidth for each of the spectrograms is found. For the TLS, the experimental bandwidth is $EB_w =$ 42.3 GHz, which is 4.2% off from the theoretical value. The first TAIS setting measurement results in $EB_w =$ 46.0 GHz and 0.22% difference, and the high bandwidth TAIS setting measurement results in $EB_w =$ 92.1 GHz and 0.21% difference. The mismatch of the theoretical and experimental characteristics of the TLS are due to the initial estimation of the dispersion and phase modulation strength, which are difficult to directly measure without approximations. In contrast, the bandwidth of the TAIS is determined by the sample rate of the phase levels, which is set with high precision by the AWG. The peaks of the vertical line features for the two TAIS settings is a discrete estimation due to the sampling of the RTO, with the 15 GHz point happening to fall somewhere between two analysis points of the projection. Therefore, it is reasonable to keep the theoretical bandwidth, which is backed by the AWG timing. This analysis shows that calibration is an important step to compensate for experimental unknowns, but also that the devices and theoretical relations function reasonably well. The most striking variation among the spectrograms displayed is the width in the frequency dimension of the

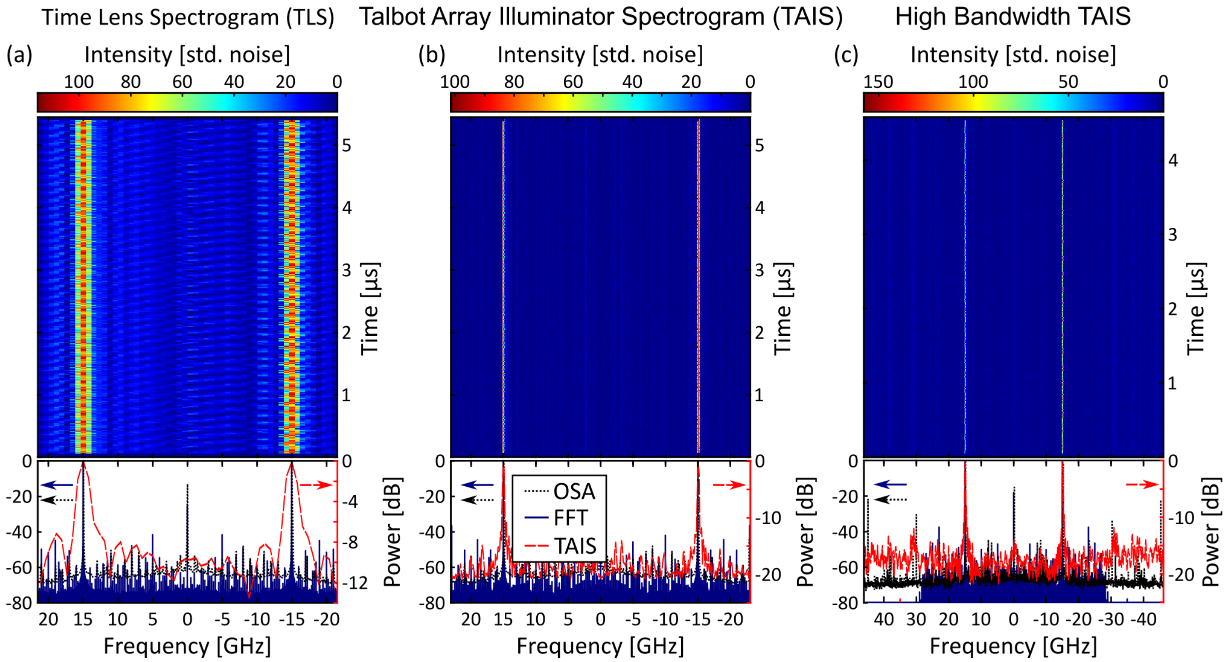

FIGURE 5.1 : Spectrograms of a single 15 GHz tone SUT for the TLS, the TAIS, and the higher bandwidth TAIS. Each optical SUT spectra from an OSA (black dotted line) is compared to the frequency projection of each spectrogram (red) and the FFT of the electrical SUT (blue solid line). Before frequency axis correction, the red spectral traces are slightly different from the more accurate OSA and electrical FFT traces. The frequency axis is corrected so that the frequency projection of the spectrograms give spectra which line up with the OSA and FFT traces of the signal.

vertical lines. This difference in frequency resolution is caused by the various temporal window sizes, according to the uncertainty principle.

5.2 Frequency Resolution

The proceeding SUT is designed to confirm the expected frequency resolution of the TLS and the TAIS. The high bandwidth TAIS will be treated in section 5.3. Considering a signal containing two frequencies at all times, the natural question arises of when would those two frequencies become too close to be discriminated in the spectrogram representation. To answer this question, a SUT is generated consisting of two linear chirps, sufficiently slow (5.35 μs) such that the frequency changes happen over long periods of time relative to the time resolution of the spectrograms. This gives more data points near the frequency resolution limit as the two chirps cross one another. The chirps' lowest frequency is 0.5 GHz and their highest is 21 GHz. The positive side of the spectrograms are shown in Figure 5.2 as well as a zoomed in section of the crossing point in the middle of the SUT. Each zoomed inset includes purple lines around the two chirps, which represent the theoretical frequency resolution of the specific method given by the uncertainty principle. The purple lines are created by first using the same equations as those to generate the SUT, then by splitting each chirp into two lines separated from one another by the expected theoretical frequency resolution. The zoomed sections of each figure thus confirm both the theoretical frequency resolutions

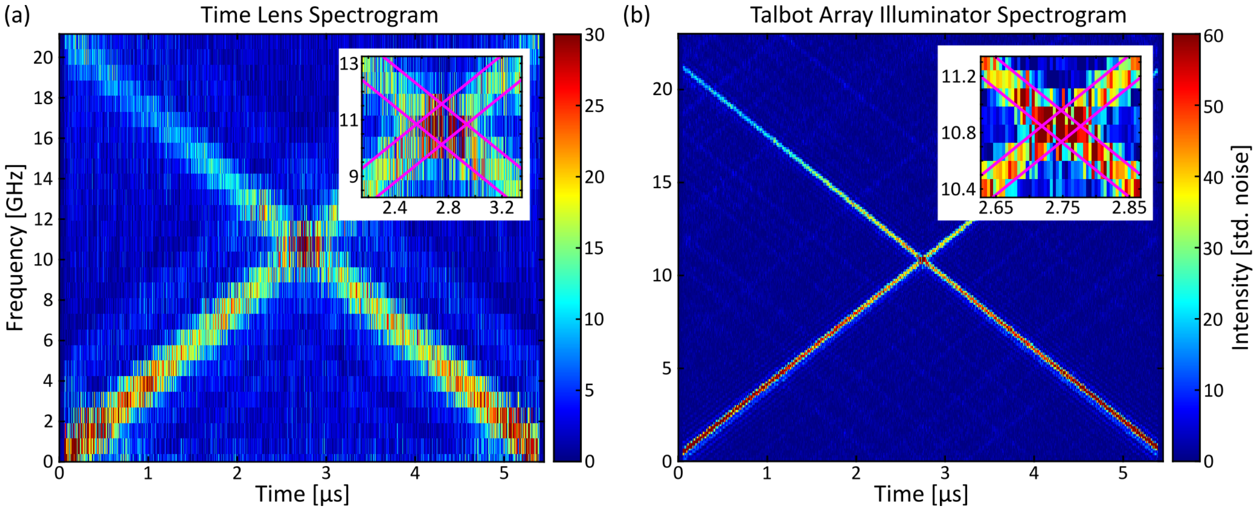

FIGURE 5.2 : Evaluation of the frequency resolution using the same double crossing chirp signal from 0.5 GHz to 21 GHz over 5.35 μs. (a) The TLS is chosen to have a time resolution of 696 ps and a dispersion of $\ddot{\phi} \approx$ 2,508 ps^2. These settings result in an experimental bandwidth of 21.2 GHz, a frequency resolution of 1.44 GHz, and 30 analysis points. (b) The TAIS is chosen to have a phase level period of 21.7 ps and with $\eta = 206$ analysis points, resulting in a time window duration of 4.48 ns. These settings result in an experimental bandwidth of 23.0 GHz, and a theoretical frequency resolution of 223 MHz. For both spectrograms, the theoretical frequency resolutions are shown as purple lines in the insets around the frequency chirps.

as well as the frequency calibrations from the previous section. For the TLS with a 6.96 ns time lens aperture, the frequency resolution is 1.44 GHz. For the TAIS with a pattern period of 4.48 ns the frequency resolution is 223 MHz. The zoomed section shown for the TAIS is one fifth the size of the TLS since the TAIS provides a much higher frequency resolution. The experimental pulse widths of the spectrograms show good agreement with the theoretical frequency resolution lines in purple, confirming that the simple inverse of the time resolution is a reasonable definition of the frequency resolution.

5.3 Degradation of Frequency Resolution

For the high bandwidth TAIS, it will be shown in this section that the available RTO is not fast enough to reach the theoretical frequency resolution. A similar signal is prepared as in section 5.2, two crossing linear chirps from 0.5 GHz to 46 GHz over a time duration of 4.49 μs. The inverse of the pattern length for this version of the TAIS (8.96 ns) gives a theoretical frequency resolution of 112 MHz. Recalling the discussion on analysis points in section 3.3, the total calibrated bandwidth along with this frequency resolution give an expected number of 824 analysis points per spectrum of the spectrogram. The detection method is most constrained by the RTO, which has an impulse response given by an $\approx$ 12.5 ps full-width at half maximum Gaussian pulse, which implies a sampling rate of 80 GSa/s. Therefore, the RTO can provide only 716 samples per spectrum (i.e., analysis points within a 8.96 ns long time window), rather than the full theoretical 824. Using the full bandwidth of the spectrogram, this number of analysis points corresponds to a degraded frequency resolution of 129 MHz. The 15% difference is likely not so visually noticeable in the spectrogram of Figure 5.3(a), nor in the zoomed inset of the crossing point.

This degradation of frequency resolution can be further evaluated by limiting the two devices involved in the detection of the time-mapped spectrogram. The high bandwidth TAIS for the same signal, while digitally limiting the RTO acquisition bandwidth to a 6-GHz acquisition bandwidth is shown in Figure 5.3(b). This is also compared with a physical detection limitation by using a 6 GHz bandwidth photodiode in Figure 5.3(c). Following eq. 3.34, the theoretically expected degraded frequency resolution for a limited detection frequency of 6 GHz is about 856 MHz. Figure 5.3(d), 5.3(e), and 5.3(f) show zoomed-in plots around the crossing point for the best possible detection, oscilloscope bandwidth limited, and using a slow photodetector, respectively. The purple lines show the theoretically expected degraded frequency resolution, showing good agreement with the experimental widths. Finally, Figure 5.3(g) compares a single output spectrum near the frequency resolution limit for detection limited to 6 GHz. The vertical slice chosen is when the two frequency chirps are spaced apart by approximately twice the degraded frequency resolution of 856 GHz. Included in this subplot are the purple lines with the same widths and frequency locations as in the zoomed spectrogram plots. The asymmetrical frequency artifacts seen are hypothesized to be caused by the temporal response of the slow photodetector. In summary, the results presented in Figure 5.3 support the derivations for the degradation of frequency resolution. Additionally, these figures demonstrate that lowering the detection bandwidth decreases the frequency resolution without affecting the total analysis bandwidth. I have shown recovery of a SUT with a 92 GHz full analysis bandwidth, using only a 6 GHz photodiode with up to ≈ 27 analysis points per spectrum. Therefore, the optically time-mapped spectrogram methods are able to recover the spectrograms of signals with much higher bandwidths than the devices used for detection.

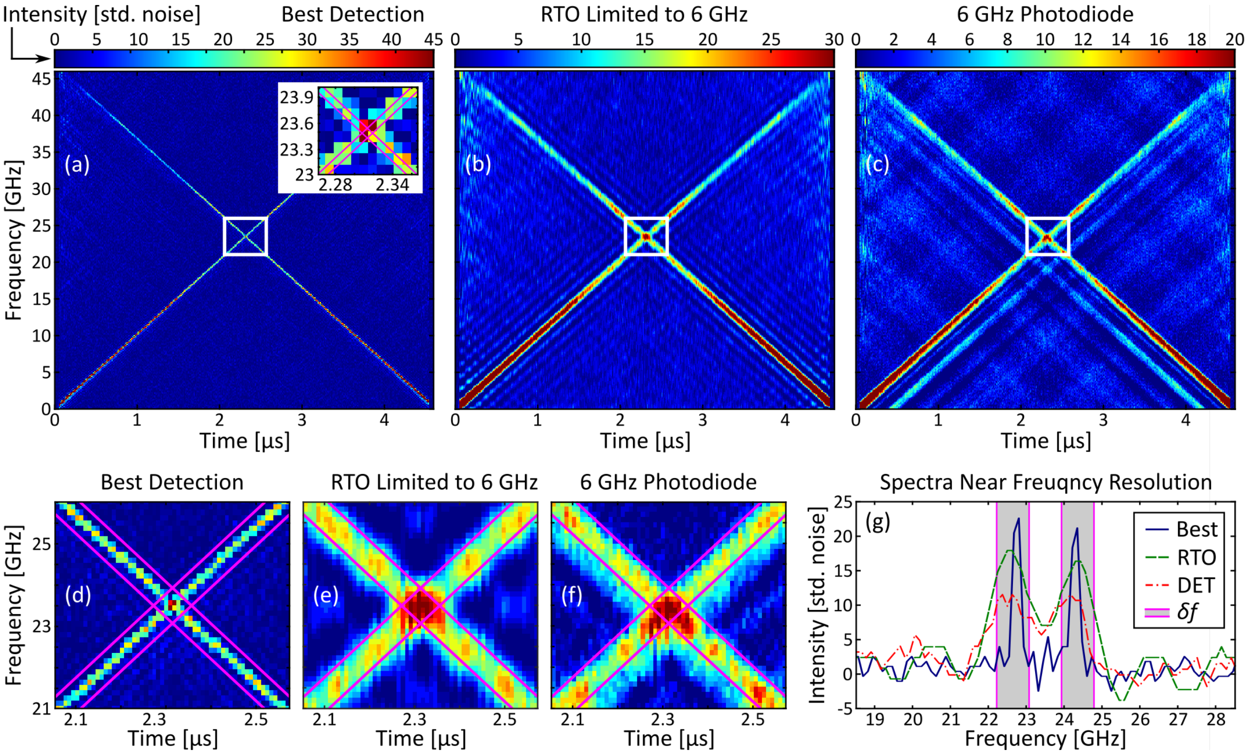

Figure 5.3 : Spectrograms from the high bandwidth TAIS for a crossing chirp signal. The results for the best possible detection are compared to two means of limiting the bandwidth of the detection devices. The purple lines of plots (e), (f), and (g) show the expected frequency degradation from a 6 GHz detection limit.

5.4 Digital vs Photonics Spectrograms

The next results compare two methods of recovering the spectrogram of an SUT with slowly increasing frequency. The first method is the 46 GHz full bandwidth TAIS and subsequent digitization by the fast 50 GHz PD and 28 GHz RTO. The second is the usual scheme involving an analog to digital conversion (ADC) of the electrical SUT from the AWG by the PD and RTO, and then digitally computing the STFT (necessarily offline to match the performance of the TAIS). The SUT consists of a single chirp with a frequency varying from 0.5 GHz to 21 GHz, over a duration of 5.35 μs. The two methods are compared while the bandwidth of detection is methodically lowered below that of the SUT, from 28 GHz, down to 6 GHz. Attempting to recover a SUT with a much larger bandwidth than the ADC (RTO) will highlight the unique ability of the TLS and TAIS to still faithfully recover the spectrogram of these signals.

The optical time-mapped spectrogram of the TAIS is shown above the offline STFT of the electrical signal in Figure 5.4. As the bandwidth of the oscilloscope is lowered, it is expected that the Nyquist sampling criterion will not be satisfied for the higher frequencies of the SUT, and therefore, that the STFT spectrograms will fail at these frequencies. The first row of spectrograms, displaying the TAIS, conclusively demonstrates that lowering the detection bandwidth only affects the frequency resolution, not the bandwidth, as shown in the previous section. This deterioration of the frequency resolution is seen as a broadening of the single chirp in the frequency direction. In the second row, the offline STFT displays a clear bandwidth cutoff at the expected frequency. To the right of the spectrograms is the spectrum of the SUT after optical modulation, taken with an OSA, compared to the frequency projection of the TAIS at the 6 GHz RTO limit. The offline STFT in the case of the 6 GHz RTO limit is compared to the offline FFT of the entire electronic SUT. The OSA displays a frequency roll off towards the higher bandwidths as expected by the effect of nonideal electro-optic up conversion, while the frequency projection of the TAIS with a 6-GHz digitization bandwidth results in slightly more roll off.

It is important to note that the TAIS still recovers the full bandwidth of the signal with a slight roll off and could be compensated for by characterization of the frequency responses of the conversion stages in a later investigation. Regular electronic detection however, results in an immediate cutoff and an unrecoverable spectra beyond a certain frequency, with no potential for compensation. To reiterate, since the TAIS provides such a large number of analysis points per spectrum, using lower bandwidth detection devices can be afforded, as the deteriorated frequency resolution will still result in an acceptably resolved spectrogram (≈ 27 analysis points per spectrum, after deterioration using a 6 GHz bandwidth limit). The same is true in principle for the TLS. However, due to the hardware limitations on the strength of the time lens from electro-optic phase modulation, only a lower number of analysis points are available from the beginning. Therefore, not much frequency resolution can be sacrificed to lower the needed detection bandwidth.

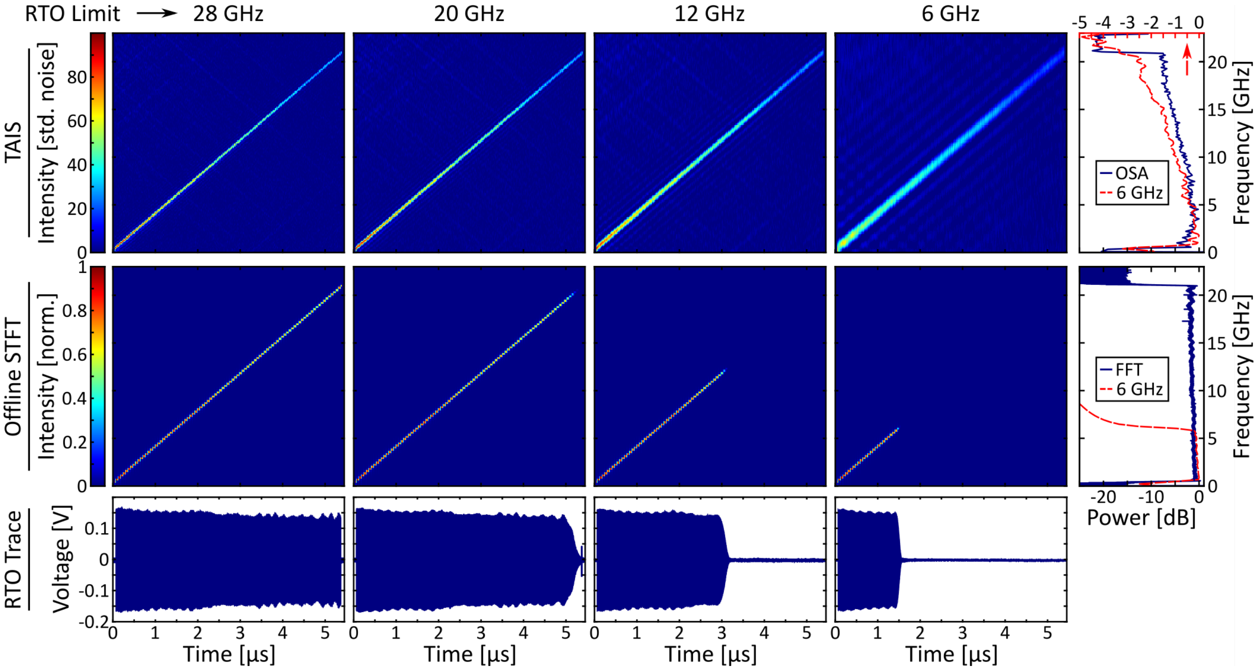

FIGURE 5.4 : TAIS compared to the offline STFT (not real time) of the electronic SUT. The STFT is chosen to have the same temporal window as the TAIS, and due to processing speed limitations, this DSP approach is necessarily done offline after the SUT is digitized and saved by the RTO. The expected bandwidth cutoff from sub-Nyquist sampling of the electronic STFT is confirmed but is not present in the TAIS, which shows recovery of the complete bandwidth even with a limited RTO bandwidth. The spectrum on the right of the TAIS compares the OSA trace to the projection of the TAIS onto the frequency axis for the 6 GHz limited case, showing a quicker roll-off but otherwise still correctly identifying the frequencies present. The spectrum to the right of the offline STFT compares the fast Fourier transform (FFT) of the electrical signal to be generated by the AWG (before the AWG), with the FFT of the electrical signal directly from the AWG digitized by the RTO when it is limited to 6 GHz bandwidth. Between these three spectra can be seen the deterioration from the electro-optic up-conversion stage (electrical FFT to OSA) and the deterioration from the 6-GHz TAIS recovery (OSA to 6-GHz frequency projection). Below the spectrograms, the frequency cutoff can be seen in the temporal trace of the electrical signal when the frequency becomes too high to be properly sampled with the corresponding bandwidth.

5.5 Ultrashort Transient Recovery

Where the TLS excels, is in providing extremely high temporal resolution, as well as high analysis bandwidth (77). The following experiment demonstrates sub-nanosecond time resolution without gaps in acquisition. A signal is prepared consisting of ultrashort transient events at 15 GHz. Each event is repeated 32 times, being shifted slightly by 1/32 the time of $T = 696$ ps, with sufficient spacing in between to treat each event individually. From this time resolution there should be approximately 10 cycles of the 15 GHz signal per time lens. The series of 32 events is repeated 9 times corresponding to different durations of the event, with the shortest event lasting 0.125$\cdot T$, and the others from 0.25$\cdot T$ to 2.25$\cdot T$ in steps of 0.25$\cdot T$. The electronic SUT is shown for the event duration of 1$\cdot T$ in Figure 5.5(a). The synchronicity of two different events with their time lenses is shown in Figure 5.5(b), 5.5(c). In Figure 5.5(b), the event falls within a single analysis window and thus is imaged by a single lens, producing a single Fourier transform in the "earlier" time lens, see Figure 5.5(d). In Figure 5.5(c), the event is divided among two different time lenses, falling on the edge between the two. In this case the energy of the event will be mapped to two spectra, corresponding to the “earlier” and “later” time lens, as shown in Figure 5.5(e), and so it is expected that the peaks of each spectra will be roughly half that of the case in Figure 5.5(d). Figure 5.5(f) displays the time mapped spectrogram of the TLS during the section with the event duration of $1{\cdot}T$, depicting the aligned and misaligned case shown above. Figure 5.5(h) shows the spectrogram recovered from the TLS of the SUT, with the temporal projection above it in Figure 5.5(g) in the dark blue trace, right vertical axis. Here, the peak value of the intensity of the pulses found in the earlier time lens are depicted in green, and that of the later time lens in red. Evidently, it can be seen that the energy of the event is transferred from the early lens to the later one as the event is scanned. In Figure 5.5(i) the electrical signal is taken from the AWG and an offline STFT with the same characteristics as the TLS confirms the expected spectrogram features. Summing the values of the spectrogram in a time-frequency area of size $3{\cdot}\delta f{\times}3{\cdot}T$ around the expected location of each event, then dividing by the summation of an empty region of noise, returns a measure of how much energy was captured by the TLS in the expected region. If the analysis is truly gapless, it is expected that there is a weak dependence of temporal shift on this measure. Figure 5.5(j) displays this measure for all durations and all shifts, showing low dependence on synchronicity. In Figure 5.5(k), the energy is divided by the duration of the event in units of T, to give a measure that does not depend on input synchronicity. In the ideal case, it is expected that this matrix be of a single color, meaning all input energy is mapped into the expected time-frequency region. The results indicate that as the event duration goes below the time resolution of the system, the effect of the imperfect time lens edges becomes non-negligible. This effect is more important if the majority of the event falls on this distorted edge. These results show that transient events of duration down to the time resolution of the spectrogram are accurately recovered, regardless of their synchronicity, without gaps in acquisition.

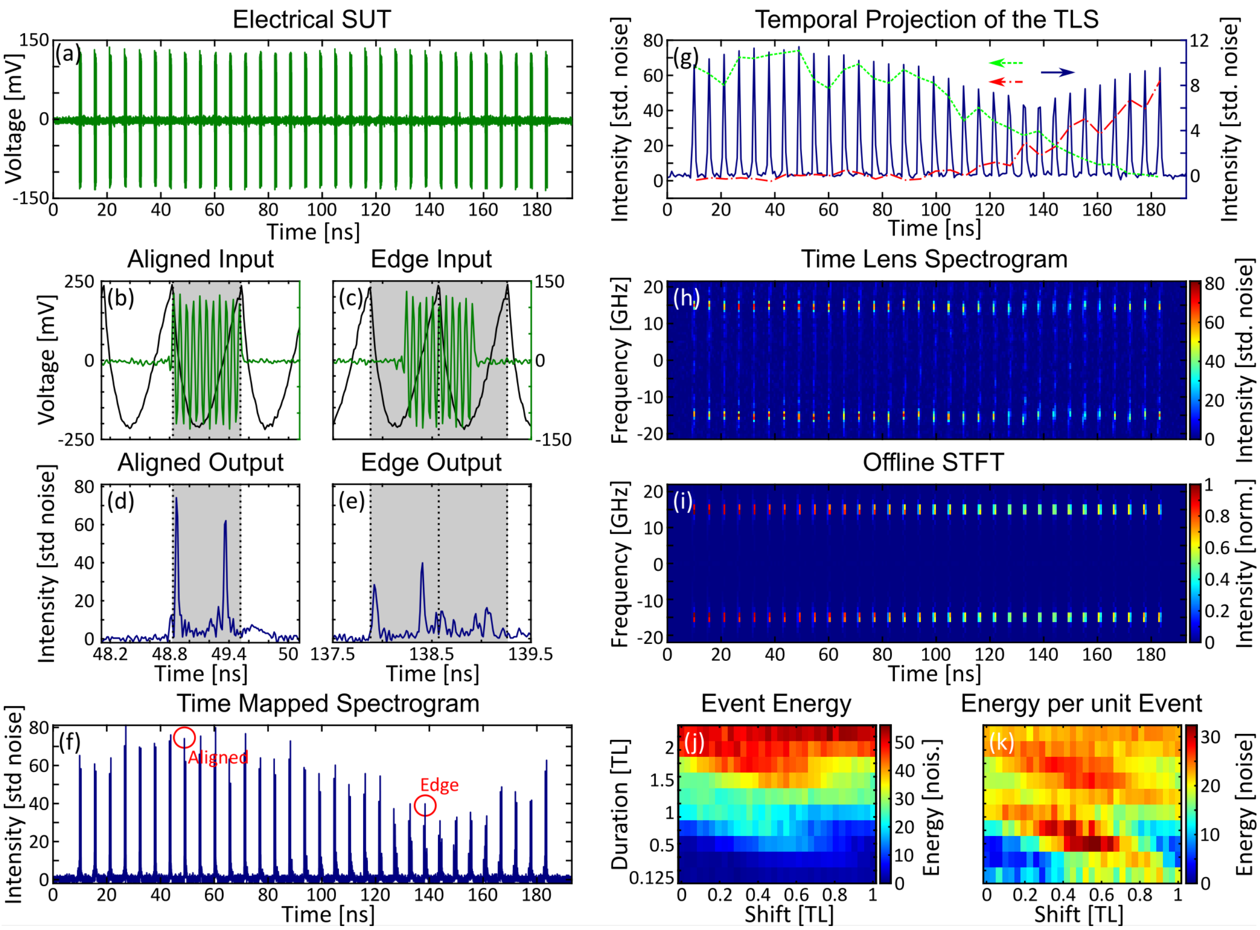

FIGURE 5.5 : TLS for a finite collection of a series of transient events with a microwave carrier of 15 GHz. Each short transient is repeated 32 times, and there are 9 of these series of transients for a variety of durations. One of these series is shown in (a), whose events are the same duration as the time resolution of the TLS (696 ps). Each event in a series is shifted by 1/32 of a time resolution, so that over the whole series the events take every position possible in terms of alignment with the time lenses. (b), (c) Short transient events aligned with the center of the first lens and the edge between the first and second lens, respectively. (d), (e) Time mapped spectra of the events from each lens, with the output lens over which the energy is distributed is shown in grey. (f) Time mapped spectra for all events in the series, highlighting the aligned and edge cases in red. (g) Temporal projection of the TLS shown in blue, summing the full energy of each output spectra, and dividing by the number of analysis points. The green dashed line displays the detected intensity of the transient tone frequency within the first lens (i.e., the lens when the event is aligned with the center, shown in (b)), while the red dashed/dotted line displays the value for the lens directly after, as the event is shifted from one to the next. (h) TLS output showing the double-sided spectra for the entire series. (i) An offline STFT is performed with the same analysis window as the TLS and shifted to match the alignment with the series. (j) Using a small area of 3 frequency points by 3 time points around each event, the values of the spectrogram are summed and divided by the noise found in the same time-frequency area, for all series of all durations. (k) The values for each duration and temporal shift are divided by the duration of the event in units of the time resolution. For a perfect system capturing all the energy incident on the TLS, this plot should be near to a single color.

5.6 Frequency Hopping Signals

In contrast to the high temporal resolution of the TLS, the TAIS excels in providing extremely high frequency resolution as shown in previous sections. In this respect, the TAIS and the TLS are complementary systems able to address a wider range of applications using the same devices. The following application-oriented signal is meant to provide a concrete demonstration of the superior performance possibilities enabled by the two photonics spectrograms in comparison to DSP, as well as other specialized photonics methods. In particular, an ultrafast, broadband frequency hopping signal with multiple channels is analysed by a single TAIS or TLS system. The SUT consists of 20 evenly spaced frequency levels from 1 GHz to 21 GHz, turning on and off randomly, resulting in events of various durations down to the nanosecond scale and below, which cannot be identified using state-of-the-art DSP technologies. In fact, even the recently reported photonics methods for recovering frequency hopping signals (9; 23) are either very fast instantaneous frequency measurement devices, or are slower but can accommodate multiple simultaneous channels. Combining multiple photonics methods to achieve both fast hopping speeds for multiple channels may be possible but would dramatically increase cost, complexity, and footprint.

In the results presented, the largest event duration consists of two hops together, but there is in principle no limit as the spectrograms are both real-time. Two different conditions are tested for both the TLS and the TAIS. The first is when the smallest hop duration is set to be equal to ten times the TLS time resolution $10 \cdot 696ps = 6.96ns$, which is larger than the TAIS resolution $T = 4.48ns$ by a factor of 1.56. The second is when the minimum hop duration is $1.39ns$ (twice the TLS resolution) and 0.31 times the TAIS resolution. The number of available analysis points from the TAIS is 206 per double sided spectrum. Therefore, this TAIS could accommodate over 100 simultaneous and arbitrary frequency channels with a hopping period below 5 ns. The potential number of channels becomes even larger in the case of the higher bandwidth TAIS with a detection deteriorated 716 analysis points. In the second case of 1.39 ns hop durations, it is expected that the TAIS will not be able to properly resolve each hop in time, while the TLS will struggle to resolve hops which are close in frequency. In neither case were the hops of the SUT synchronized with the TLS or TAIS systems, and as a result the hops arrive at an unknown position on the analysis windows.

The electrical SUT of the frequency hops, recovered directly from the oscilloscope, is shown in figure 5.6 along with the full digital Fourier transform. 43 peaks in total can be seen in Fourier transform figure, representing 20 evenly spaced frequency levels on each side of a central frequency peak, as well as two unintended side lobe frequencies outside of the TLS and TAIS analysis bandwidth.

The TAIS for the long hop duration case is shown in Figure 5.7. The spectra of the SUT measured by the OSA is shown in Figure 5.7(a), along with the frequency projection of the resulting TAIS. Figure 5.7(b) displays the TAIS for a portion of the frequency hopping signal. Notice the impressive clarity of the individual hops, and keep in mind that no other method would be able to recover this signal in real time. Comparison with the offline STFT in Figure 5.7(c) shows that the TAIS is properly recovering the frequency and time of the events with sufficient resolution. The portion of the TAIS displayed in these two figures contains over 80 events, with multiple frequencies being present simultaneously. In Figure 5.7(d) the most hops present at once is 3 as a proof of concept demonstration, however the predicted maximum number of frequency channels would be on the order of one per analysis point on a single sided spectrum, in the case of the results presented,

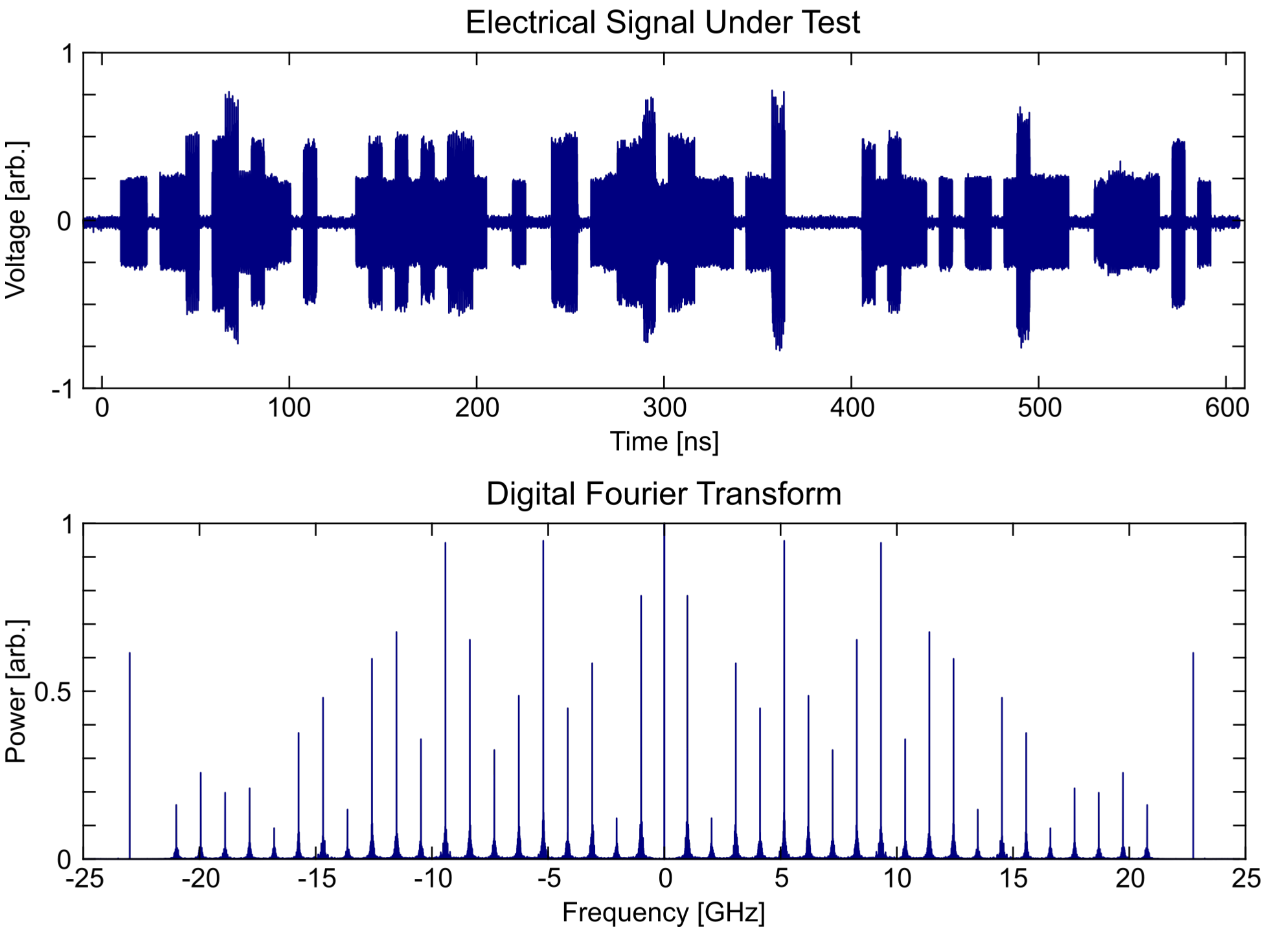

FIGURE 5.6 : Electrical SUT from the AWG for a small section of the signal with minimum hop duration equal to 10 T_L. Below, the Fourier transform of the signal, displaying the expected frequency channels. Additionally in the Fourier transform is a central frequency or DC peak, and two side lobe frequencies outside of the analysis bandwidth.

roughly 103. In Figure 5.7(d), (e) another area of the frequency hopping signal is shown with very closely spaced events and multiple frequencies occurring simultaneously.

The same portion of the signal is analysed by the TLS and shown in Figure 5.8. In Figure 5.8(a) it is clear to see that the TLS has insufficient frequency resolution to resolve the frequency channels by simply using a frequency projection. Figure 5.8(b) and 5.8(c) show the TLS and the offline STFT for the same time-frequency resolutions. Figure 5.8(a) is displayed with the minimum colour set to 4 times the standard deviation of the noise as the TLS does not provide the same clarity as the TAIS due to the number of analysis points. It is still possible to distinguish hops if there are no others close in frequency, as shown in the zoomed sections of Figure 5.8(d) and 5.8(e). In these subfigures it is also possible to see just how many more temporal analysis points the TLS provides in comparison to the TAIS for the exact same hop duration widths.

The superior frequency resolution is certainly an advantage the TAIS has for frequency hopping signals, but the TLS is advantageous for increasing the hopping rate due to it's impressive temporal resolution. The TLS and the TAIS for the same frequency hopping signal as before, but now with

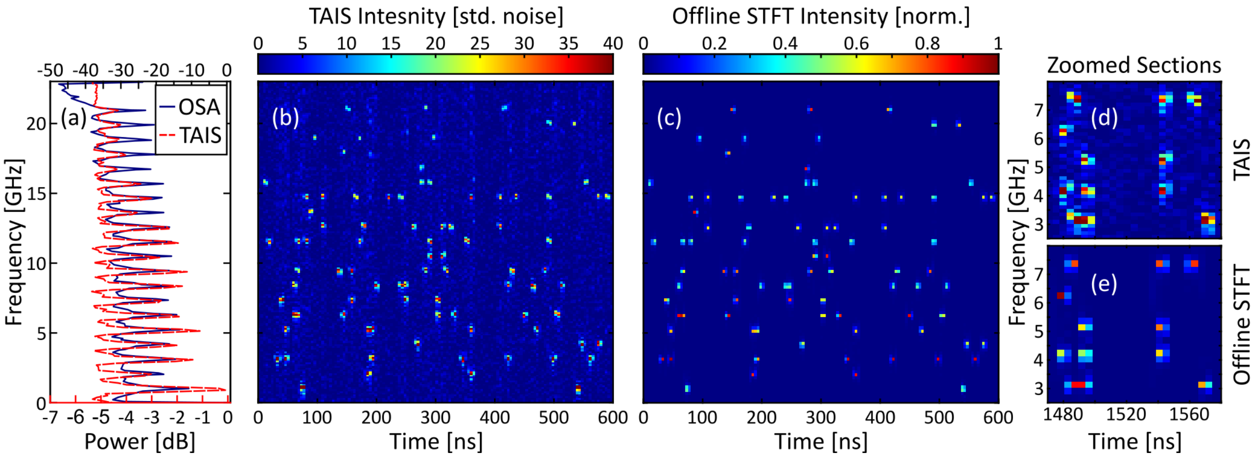

FIGURE 5.7 : Frequency hopping signal analysed by the TAIS, compared with the offline STFT (not real time analysis) of the electronic SUT. The signal consists of more than 80 time-frequency events occurring over a duration of around 600 ns and with 20 evenly spaced frequency levels from 1 to 21 GHz. Many frequency events can occur simultaneously or in very close temporal proximity. (a) The projection of the TAIS onto the frequency domain is overlayed onto the spectrum from the OSA measuring the microwave on optical SUT. (b) The real-time spectrogram obtained by the TAIS. (c) The offline STFT of the electrical signal from the AWG, using an analysis window the same size as the TAIS. (d), (c) Two small, zoomed sections from another part of the frequency hopping signal are shown for the TAIS and the offline STFT respectively.

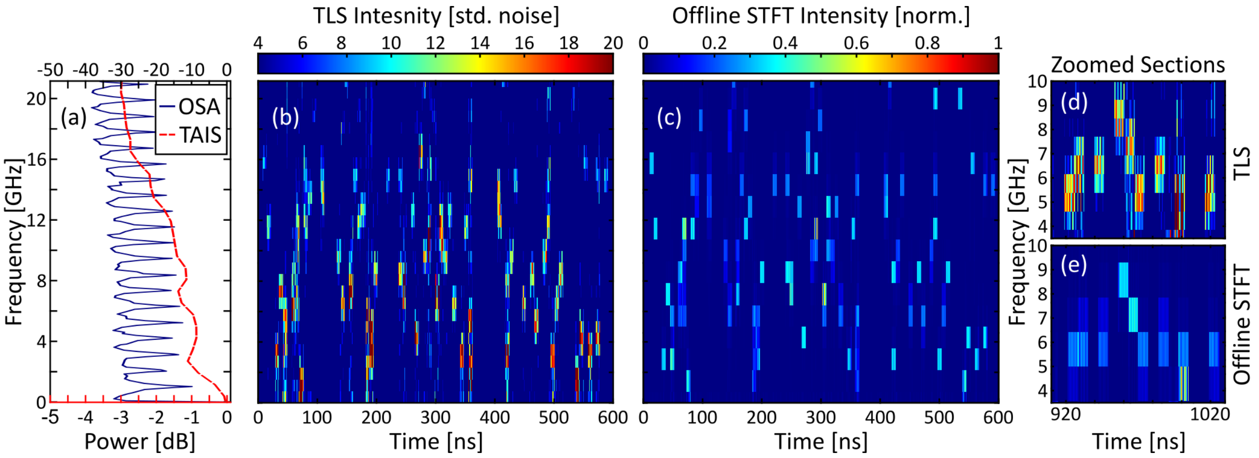

FIGURE 5.8 : Frequency hopping analysed by the TLS, compared with the offline STFT (not real time analysis) of the electronic SUT. The signal consists of more than 80 time-frequency events occurring over a duration of around 600 ns and with 20 evenly spaced frequency levels from 1 to 21 GHz. Many frequency events can occur simultaneously or in very close temporal proximity. (a) The projection of the TLS onto the frequency domain is overlayed onto the spectrum from the OSA measuring the microwave on optical SUT. (b) The real-time spectrogram obtained by the TLS. (c) The offline STFT of the electrical SUT from the AWG, using an analysis window the same size as the TLS. (d), (c) Two small, zoomed sections from another part of the frequency hopping signal are shown for the TLS and the offline STFT respectively.

a shorter hopping time of 1.39 ns are shown in Figure 5.9(a) and 5.9(b), respectively. As the frequency hops are significantly shorter (1.39 ns) than the TAIS temporal resolution (4.48 ns), it is expected that hops closely spaced in time will interfere and destroy the possibility of recovery. Even though these figures display the analysis of the exact same signal, they look almost like different sequences entirely due to the time resolution of the TAIS. This figure shows that the TLS can outperform the TAIS for the recovery of frequency hopping signals if the hopping speed is too

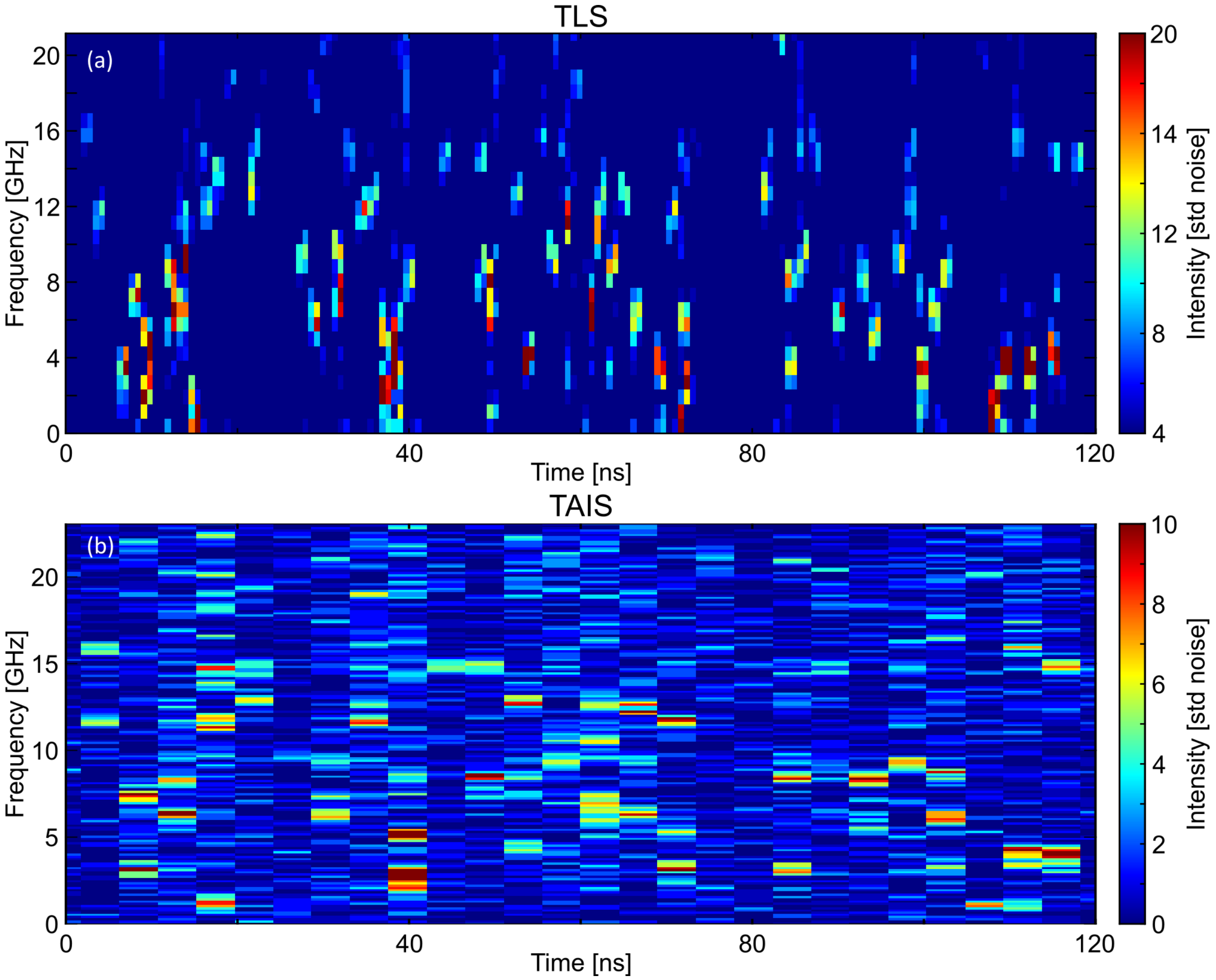

FIGURE 5.9 : Fast frequency hopping signal with 1.39 ns hop periods, 20 frequency levels from 1 to 21 GHz. (a) The TLS, with time resolution 696 ps, recovers the hops successfully if the frequency spacing is sufficient (i.e., beyond the 1.44 GHz frequency resolution). (b) The TAIS, which has a time resolution of 4.48 ns, cannot recover the frequency hops with any reasonable amount of clarity, and is corrupted by many noise artifacts.

fast for the TAIS, but importantly the TLS still suffers from poor frequency resolution. By balancing the number of frequency channels with the hopping period, it would be possible to maximize the potential information capacity for the TLS and the TAIS based on the trade offs from section 3.3.

Further analysis of the time and frequency resolutions can be done by taking the marginals, or projections from the 2D representations into the 1D time or frequency functions. These are compared to the optical SUT intensity recovered with the photodetector and oscilloscope. In particular, the lower resolution projections should follow the true 1D functions in either domain. The frequency resolutions have already been displayed in Figure 5.7 and Figure 5.8 for the TAIS and the TLS, respectively. Figure 5.10 shows the projections onto the time domain for the long hop duration case. There is a striking difference between the resolutions, as the TLS easily follows the intensity of the SUT with 10 points per hop. The TAIS on the other hand only has approximately 1.56 time points per hop, and is nearing the temporal limit to what it can recover.

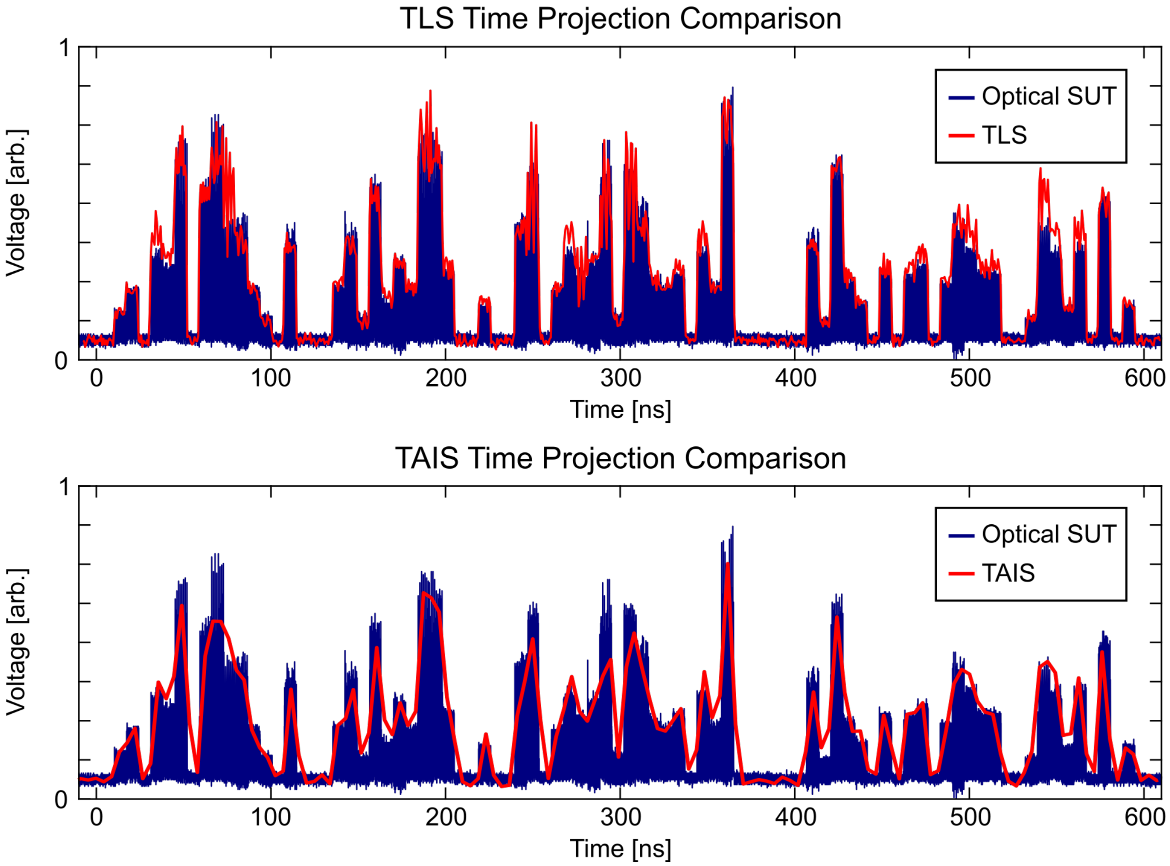

FIGURE 5.10 : Comparison between the optically detected SUT and the TLS and TAIS time projections. The TLS time projection follows closer to the expected or true temporal profile, as the TLS allows for 10 temporal analysis points per hopping period. The TAIS projection still follows the outline of the temporal profile, but only with an average of 1.56 temporal analysis points per hopping period.

In figure 5.11 the time projections for the shorter hop durations are shown. As the hop duration is only twice the time resolution of the TLS, the system is nearing the limits of resolvability. This figure confirms that TAIS on the other hand is well past the resolution limits, and the time projection becomes only vaguely similar to the actual optical SUT intensity.

The frequency hopping signal demonstrates that the TLS and the TAIS can be seen as complementary systems. As discussed in the theory section, device limitations mainly impact the frequency resolution of the TLS, while the impact for the TAIS is limited time resolution and bandwidth. Attempting to recover a spectrogram of the frequency hopping signals presented in this section using a state of the art real-time spectrum analyser would result in all of these events being processed in only a few analysis windows at best. Thus, with the available DSP the frequency hops would be completely unidentifiable. Furthermore, the recently reported photonics methods for recovering frequency hopping signals are either limited in hopping speed or number of channels and bandwidth capable of being analysed. The performance advantages of the TLS and especially the TAIS over the state-of-the-art for frequency hopping signals enables treatment of an increased number of simultaneous channels and a dramatic increase in hopping speed. Both of these

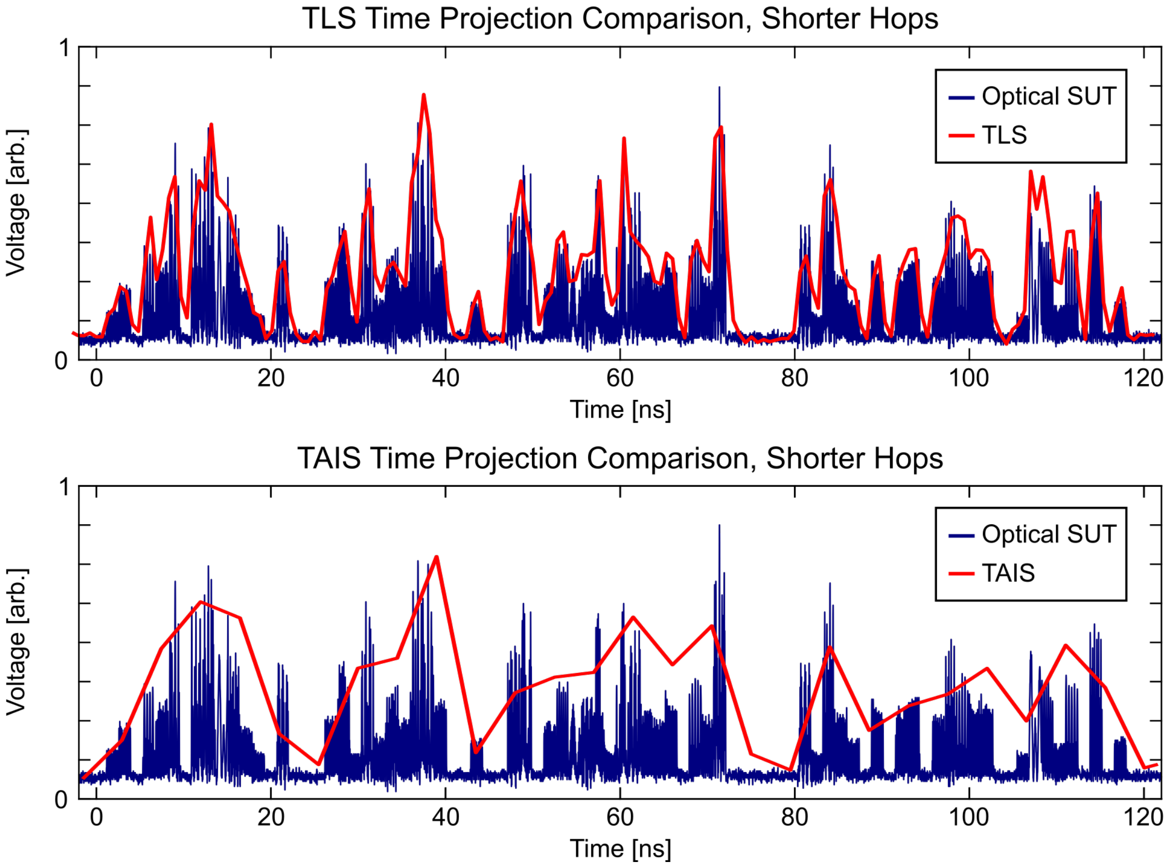

FIGURE 5.11 : Comparison between the optically detected SUT and the TLS and TAIS time projections for the shorter frequency hops of 1.39 ns. The TLS with temporal resolution 696 ps is still sufficient to resolve the intensity features shown in the actual optical SUT trace from the RTO. The TAIS, with temporal resolution of 4.48 ns is not capable of meaningfully resolving most of the temporal features, and as a result the TAIS cannot recover the frequency hops.

increases directly correspond to dramatic increases in potential data rate, alongside an increase in security.

5.7 Optical Signals

5.7.1 Introduction to Optical Signals

All the previous spectrograms displayed in this thesis have been symmetric, that is, the positive and negative frequencies (relative to the carrier) are mirror images of one another. This is due to the way in which the electo-optic modulation was performed, producing a double-sided spectrum of width in the 10s of GHz range, centred around the carrier frequency of 193.5 THz. From a physical perspective, the use of complex notation in the Fourier transform is for convenience only (78; 79; 80). Complex notation is an (extremely) useful mathematical tool for describing waves which are, in reality, real and not imaginary displacements of observable fields. The aim of this section is not to delve into the ontology of optical waves however, but it is worth at least mentioning that the mathematical descriptions used should not corrupt how one thinks about optical communications. If we were to detect the electric field oscillations of an optical communications signal, and perform a Fourier transform, we would recover a double sided spectrum centred around the zero frequency (i.e., DC) with symmetric features at $\pm$ 193.5 THz. From an electro-optics perspective however, the carrier frequency of 193.5 THz is indistinguishable from DC current (if you don't believe me, take a look at any optical continuous wave source with any available photodetector and real-time oscilloscope). This indistinguishability is due to the sample rate of the oscilloscope being nowhere near fast enough to properly sample the waveform, even if the photodetector could properly down-convert into the electrical domain. Therefore, it is possible to artificially create a "complex valued signal" using physically real waves. The result would be an asymmetric microwave bandwidth spectrum implicitly centred around the central frequency of an optical carrier. The essential difference between a symmetric and asymmetric spectrum is phase information (recall sec 2.2), which have been ignored until now. Therefore, the following final results will be dedicated to complex modulated optical signals.

Recall the essential characteristics of the TLS and the TAIS is that they are capable of continuous analysis of signals not periodic nor limited in time, they are gapless in that they have no breaks in acquisition, and they are ultrafast in time and ultrabroad in frequency. Pose the following question then: what type of signals test simultaneously all of these properties, and furthermore include nontrivial, ultrafast phase variations which would result in the asymmetric spectra discussed? One possible answer is coherent communications in the field of optical telecommunications. Quadrature amplitude modulation (QAM) formats have phase variations on the scale of nanoseconds or below, and are potentially continuous over time scales which may be considered infinite (milliseconds or greater) for all practical purposes.

Recovering QAM signals, or any other signals with phase information, is not as simple as using a photodetector and digitizing. Instead, complex systems involving interference either with the SUT or a phase stable local oscillator, as well as multiple photodetectors and extensive DSP is employed

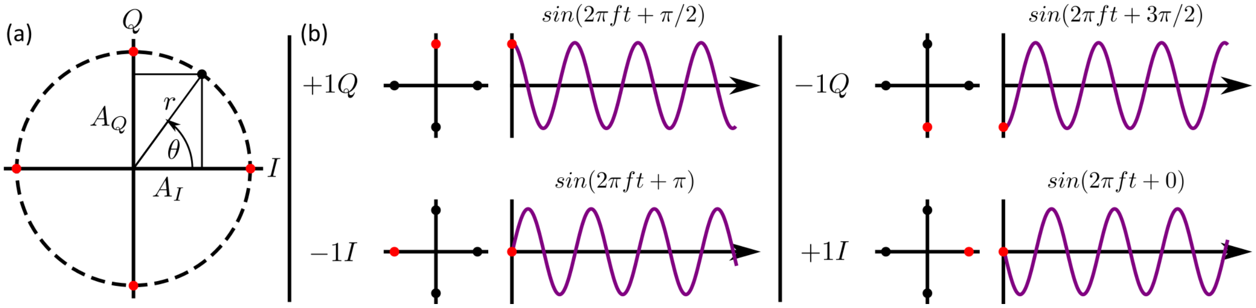

Figure 5.12 : Conceptual diagram of in-phase (I) and quadrature (Q) components of a wave with phase information. Either the amplitudes in the I and Q direction can be specified (denoted here by A_I and A_Q), or the relative phase θ and the intensity r^2 of the carrier wave. For a modulation format with four possible "symbols", or unique points on the IQ diagram, there are four possible waves to send. Notice that two degrees of freedom gives a 2 dimensional space in which information can be encoded, rather than an intensity only modulation format.

(81). These considerations result in a more complex, expensive system, with a larger footprint and high energy consumption. The innovative approach that will be described in this section almost entirely avoids the requirements for typical complex communication signal recovery. Specifically, the TLS is shown to recover these signals using no interferometry, only a single optical path, a single photodiode, and a very simple digital algorithm for the final data stream reconstruction. To my knowledge, this is the first time that time-frequency analysis has been used for the actual data decoding and recovery of complex communications.

5.7.2 Theory of Phase Recovery for Coherent Communications

In this section I will describe why it is expected that the TLS should be able to successfully recover coherent communications signals. QAM signals are generated by controlling both the intensity and relative phase of an optical wave (82; 44). This relates directly to the polar coordinate representation of a point in two dimensional space, which can also be given in rectilinear coordinates. Using the rectilinear coordinates, two intensity only modulation formats are combined, with a relative phase of $\pi/2$. This is what leads to the (I)n-phase and (Q)uadrature notation of an IQM. The concept of an IQ diagram and using the phase of the wave to encode information is shown in Figure 5.12.

Once a QAM signal is generated, the TLS temporal phase modulation pattern is aligned such that the TLS images the transition from one symbol to the next. This is not a very strict synchronicity requirement, as the transitions between symbols usually happen quite fast, so the only alignment which would cause issues would be perfect alignment of the transitions on the edges of the time lenses. The working condition implements an entirely self-referenced differential intensity detection of the phase information without the need for interferometric or optical phase locking schemes and in an entirely colorless fashion (independent of carrier wavelength). The change of phase from one symbol to the next results in an instantaneous frequency shift, which also depends on the intensity and transition function. Therefore, each intensity and phase transition corresponds to a unique

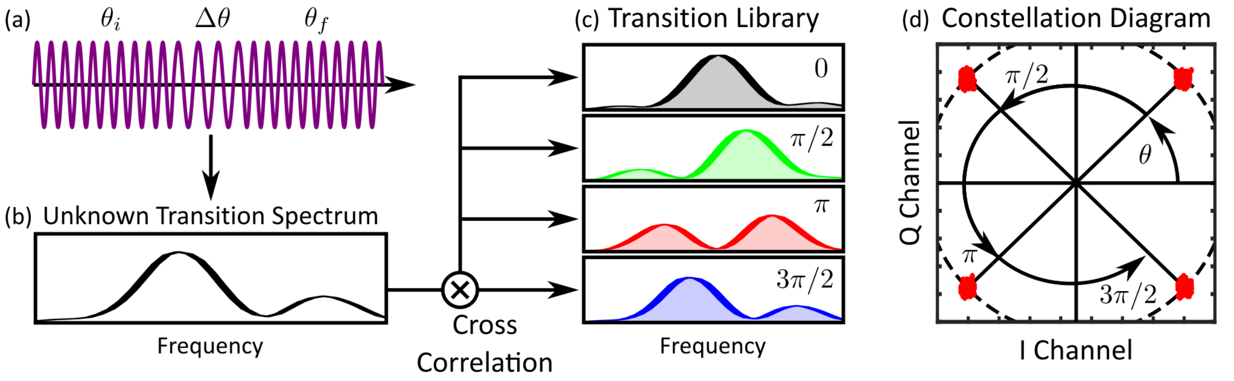

FIGURE 5.13 : Concept of the recovery of phase of an optical wave (a) using the spectrum of the transition from one relative phase θ_i to the next θ_f. The phase difference $\Delta\theta$, potentially in conjunction with an intensity change, creates a shift in the instantaneous frequency and a spectral pattern unique to the transition (b). (c) The unknown transition is compared with a decision method (cross correlation in this case) to a library of all possible transitions constructed beforehand. (d) The next symbol in the pattern can then be determined by the closest fit from the decision method.

spectral fingerprint. Because of this, recovering the time mapped Fourier transform of the symbol transition gives all the required information on the specific changes. By comparing an unknown transition with a complete set or library of spectra from a calibration sequence containing all possible transitions, the phase and intensity change sequence can be reconstructed. The calibration spectrum that maximizes the decision function with the spectrum under test is chosen as its match to determine the encoded phase and intensity changes. This decision method and analysis of the measured spectrogram were performed offline, but they could be implemented in real-time and conceivably using photonic approaches. This process is shown for QAM4 in Figure 5.13.

5.7.3 Coherent Communications Results

For the experimental demonstration of the TLS applied to QAM signals, the intensity modulator in the signal generation step is replaced with an in-phase and quadrature modulator (IQM). The time aperture of the TLS is chosen to be 1 ns, and the dispersion 15,713 ps^2. The (I)n-phase and (Q)uadrature channels of the signal are generated separately by the AWG and combined in the IQM to make a coherent pseudo-random bit sequence (PRBS). The QAM signals are all chosen with a baud rate of 1 Gbaud to match the Fourier transform rate of the TLS, and aligned with the transition between symbols as in Figure 5.13. The time-mapped spectrogram is recovered in real-time using a 50 GHz detector and 28 GHz RTO. The decision method was the cross correlation function implemented offline, and defined as

$$\rho(T,L) = \frac{1}{N-1}\sum_{i}^{N}\left(\frac{T_i-\mu_T}{\sigma_T}\right)\left(\frac{L_i-\mu_L}{\sigma_L}\right). \tag{5.1}$$

The TLS for the QAM4 modulation format is shown Figure 5.14, where each vertical slice represents the Fourier transform of a transition from one symbol to the next. The ability of the

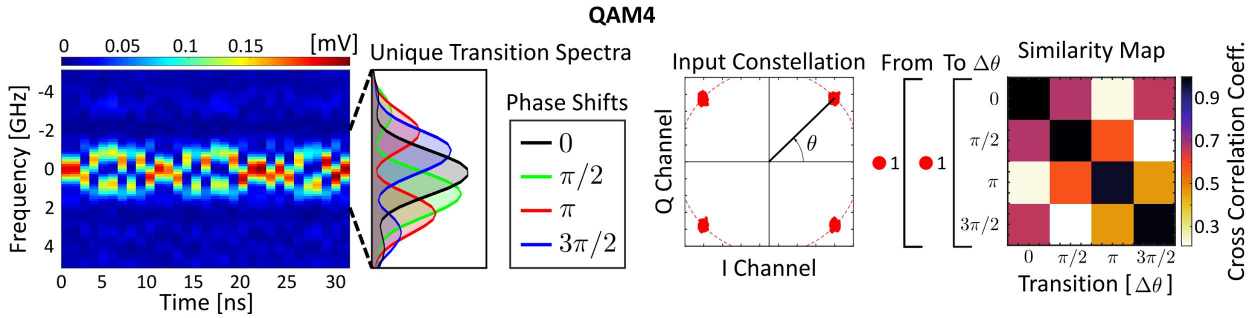

FIGURE 5.14 : TLS for a QAM4 PRBS. The two dimensional spectrogram image shown displays the spectrogram of the complete calibration sequence for QAM4. This includes all possible transitions from one symbol to any other symbol. Redundancy is included to ensure that all symbols can be treated equally, and only the phase change matters. A zoomed section of the spectrogram is shown to the right, where transitions resulting from similar phase changes have all been averaged. Further right is the input constellation using the I and Q channels from the AWG. To construct the similarity map, two different calibration sequences were taken. For QAM4, each of these sequences was 31 transitions long. Then, the cross correlation coefficient was calculated for every transition of the first sequence to every transition of the second sequence. All coefficients from transitions resulting in the same pair of phase changes were averaged, and the value plotted as shown.

spectrogram to discriminate the different unique transitions can be shown by superimposing their spectra, creating an analogous “frequency-domain eye diagram” for the TLS, shown to the right of the spectrogram in Figure 5.14. The right side of Figure 5.14 shows the constellation diagram of input symbols from the electrical AWG I and Q signals. Comparing all unique transitions of one calibration sequence to another via cross correlation results in the similarity map shown. The greater the difference between diagonal values and off-diagonal values, the greater the efficacy of using this particular decision method (cross correlation). Since for QAM4, there is only a single intensity level, the only differentiating feature is the phase change $\Delta\theta$, which can have four values. The clarity of this similarity map accounts for the low error rate for QAM4. Among the 2^{23-1} symbols tested, no errors were found, resulting in a pre-forward error correction bit error rate (pre-FEC BER) of $< 5.96 \times 10^{-8}$.

Figure 5.15(a) shows the constellation diagram and similarity map for QAM8. In this case, there are two intensity levels (indicated by the colors and dotted circles). The lower level of QAM8 (red circles) by itself is analogous to QAM4, so it is expected that for changes within these points a very similar pattern to the similarity map of QAM4 should be observed. For the 2^{19-1} symbols tested in the PRBS, 98 errors were found resulting in a pre-FEC BER of 6.23×10^{-5}, still well within acceptable ranges for error correcting codes (ECCs) (83). Figure 5.15(b) shows the constellation diagram and similarity map for QAM16, which contains three intensity levels. The density of spectra dramatically increases, so it is expected that there arise issues, as confirmed by the darker regions not on the diagonal. For 2^{17-1} PRBS symbols tested, 3930 errors were counted, resulting in a pre-FEC BER of 7.50×10^{-3}. It is expected that it will become increasingly difficult to differentiate between the various transitions as the modulation order increases. Since the TLS analysis rate is set to the baud rate of the data signal, the bandwidth of a transition will be within a fraction of the total analysis bandwidth of the TLS. This is because the π phase transition defines the maximum possible frequency shift. For higher order modulations, the number of unique spectral signatures

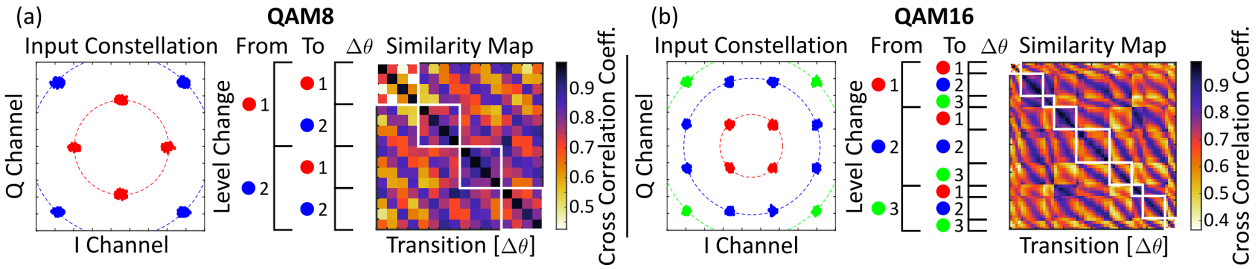

FIGURE 5.15 : (a) TLS applied to a QAM8 PRBS. The input constellation of the QAM8 sequence is shown, which includes two phase levels. During the analysis, it was found that for this particular decision method, an intensity level increase was discernable to an intensity level decrease, even if there was the same phase change between the symbols. Therefore, separating further the averaging in the similarity map to include information of the starting and ending intensity level improves the BER. (b) The constellation diagram for a QAM16 PRBS is shown, with three intensity levels. QAM16 includes some transitions which are comprised of intensity changes only, and a zero change in phase. In this case, the transition still produces an identifiable change. In the sequence tested, no one particular transition or symbol was found to be particularly troublesome above the others.

increases without any increase in the bandwidth that they cover, making them increasingly difficult to recover due to the limited number of analysis points relevant to the transition spectra (i.e., limited by the spectral resolution). However, it is possible that a more sophisticated lens system, as well as other methods to tailored the system to recovering complex communications data signals, could be considered. To reiterate, this is the first reported demonstration of the use of real-time joint TF signal analysis for the recovery of complex-modulation optical data signals, and uses self referenced intensity-only measurements. This is extremely promising, as the removal of the local oscillator as well as the intense DSP dramatically simplifies the system and has the potential to be competitive with certain short range telecommunication systems.

6 CONCLUSION

6.1 Summary

In this thesis, a theoretical link between the time lens spectrogram and the Talbot array illuminator spectrogram has been demonstrated. Their capabilities for ultrafast, broadband, gapless, and real-time microwave signal analysis were shown, as well as a thorough technical and experimental analysis of their design parameters and trade-offs. Using commercially available electro-optics, a 46 GHz bandwidth signal was recovered using only a cost-effective 6 GHz photodiode. Of particular and immediate interest are the applications stemming from the recovery of an ultrafast frequency hopping signal with nanosecond scale hops and multiple simultaneous channels over 20 GHz of real bandwidth. These spectrograms present easily the most impressive performance for cognitive communications in literature so far.

A brief demonstration of the capability to recover optical signals with phase information was also shown. The ability of coherent communications to be recovered by these spectrograms in a manner which relies on non-interferometric, intensity only detection is unique to this system. The simplicity over coherent detection techniques involving stable local oscillators or extensive digital signal processing makes the TLS and TAIS competitive for optical telecommunications in certain applications. Further details on the possibilities for spectroscopy, ultrafast characterization, and LIDAR are found in the credited publications.

6.2 Future Work

The possible directions enabled by the development of the TLS and the TAIS are extensive. So far, only two ranges of the electromagnetic spectrum have been investigated, for a small sample size of the possible applications from ultrafast characterization to medicine.

6.2.1 Fresnel Lens

The Fresnel lens is meant to solve the issue of large phase accumulation in phase modulation (84). This is done by wrapping the phase modulation function to 2π, and thereby reducing the requirements of the devices to only require this strength of modulation. For a quadratic function, the edges of the lens begin to wrap faster and faster, and thus require more bandwidth for wider lenses. The quadratic phase modulation of the TLS, the lens does not require high bandwidth, but does utilize the full strength of the phase modulator. The TAI lens on the other hand also wraps to 2π, but is a discrete pattern with a constant step width, and therefore maintains the same required bandwidth over the entire lens. This contributed to the choice of a TAI lens over a Fresnel lens for the spectrogram. Both the Fresnel and the TAI lens however do not use the full modulation strength of the phase modulator. By wrapping the modulation function at the limit of the maximum phase modulation strength instead of 2π, the modified Fresnel lens would use the full bandwidth and full modulation strength of the impressive devices available. This could potentially increase the maximum bandwidth beyond the capabilities of the TLS (into a natural THz bandwidth range), while improving the frequency resolution and number of analysis points to utilize slower detection devices like the TAIS.

6.2.2 On Chip Implementation

To use the TLS or TAIS system in a practical application, it is very likely that using a very expensive and delicate arbitrary waveform generator to construct the lens functions is not acceptable. Since the TLS and TAIS are known periodic functions, it would not be necessary to use an arbitrary generator. The much simpler TLS could be implemented by an RF oscillator and full wave rectifier circuit based on Schottky diodes (85). Both of these devices have been implemented on chip and in very small form factors at the required speeds. As I am not a photonics on chip expert, I cannot comment on the feasibility that every piece of the TLS could be implemented on the same chip. Certainly, specifically designing chips to generate the phase patterns for the TLS would significantly reduce the cost and footprint, rather than employing devices suitable for arbitrary control.

6.2.3 Nonlinear Phase Modulation

The electro-optic phase modulation used is simple and easy implementation. Using nonlinear optics however, such as cross phase modulation (XPM) or four wave mixing (FWM), allows for a significantly improved phase modulation strength and speed. Time lenses with nonlinear optics have already been demonstrated (86; 87), and constructing infinite periodic functions with near arbitrary control is a well studied technique using spectral shaping (88). Maximum phase excursions of above 100π have been shown to be possible (74), and would allow for TLS to achieve astonishing bandwidths at unprecedented Fourier transform rates and frequency resolutions comparable to the TAIS. The requirement for chromatic dispersion also is reduced with a shorter time lens, making this aspect of the TLS easier to implement as the Fourier transform rate is increased. The difficulty with using nonlinear optics, and dramatically increasing the speed of the spectrogram, is that the detection required would likely not be possible to implement in real-time without a significant amount of parallelization and multiplexing.

6.2.4 Time-Frequency Filtering and Synthesis

The frequency-to-time mapping process allows for complete control of the JTFR features of a signal. Using an intensity modulator, it has already been demonstrated that unwanted spectral features can be removed by a user-defined, ultrafast programmable filter (22). This aspect is exciting due to the many applications relying on real-time signal filtering. The TLS and TAIS could also be used for waveform synthesis, where the entire process is reversed and the JTFR is defined at the input. This has the potential to easily create ultrafast frequency hopping signals, or even signals with phase information.

6.2.5 TLS and TAIS Connection

As mentioned in the 3 section, the Talbot phase found to be the discretization was only related to one possible case of the Talbot phase patterns. Specifically, the phase pattern which made the connection was the one in which the Talbot phase has an even number of phase levels or divisions in each lens. There is another phase equation which is similar, for odd values (65). In this thesis only even values were chosen, but odd ones have also been confirmed experimentally to work with the TAIS. A more general and rigorous derivation, including the proper definitions for the convolution of distributions, is left as future work.

6.2.6 Coherent Communications

One of the most exciting demonstrations, the recovery of coherent communications, is worth investigating further. Specifically, an in depth study could be performed on the effects of low signal to noise ratio, propagation distortions, and carrier phase drift (44; 89; 83). Furthermore, the use of reinforcement learning and neural networks to implement the decision method could significantly improve BER, without much additional demand to computation requirements. Lastly, the objective of the experiment was to recover rapid phase changes on a long continuous signal. This motivates the idea to design a phase modulation pattern with coherent communications in mind rather than necessitating spectrogram analysis specifically. All these factors position time-frequency analysis as a potentially competitive option for short range coherent data and telecommunications.

JOURNAL PUBLICATIONS

[JP1] B. Crockett*, C. Rowe*, and J. Azaña, “Capturing ultra-broadband complex-fields of arbitrary duration using a real-time spectrogram,” APL Photonics, featured article **8**, 066108 (2023). (*) authors have contributed equally, DOI: 10.1063/5.0145961.

[JP2] J. Azaña, X. Zhu, C. Rowe, and B. Crockett, “Optical Time-Mapped Spectrograms (II): Fractional Talbot Designs,” Journal of Lightwave Technology 1–12 (2023). DOI: 10.1109/JLT.2023.3260706.

[JP3] X. Zhu, B. Crockett, C. Rowe, and J. Azaña, “Agile manipulation of the time-frequency distribution of high-speed electromagnetic waves,” (2023). Submitted.

[JP4] A. Shoeib, M. P. Fernandez, C. M. Rowe, R. Maram, P. Riccaiardi, and J. Azaña, “Fiber-optics spectrum monitoring of WDM telecommunication signals with MHz update rates,” (2023). Submitted.

[JP5] C. Rowe, B. Crockett, X. Zhu, and J. Azaña, “Versatile Photonics Spectrograms for Ultrafast Real-Time Broadband Microwave Signal Analysis,” (2023). Submitted.

CONFERENCE PUBLICATIONS

[CP1] A. Shoeib, M. P. Fernández, C. M. Rowe, R. Maram, P. Riccaiardi, and J. Azaña, “Real-time Optical Monitoring of Telecom Data Signals Utilizing Dispersive Fourier Transformation,” in *IEEE Photonics Conference (IPC)* (Orlando, USA, 2023). In Press.

[CP2] B. Crockett, C. M. Rowe, and J. Azaña, “Self-referenced Full-field Acquisition of Optical Signals Via a Real-time Photonics Spectrogram,” in *IEEE Photonics Conference (IPC)* (Orlando, USA, 2023). In Press.

[CP3] X. Zhu, B. Crockett, C. M. Rowe, and J. Azaña, “Microwave Photonic Filter with user-defined reconfigurability and high frequency-selectivity,” in *IEEE International Topical Meeting on Microwave Photonics (IEEE MWP)* (Nanjing, China, 2023). In Press.

[CP4] X. Zhu, B. Crockett, C. M. Rowe, and J. Azaña, “Microwave Photonic Filter with Rapid Tunability and Arbitrary Reconfigurability,” in *European Conference on Optical Communications (ECOC)* (Glasgow, Scotland, 2023). In Press.

[CP5] C. M. Rowe, B. Crockett, and J. Azaña, “Advances in ultrafast photonic spectrograms towards sub-THz bandwidths,” in *General Assembly and Scientific Symposium of the International Union of Radio Science (URSI)* (Sapporo, Japan, 2023). In Press.

[CP6] X. Zhu, B. Crockett, C. M. L. Rowe, and J. Azaña, “Photonics-Based Real-Time Spectral Analysis Over 40-GHz Bandwidth with Fine Frequency Resolution,” in *2023 IEEE Research and Applications of Photonics in Defense Conference (RAPID)* (Miramar Beach, USA, 2023). DOI: 10.1109/RAPID54473.2023.10264773.

[CP7] C. M. Rowe, B. Crockett, and J. Azaña, “Intensity-only Detection and Decoding of Coherent Signals using a Photonics Spectrogram,” in *2023 IEEE Photonics Society Summer Topicals Meeting Series (SUM)* (Sicily, Italy, 2023). DOI: 10.1109/SUM57928.2023.10224369.

[CP8] B. Crockett, C. M. L. Rowe, and J. Azaña, “Phase Recovery of Ultrabroadband Waveforms Over Long Time Durations by Unwrapping a Photonic Spectrogram,” in *Advanced Photonics Congress 2023* (Busan, Korea, 2023). DOI: 10.1364/SPPCOM.2023.SpTu3E.3.

[CP9] B. Crockett, C. M. Rowe, and J. Azaña, “Continuous Time-Frequency Analysis of Ultrabroadband Optical Waveforms by Algorithmic Unwrapping,” in *2023 Conference on Lasers and Electro-Optics (CLEO)* (San Jose, USA, 2023). DOI: 10.1364/CLEO_AT.2023.AW3K.8.

[CP10] C. M. Rowe, B. Crockett, and J. Azaña, “Direct Intensity Detection of QAM Telecommunications Signals,” in *2023 Photonics North (PN)* (Montreal, Canada, 2023). DOI: 10.1109/PN58661.2023.10222942.

[CP11] B. Crockett, M. Connor Rowe, and J. Azaña, “Real-time spectral characterization of THz-bandwidth waveforms by unwrapping a time-lens spectrogram,” in *2023 Photonics North (PN)* (Montreal, Canada, 2023). DOI: 10.1109/PN58661.2023.10223063.

[CP12] X. Zhu, B. Crockett, C. M. L. Rowe, and J. Azaña, “Broadband and Fine-resolution Microwave Photonic Filtering with High-Speed Electronic Reconfigurability,” in *2023 Optical*

Fiber Communications Conference and Exhibition (OFC) (San Diego, USA, 2023). DOI: 10.23919/OFC49934.2023.10116973.

[CP13] X. Zhu, B. Crockett, C. M. L. Rowe, and J. Azaña, “Photonics-enabled Nanosecond Scale Real-time Spectral Analysis with 92-GHz Bandwidth and MHz resolution,” in *Optical Fiber Communication Conference (OFC) 2023* (San Diego, USA, 2023). DOI: 10.1364/OFC.2023.M1J.5.

[CP14] C. M. L. Rowe, B. Crockett, and J. Azaña, “Direct Intensity Detection of Complex Communication Data Signals Using a Real-time Photonics Spectrogram,” in *Optical Fiber Communication Conference (OFC) 2023* (San Diego, USA, 2023). DOI: 10.1364/OFC.2023.W4C.7.

[CP15] B. Crockett, R. Connor M.L., and J. Azana, “Ultrafast Spectrogram with Sub-THz Bandwidth,” in *2022 IEEE Photonics Conference (IPC)* (Vancouver, Canada, 2022). DOI: 10.1109/IPC53466.2022.9975608.

[CP16] C. M. L. Rowe, B. Crockett, and J. Azaña, “Photonics Enabled Real-time Spectrogram for Continuous Signal Processing,” in *Frontiers in Optics + Laser Science 2022 (FIO, LS)* (Rochester, USA, 2022). DOI: 10.1364/FIO.2022.JTu4A.71.

[CP17] C. M. Rowe, L. R. Cortes, H. G. De Chatellus, M. Seghilani, and J. Azana, “Generalized Talbot Self-Healing of Periodic Images,” in *2022 IEEE Photonics Society Summer Topicals Meeting Series (SUM)* (Cabo San Lucas, Mexico, 2022). DOI: 10.1109/SUM53465.2022.9858325.

[CP18] C. M. Rowe, B. Crockett, and J. Azana, “Photonic-Enabled Real-time Spectrogram Analysis of sub-Nanosecond Microwave Events over a 40-GHz Instantaneous Bandwidth,” in *2022 IEEE/MTT-S International Microwave Symposium - IMS 2022* (Denver, USA, 2022). DOI: 10.1109/IMS37962.2022.9865314.

[CP19] B. Crockett, C. M. Rowe, and J. Azaña, “Photonics-enabled Continuous and Gapless Time-frequency Analysis of Fast Transient Events,” in *Conference on Lasers and Electro-Optics* (San Jose, USA, 2022). DOI: 10.1364/CLEO_SI.2022.STh5M.5.

[CP20] C. M. Rowe, B. Crockett, and J. Azana, “Real-Time Gapless Analog Time Frequency Analysis for Bandwidths above 20 GHz with Nanosecond Resolution,” in *2021 European Conference on Optical Communication (ECOC)* (Bordeaux, France, 2021). DOI: 10.1109/ECOC52684.2021.9606086.

PATENT

[P1] C. M. Rowe, B. Crockett, and J. Azaña, “Method and System for Generating the Spectrogram of a Signal,” (2022). United States, Patent No. 17/931,566, Pending.

REFERENCES

[1] J. M. Grochowalski and T. Chady, “Pulsed Multifrequency Excitation and Spectrogram Eddy Current Testing (PMFES-ECT) for Nondestructive Evaluation of Conducting Materials,” Materials **14**, 5311 (2021).

[2] W. Wang, G. Zhang, L. Yang, V. Balaji, V. Elamaran, and N. Arunkumar, “Revisiting signal processing with spectrogram analysis on EEG, ECG and speech signals,” Future Generation Computer Systems **98**, 227–232 (2019).

[3] B. Pinkowski, “Principal component analysis of speech spectrogram images,” Pattern Recognition **30**, 777–787 (1997).

[4] J. F. Alm and J. S. Walker, “Time-Frequency Analysis of Musical Instruments,” SIAM Review **44**, 457–476 (2002).

[5] P. Neammalai, S. Phimoltares, and C. Lursinsap, “Speech and music classification using hybrid Form of spectrogram and fourier transformation,” in *Signal and Information Processing Association Annual Summit and Conference (APSIPA), 2014 Asia-Pacific* (IEEE, Chiang Mai, Thailand, 2014), 1–6.

[6] R. I. A. Harmanny, J. J. M. de Wit, and G. P. Cabic, “Radar micro-Doppler feature extraction using the spectrogram and the cepstrogram,” in *2014 11th European Radar Conference* (IEEE, Italy, 2014), 165–168.

[7] C. Dorrer and I. Kang, “Simultaneous temporal characterization of telecommunication optical pulses and modulators by use of spectrograms,” Optics Letters **27**, 1315 (2002).

[8] S. Rahman and D. A. Robertson, “Classification of drones and birds using convolutional neural networks applied to radar micro-Doppler spectrogram images,” IET Radar, Sonar & Navigation **14**, 653–661 (2020).

[9] Q. Liu and M. P. Fok, “Ultrafast and Wideband Microwave Photonic Frequency-Hopping Systems: A Review,” Applied Sciences **10** (2020).

[10] J. G. Mance, B. M. La Lone, D. H. Dolan, S. L. Payne, D. L. Ramsey, and L. R. Veeser, “Time-stretched photonic Doppler velocimetry,” Optics Express **27**, 25022 (2019).

[11] M. Li and J. Yao, “All-Optical Short-Time Fourier Transform Based on a Temporal Pulse-Shaping System Incorporating an Array of Cascaded Linearly Chirped Fiber Bragg Gratings,” IEEE Photonics Technology Letters **23**, 1439–1441 (2011).

[12] O. B. A. Nuruzzaman and B. Jalali, “Time-stretched short-time fourier transform,” IEEE Trans. Instrum. Meas. **55**, 598–602 (2006).

[13] “Application note 37w-17249-5: Fundamentals of real-time spectrum analysis,” (2015).

[14] P. Zuo, D. Ma, and Y. Chen, “Short-Time Fourier Transform Based on Stimulated Brillouin Scattering,” Journal of Lightwave Technology **40**, 5052–5061 (2022).

[15] J. Li, S. Fu, X. Xie, M. Xiang, Y. Dai, F. Yin, and Y. Qin, “Low-latency short-time Fourier Transform of microwave photonics processing,” Journal of Lightwave Technology 1–8 (2023).

[16] S. R. Konatham, R. Maram, L. Romero Cortés, J. H. Chang, L. Rusch, S. LaRochelle, H. Guillet de Chatellus, and J. Azaña, “Real-time gap-free dynamic waveform spectral analysis with nanosecond resolutions through analog signal processing,” Nature Communications **11**, 3309 (2020).

[17] B. Crockett, C. Rowe, and J. Azaña, “Capturing ultra-broadband complex-fields of arbitrary duration using a real-time spectrogram,” APL Photonics **8**, 066108 (2023).

[18] J. Azaña, X. Zhu, C. Rowe, and B. Crockett, “Optical Time-Mapped Spectrograms (II): Fractional Talbot Designs,” Journal of Lightwave Technology 1–12 (2023). DOI: 10.1109/JLT.2023.3260706.

[19] B. Kolner, “Space-time duality and the theory of temporal imaging,” IEEE Journal of Quantum Electronics **30**, 1951–1963 (1994).

[20] R. Salem, M. A. Foster, and A. L. Gaeta, “Application of space–time duality to ultrahigh-speed optical signal processing,” Advances in Optics and Photonics **5**, 274 (2013).

[21] J. Azana and X. Zhu, “Optical time-mapped spectrograms (I): from the time-lens Fourier transformer to the Talbot-based design,” Journal of Lightwave Technology 1–15 (2023).

[22] X. Zhu, B. Crockett, C. Rowe, and J. Azaña, “Agile manipulation of the time-frequency distribution of high-speed electromagnetic waves,” (2023). Submitted.

[23] L. A. Bui, “Recent advances in microwave photonics instantaneous frequency measurements,” Progress in Quantum Electronics **69**, 100237 (2020).

[24] A. D. Kilmer and M. Civil, “Old Babylonian Musical Instructions Relating to Hymnody,” Journal of Cuneiform Studies **38**, 94–98 (1986).

[25] H. F. Olson, *Music, Physics and Engineering* (Dover Publications, 1967).

[26] F. F. Arago, *Biographies of Distinguished Scientific Men. First series* (Ticknor and Fields, 1859).

[27] J. H. Lienhard, “Jean baptiste joseph fourier,” The Engines of our Ingenuity 1878 (2023).

[28] A. V. Oppenheim, A. S. Willsky, and S. H. Nawab, *Signals and Systems, 2nd Edition*, Prentice Hall signal processing series (Pearson, 1997).

[29] J. Fischer, “On the Duality of Discrete and Periodic Functions,” Mathematics **3**, 299–318 (2015).

[30] A. V. Oppenheim and R. W. Schafer, eds., *Discrete-time signal processing, 3rd Edition*, Prentice Hall signal processing series (Pearson, 2010).

[31] K. M. M. Prabhu, *Window functions and their applications in signal processing* (CRC Press/Taylor & Francis, Boca Raton, [Florida], 2014).

[32] J. W. Goodman, *Introduction to Fourier Optics* (W. H. Freeman and Company, 2017).

[33] E. Hecht, *Optics* (Pearson Education, Incorporated, 2017).

[34] R. Y. K. S. A. Akhmanov, A. P. Sukhorukov and A. S. Chirkin, “"on space-time analogy in the theory of nonlinear interaction of modulated electromagnetic waves",” in *3rd USSR Symp. on Nonlinear Optics* (1967).

[35] S. Akhmanov, A. Chirkin, K. Drabovich, A. Kovrigin, R. Khokhlov, and A. Sukhorukov, “Nonstationary nonlinear optical effects and ultrashort light pulse formation,” IEEE Journal of Quantum Electronics **4**, 598–605 (1968).

[36] B. H. Kolner and M. Nazarathy, “Temporal imaging with a time lens,” Opt. Lett. **14**, 630–632 (1989).

[37] B. H. Kolner, “Generalization of the concepts of focal length and f-number to space and time,” J. Opt. Soc. Am. A **11**, 3229–3234 (1994).

[38] S. D. J. R. Klauder, A. C. Price and W. J. Albersheim, “The theory and design of chirp radars,” Bell System Technical Journal **39**, 745–808 (1960).

[39] W. Caputi, “Stretch: A time-transformation technique,” IEEE Trans. Aerosp. Electron. Syst. **AES-7**, 269–278 (1971).

[40] J. van Howe and C. Xu, “Ultrafast optical signal processing based upon space-time dualities,” Journal of Lightwave Technology **24**, 2649–2662 (2006).

[41] J. Azana and M. Muriel, “Real-time optical spectrum analysis based on the time-space duality in chirped fiber gratings,” IEEE Journal of Quantum Electronics **36**, 517–526 (2000).

[42] C. P. Steinmetz, “Complex quantities and their use in electrical engineering,” in *Proceedings of the International Electrical Congress Held in the City of Chicago* (American Institute of Electrical Engineers, 1893), 33–74.

[43] C. Lee, *Microwave Photonics, Second Edition* (Taylor & Francis, 2013).

[44] “Roadmap of optical communications,” Journal of Optics **18**, 063002 (2016).

[45] A. Fresnel, *Mémoires vol. V* (l’Académie Royale des Sciences de l’Institut de France, 1826), chap. Mémoire sur la diffraction de la lumière.

[46] T. Jannson, “Real-time fourier transformation in dispersive optical fibers,” Opt. Lett. **8**, 232–234 (1983).

[47] B. H. Kolner, *Broadband Optical Modulators: Science, Technology, and Applications* (A. Chen and E. Murphy, eds. (CRC Press), 2011), chap. Chap. 19: Electro-optic time lenses for shaping and imaging optical waveforms.

[48] H. Talbot, “Lxxvi. facts relating to optical science. no. iv,” Philosophical Magazine Series 3 **9** (1836).

[49] J. W. S. Lord Rayleigh, “Xxv. on copying diffraction-gratings, and on some phenomena connected therewith,” Philosophical Magazine Series 5 **11** (1881).

[50] J. Goodman, *Introduction to Fourier Optics* (W. H. Freeman, 2017), 4th ed.

[51] W. D. Montgomery, “Self-imaging objects of infinite aperture,” Journal of the Optical Society of America **57** (1967).

[52] J. W. S. Lord Rayleigh, *The Theory of Sound | Vibrations of Membranes* (1877), 250–263.

[53] J. Jahns and A. Lohmann, “The lau effect (a diffraction experiment with incoherent illumination),” Optics Communications **28** (1979).

[54] A. W. Lohmann and J. A. Thomas, “Making an array illuminator based on the Talbot effect,” Applied Optics **29**, 4337 (1990).

[55] N. Streibl, “Beam shaping with optical array generators,” Journal of Modern Optics **36**, 1559–1573 (1989).

[56] O. Bryngdahl, “Image formation using self-imaging techniques∗,” J. Opt. Soc. Am. **63**, 416–419 (1973).

[57] P. Latimer and R. F. Crouse, “Talbot effect reinterpreted,” Applied Optics **31**, 80 (1992).

[58] M. V. Berry and S. Klein, “Integer, fractional and fractal talbot effects,” Journal of Modern Optics **43** (1996).

[59] K. Banaszek, K. Wódkiewicz, and W. P. Schleich, “Fractional talbot effect in phase space: A compact summation formula,” Opt. Express **2**, 169–172 (1998).

[60] M. Testorf and J. O.-C. neda, “Fractional talbot effect: analysis in phase space,” J. Opt. Soc. Am. A **13**, 119–125 (1996).

[61] L. Romero Cortés, R. Maram, H. Guillet de Chatellus, and J. Azaña, “Arbitrary energy-preserving control of optical pulse trains and frequency combs through generalized talbot effects,” Laser & Photonics Reviews **13**, 1900176 (2019).

[62] J. Azana and M. Muriel, “Temporal self-imaging effects: theory and application for multiplying pulse repetition rates,” IEEE Journal of Selected Topics in Quantum Electronics **7**, 728–744 (2001).

[63] C. R. Fernández-Pousa, R. Maram, and J. Azaña, “CW-to-pulse conversion using temporal Talbot array illuminators,” Optics Letters **42**, 2427 (2017).

[64] C. Zhou, S. Stankovic, and T. Tschudi, “Analytic phase-factor equations for Talbot array illuminations,” Applied Optics **38**, 284 (1999).

[65] L. R. Cortés, H. Guillet de Chatellus, and J. Azaña, “On the generality of the Talbot condition for inducing self-imaging effects on periodic objects,” Optics Letters **41**, 340 (2016).

[66] L. R. Cortéz, “Generalized talbot effect | theory and application to advanced optical wave processing,” Ph.D. thesis, Université du Québec, Institut national de la recherche scientifique (2018).

[67] V. Arrizón and J. Ojeda-Castañeda, “Multilevel phase gratings for array illuminators,” Applied Optics **33**, 5925 (1994).

[68] B. Crockett, L. Romero Cortés, S. R. Konatham, and J. Azaña, “Full recovery of ultrafast waveforms lost under noise,” Nature Communications **12**, 2402 (2021).

[69] B. Crockett, “Denoising amplification of arbitrary coherent signals using the talbot effect,” (2019). Masters Thesis, Université du Québec, Institut national de la recherche scientifique.

[70] J. Lighthill, *Introduction to Fourier Analysis and Generalised Functions* (Cambridge University Press, 1958).

[71] F. Friedlander and M. Joshi, *Introduction to the Theory of Distributions*, Introduction to the Theory of Distributions (Cambridge University Press, 1998).

[72] J. V. Fischer, “Four particular cases of the fourier transform,” Mathematics **6** (2018).

[73] C. R. Fernández-Pousa, “On the structure of quadratic Gauss sums in the Talbot effect,” Journal of the Optical Society of America A **34**, 732 (2017).

[74] R. Salem, M. A. Foster, A. C. Turner, D. F. Geraghty, M. Lipson, and A. L. Gaeta, “Optical time lens based on four-wave mixing on a silicon chip,” Optics Letters **33**, 1047 (2008).

[75] K. Technologies, “Infiniium UXR-B Series Oscilloscopes,” (2023).

[76] L. A. Bui, “Mach–Zehnder modulator condition for a low chirp factor versus DC bias,” Applied Optics **61**, 2643 (2022).

[77] B. Crockett, C. Rowe, and J. Azaña, “Capturing ultra-broadband complex-fields of arbitrary duration using a real-time spectrogram,” APL Photonics **8**, 066108 (2023).

[78] R. Lyons, “Does the fft generate artificial spectral components?” Vibrations Magazine (2012).

[79] R. G. Lyons, ed., *Streamlining digital signal processing: a tricks of the trade guidebook* (IEEE Press [u.a.], Piscataway, NJ, 2012), 2nd ed.

[80] R. Pachori, *Time-Frequency Analysis Techniques and their Applications* (CRC Press, 2023).

[81] D. Lavery, R. Maher, D. S. Millar, B. C. Thomsen, P. Bayvel, and S. J. Savory, “Digital Coherent Receivers for Long-Reach Optical Access Networks,” Journal of Lightwave Technology **31**, 609–620 (2013).

[82] K. Kikuchi, “Fundamentals of Coherent Optical Fiber Communications,” Journal of Lightwave Technology **34**, 157–179 (2016).

[83] T. Mizuochi, “Recent progress in forward error correction and its interplay with transmission impairments,” IEEE Journal of Selected Topics in Quantum Electronics **12**, 544–554 (2006).

[84] A. Davis and F. Kühnlenz, “Optical Design using Fresnel Lenses: Basic Principles and some Practical Examples,” Optik & Photonik **2**, 52–55 (2007).

[85] K. Li-Dessau, E. Ozbay, A. S. Hou, J. A. Sheridan, and D. M. Bloom, “Ultrafast measurements of 200-GHz GaAs Schottky photodiodes,” (San Diego, CA, 1993), 198.

[86] A. Klein, S. Shahal, G. Masri, H. Duadi, and M. Fridman, “Four Wave Mixing-Based Time Lens for Orthogonal Polarized Input Signals,” IEEE Photonics Journal **9**, 1–7 (2017).

[87] A. Klein, I. Sibony, S. Meir, S. Shahal, H. Duadi, and M. Fridman, “Overlapping Time-Lens Array,” IEEE Photonics Journal **11**, 1–6 (2019).

[88] M. P. Fernández, L. Romero Cortés, S. R. Konatham, B. Crockett, L. A. Bulus-Rossini, P. A. Costanzo-Caso, and J. Azaña, “Nonlinear time-lens with improved power efficiency through a discrete multilevel pump,” Optics Letters **45**, 3557 (2020).

[89] K. Kikuchi, *High Spectral Density Optical Communication Technologies* (Springer Berlin Heidelberg, 2010), chap. Coherent Optical Communications: Historical Perspectives and Future Directions.

[90] W. Duane Montgomery, “Algebraic formulation of diffraction applied to self imaging,” Journal of the Optical Society of America **58** (1968).

APPENDIX

A.1 Rectangular Window Functions and the Convolution Theorem

The following has no doubt been observed many times before, but I have not read about it anywhere, so it is included for your enjoyment. The convolution of two functions is a process by where one function $f(t)$ is multiplied by another function $g(t)$, delayed by a certain amount τ. The integral of this multiplication is computed to calculate the amount of overlapping area between the two, for every possible value of the delay τ. This is the convolution, defined as

$$(f * g)(t) \equiv \int_{-\infty}^{\infty} f(\tau) \cdot g(t-\tau) d\tau, \tag{7.1}$$

where the integration occurs over the delay variable τ. Ask the following question: is there a function $h(t)$ such that

$$(h * h)(t) \equiv \int_{-\infty}^{\infty} h(\tau) \cdot h(t-\tau) d\tau = h(t)? \tag{7.2}$$

In this section of the appendix, that question will be answered. The main tool to use is the convolution theorem, which states for two functions

$$\mathcal{F}\{f(t) \cdot g(t)\} = \mathcal{F}\{f(t)\} * \mathcal{F}\{g(t)\}, \tag{7.3}$$

where $\mathcal{F}$ denotes the Fourier transform. Define a rectangular window function $R(t)$ in the following way,

$$R(t) = \left\{ \begin{array}{lll} 0, & \text{if} & t > |1/2| \\ 1, & \text{if} & t \leq |1/2| \end{array} \right\}, \tag{7.4}$$

whose Fourier transform is a sinc function,

$$\mathcal{F}\{R(t)\} = \mathrm{sinc}(\omega), \tag{7.5}$$

for the Fourier dual variable ω. Notice

$$R(t) \cdot R(t) = R(t), \tag{7.6}$$

and in general

$$R^n(t) = R(t), \quad \forall n \in \mathbb{N}. \tag{7.7}$$

This is so far unsurprising and obvious. Consider $\mathcal{F}\{g(t) \cdot R(t)\}$ which by the convolution theorem is

$$\begin{aligned} \mathcal{F}\{g(t) \cdot R^n(t)\} &= \mathcal{F}\{g(t)\} * \mathcal{F}\{R^n(t)\} && (7.8) \\ &= \mathcal{F}\{g(t)\} * \mathcal{F}\{R(t)\} && (7.9) \\ &= \mathcal{F}\{g(t)\} * \mathrm{sinc}(\omega). && (7.10) \end{aligned}$$

But also,

$$\begin{aligned}\mathcal{F}\{g(t) \cdot R^n(t)\} &= \mathcal{F}\{g(t)\} * \mathcal{F}\{R^n(t)\} && (7.11)\\ &= \mathcal{F}\{g(t)\} * (\mathcal{F}\{R(t) \cdot R(t) \cdot ... \cdot R(t)\}) && (7.12)\\ &= \mathcal{F}\{g(t)\} * \operatorname{sinc}(\omega) * \operatorname{sinc}(\omega) * ... * \operatorname{sinc}(\omega) && (7.13)\\ &= \mathcal{F}\{g(t)\} * \operatorname{sinc}(\omega). && (7.14)\end{aligned}$$

Therefore, since $g(t)$ could have been any function, and even another rectangular function, we have that $\operatorname{sinc}(\omega)$ convolved with itself is exactly $\operatorname{sinc}(\omega)$. This result in the Fourier domain maybe slightly disturbing upon first glance, as the existence of a function that can be convolved infinitely many times with itself to produce the same result is quite surprising, and only makes intuitive sense by going back in to the rectangular function in the other domain. A further result can be proved for convolving differently scaled sinc functions by simply noting what happens in the Fourier domain with two rectangular window functions multiplied together. For two integers a and b, assume without loss of generality that $a < b$, then

$$\begin{aligned}\frac{1}{a}\operatorname{sinc}\left(\frac{\omega}{a}\right) * \frac{1}{b}\operatorname{sinc}\left(\frac{\omega}{b}\right) &= \mathcal{F}\{R(at) \cdot R(bt)\} && (7.15)\\ &= \mathcal{F}\{R(at)\} && (7.16)\\ &= \frac{1}{a}\operatorname{sinc}\left(\frac{\omega}{a}\right) && (7.17)\end{aligned}$$

I hope this was a fun little detour which sparked some curiosity and appreciation for the convolution theorem. It would be interesting to explore other transformations to see if they permit a similar phenomenon.

A.2 Discretizing the Short Time Fourier Transform

This section is dedicated to fully discretizing the STFT. This is particularly relevant for the derivations in chapter 3.

A rectangular analysis window function is defined as

$$R(t) = \left\{ \begin{array}{ll} 0, & \text{if} \quad t > |1/2| \\ 1, & \text{if} \quad t \leq |1/2| \end{array} \right\}. \qquad (7.18)$$

With rectangular windows of width T, the STFT for an input waveform of $a(t)$ is defined as

$$STFT(t, f) = \int_{-\infty}^{\infty} a(\tau) R\left(\frac{\tau - t}{T}\right) e^{-i2\pi f \tau} \, d\tau. \qquad (7.19)$$

This definition is the continuous STFT valid where the window is centered around any time t. If the analysis windows are non-overlapping, as previously assumed, then the STFT at the n^{th} window is

$$STFT[n, f) = \int_{-\infty}^{\infty} a(\tau) R\left(\frac{\tau - nT}{T}\right) e^{-i2\pi f \tau} \, d\tau. \qquad (7.20)$$

Where the window has been centred around time $t = nT$, for some integer n, and the square brackets explicitly refer to the argument as a discrete variable. In more mathematical rigor, $STFT(t, f)$ and $STFT[n, f)$ are two different mappings defined on different domains but whose images coincide when $t = nT$, and thus, using the same name (STFT) for both is justified. It is commonly desired to heavily overlap input analysis windows in practice, however, how that process may be carried out in the optical domain is not entirely straightforward (although it has been suggested that the pulsed Talbot spectrogram operates in this way (16)). The n^{th} segment of the input SUT function is defined as

$$a[n, t) = a(t)R\left(\frac{t - nT}{T}\right). \tag{7.21}$$

Then for the spectrogram, the following comes from the standard definition of the Fourier transform, denoted with $\mathcal{F}$,

$$SPGM[n, f) = \left|\mathcal{F}\{a[n, t)\}^2\right|. \tag{7.22}$$

So far, this definition includes a discrete index running over steps of the time resolution, and a continuous frequency domain. Using the uncertainty principle, it is also possible to discretize over steps of the frequency resolution $\delta f = 1/T$, equivalently the smallest possible frequency step. At a frequency $f_k = k\delta f$, for an integer k not yet bounded,

$$STFT[n, k] = \int_{-\infty}^{\infty} a(\tau)R\left(\frac{t - nT}{T}\right) e^{-i2\pi\frac{k}{T}\tau}\, d\tau. \tag{7.23}$$

Which is the STFT discretized in both domains for a continuous input signal $a(t)$. The definitions for partially and fully discrete STFTs will be useful for the two spectrograms in sections 3.1 and 3.2.

A.3 Talbot Self Imaging

For a more involved derivation of the self imaging effect, I will closely follow a paper by W. Duane Montgomery. In 1967 and 1968 he published two very interesting papers on Rayleigh's diffraction integrals as applied to self imaging. His mathematical derivation showed quite surprisingly (to me at least) that gratings and other periodic structures are not the only objects that can have Talbot self images (51) (90).

The interest is in determining the structure of an object in space at $z = 0$ which will modify an incident wave to reconstruct a faithful representation of the object at a distance $z > 0$. Consider a field of the form

$$\varphi(\mathbf{x}, z)e^{i\omega t} \tag{7.24}$$

Where $\mathbf{x}$ is the possibly multidimensional vector perpendicular to z. Assume that the function space has a Fourier dual, so that there exists a Fourier transform $\Phi(\xi, z)$ at least for all of $z > 0$ of the function. The next assumption is that $\varphi(\mathbf{x}, z)exp(i\omega t)$ is a solution of the wave equation. Then for $k = 2\pi/\lambda$,

$$(\nabla^2 + k^2)\varphi = 0 \tag{7.25}$$

The third assumption is that the function, its Fourier transform, and the relevant derivatives are all square normalizable. Then, act the differential operator on the definition of the Fourier transform.

$$(\nabla^2 + k^2)\varphi = (\nabla^2 + k^2)\int_{\mathbb{R}^2} \Phi(\xi, z)e^{i2\pi\mathbf{x}\cdot\xi}d\xi \tag{7.26}$$

Using equation (7.25) and passing the operator into the integral,

$$0 = \int_{\mathbb{R}^2} \nabla^2 \left(\Phi(\xi, z)e^{i2\pi\mathbf{x}\cdot\xi}\right) + k^2\Phi(\xi, z)e^{i2\pi\mathbf{x}\cdot\xi}d\xi \tag{7.27}$$

The Fourier transform of the function has no explicit dependency on the spatial derivatives except z, and the partial derivative of an exponential is easy to calculate after the product rule. Define the useful quantity

$$K^2 = (k^2 - 2\pi\xi^2) = 2\pi(\lambda^{-2} - \xi^2) \tag{7.28}$$

$$0 = \int_{\mathbb{R}^2} \left([2]\Phi(\xi, z)z + K^2\Phi(\xi, z)\right) e^{i2\pi\mathbf{x}\cdot\xi}d\xi \tag{7.29}$$

Through a standard argument it can be shown the quantity in the brackets must be zero. Therefore,

$$[2]\Phi(\xi, z)z = -K^2\Phi(\xi, z) \tag{7.30}$$

If K^2 is positive then equation (9) is simple to solve using the Fourier basis.

$$\Phi(\xi, z) = A(\xi)cos(Kz) + B(\xi)sin(Kz) \tag{7.31}$$

If K^2 is negative then equation (9) is the usual 1 dimensional wave equation with solutions

$$\Phi(\xi, z) = C(\xi)e^{iKz} + D(\xi)e^{-iKz} \tag{7.32}$$

With the definition of K in hand, it is readily seen that for $K^2 < 0$, $K\epsilon\mathbb{I}$ (the imaginary numbers). Thus $exp(-iKz)$ tends to infinity exponentially with z. This is nonphysical, so set $D = 0$. The other term tends to zero exponentially with distance which, recall from the introduction, produces the effect that Rayleigh observed. Now $z = 0$ is the object plane, let it be described by a function $f(\mathbf{x}) = \varphi(\mathbf{x}, 0)$. With foresight, $f(\mathbf{x})$ is the function to image. Taking the Fourier transform at $z = 0$ there is a restriction on possible solutions,

$$F(\xi) = \begin{cases} A(\xi), & |\xi| \leq 1/\lambda \\ C(\xi), & |\xi| > 1/\lambda \end{cases} \tag{7.33}$$

The following is an important step. According to Paul Latimer and Randy F. Crouse (57), the Talbot effect has a valid reinterpretation as a simple wave-optics phenomenon which is demonstrated using simple interference patterns. While this paper came after Montgomery (51), it gives credit to the claim that in the limit $\lambda \to \infty$, this should agree with the standard geometrical optics. So far there are two regions separated by the line $|\xi| = 1/\lambda$, giving two solutions,

$$\varphi(\mathbf{x}, z) = \int_{|\xi|\leq 1/\lambda} [F(\xi)cos(Kz) + B(\xi)sin(Kz)]e^{i2\pi\mathbf{x}\cdot\xi}d\xi + \int_{|\xi|>1/\lambda} F(\xi)e^{iKz}e^{i2\pi\mathbf{x}\cdot\xi}d\xi \tag{7.34}$$

To agree with geometrical optics, demand $\varphi(\mathbf{x}, z) \to exp(iKz)f(\mathbf{x})$. In other terms,

$$F(\xi)cos(Kz) + B(\xi)sin(Kz) \to e^{iKz}F(\xi) \tag{7.35}$$

This leads to to $B(\xi) = iF(\xi)$ within the circular region. Positive values of z results in the solution

$$\varphi(\mathbf{x}, z) = \int_{\mathbb{R}^2} F(\xi)e^{iKz}e^{i2\pi\mathbf{x}\cdot\xi}d\xi \tag{7.36}$$

To find the imaging condition, first use an approximation on K to confirm Rayleigh's theoretical result. This is known to Montgomery as the weak imaging case. Assume that at the image plane, the frequencies are not attenuated. This means the exponential multiplying $F(\xi)$ must still be imaginary. Therefore, $|\xi| \leq 1/\lambda$. Using the binomial approximation again,

$$K(\xi) = \frac{2\pi}{\lambda}\sqrt{1-\xi^2\lambda^2} \approx k(1-\frac{1}{2}\xi^2\lambda^2) \tag{7.37}$$

Recall $f(\mathbf{x})$ was chosen to be the object plane. The field at a plane $z = d$ should be a multiple of the object. $\varphi(\mathbf{x}, d) = \alpha f(\mathbf{x})$ for $\alpha\epsilon\mathbb{C}$. Taking the Fourier transform of both sides results in

$$F(\xi)e^{iKz} = \alpha F(\xi) \qquad \forall|\xi| \ll 1/\lambda \tag{7.38}$$

A complex number can be written as an exponential, and assuming the spectra is nonzero,

$$e^{ik(1-\frac{1}{2}\xi^2\lambda^2)z_I} = e^{i2\pi\alpha'} \tag{7.39}$$

$$k(1-\frac{1}{2}\xi^2\lambda^2)z_I = 2\pi\alpha' + \theta(\xi) \tag{7.40}$$

In this case $\theta(\xi)$ is a multiple of 2π which could be an extra phase depending on the frequency. At the zero frequency $2\pi\alpha' = kz_I - \theta(0)$. Substitute this into the equation to get

$$-\frac{1}{2}kz_I\xi^2\lambda^2 = -\theta(0) + \theta(\xi) \tag{7.41}$$

Knowing that the right hand two terms are integer multiples of 2π and dividing by that amount,

$$\frac{z_I}{2\lambda}\xi^2\lambda^2 = p(\xi) \qquad \text{where} \qquad p\epsilon\mathbb{Z} \tag{7.42}$$

Granted equation 7.42 doesn't immediately look like the result Rayleigh obtained, but that's mainly because the same notation has not been maintained. Consider a periodic grating like Rayleigh did, with period $1/\xi = d$. Now also consider a monochromatic wave as Rayleigh did with wavelength λ. Finally, rename the imaging distance z_I to the Talbot distance z_T in the case of $p = 1$. Substituting these into the equation will arrive at

$$\frac{z_I}{2}\frac{1}{d^2}\lambda = p(\xi) \Rightarrow \boxed{z_T = \frac{2d^2}{\lambda}} \tag{7.43}$$

It is important to remember the approximations made, but also that ξ could have been a multidimensional vector. In this treatment, an infinite aperture is required with a near point source positioned at a long distance away. It is also assumed the grating frequency ξ was much smaller than the frequency of light. These are all the same conditions both Talbot and Rayleigh used for the grating and aperture when observing this effect, so it's expected that Montgomery arrived at the same result.